1-1-2012

Cryogenic Abrasive Jet Machining of Polydimethylsiloxane and Polytetrafluoroethylene at Different Temperatures

Aaron Glenn Gradeen
Ryerson University

CRYOGENIC ABRASIVE JET MACHINING OF POLYDIMETHYLSILOXANE AND POLYTETRAFLUOROETHYLENE AT DIFFERENT TEMPERATURES

by

Aaron Glenn Gradeen, B.Sc, Queen's University, Kingston ON Canada 2007

A thesis presented to Ryerson University

in partial fulfillment of the requirements for the degree of

Master of Applied Science

in the program of

Mechanical Engineering

Toronto, Ontario, Canada, 2012

AUTHOR'S DECLARATION

I hereby declare that I am the sole author of this thesis or dissertation. This is a true copy of the dissertation, including any required final revisions, as accepted by my examiners.

I authorize Ryerson University to lend this thesis or dissertation to other institutions or individuals for the purpose of scholarly research.

I further authorize Ryerson University to reproduce this thesis or dissertation by photocopying or by other means, in total or in part, at the request of other institutions or individuals for the purpose of scholarly research.

I understand that my dissertation may be made electronically available to the public.

ABSTRACT

Cryogenic Abrasive Jet Machining of Polydimethylsiloxane and Polytetrafluoroethylene at Different Temperatures

Master of Applied Science, Mechanical Engineering, 2012, Aaron Glenn Gradeen

Yeates School of Graduate Studies, Ryerson University

The temperature dependence of the solid particle erosion of polydimethylsiloxane (PDMS), polytetrafluoroethylene (PTFE) and high carbon steel using aluminum oxide particles was investigated. The most efficient machining of PDMS occurred at approximately -178°C, at angles of attack between 30° and 60°. Although it was demonstrated that PDMS could be machined at temperatures above its glass transition, the erosion rate increased by a factor of more than 10 when the machining temperature was below this point.

The maximum erosion in PTFE occurred at the coldest temperature of -177°C between the angles of 30 and 90°. This scenario improved the erosion rate by more than a factor of five. The erosion rate in high carbon steel was increased approximately twofold when lowering the temperature from 17°C to -177°C.

The surface evolution results presented can be used to predict feature shapes both polymers while minimizing cooling costs, minimizing mask wear or maximizing substrate erosion.

ACKNOWLEDGEMENTS

Table of Contents

List of Tables

List of Figures

List of Appendices

Nomenclature

The definition of symbols in alphabetical order:

Symbol	Name	Unit
C	Erosion constant	Non-dimensional
D	Diameter of particle	μm
E	Erosion rate	mm^3/kg, kg/kg
$E(\alpha)$	Erosion rate at an arbitrary angle	mm^3/kg
E_{90}	Erosion rate at 90° angle of attack	mm^3/kg
$G(\alpha)$	Normalized erosion rate	Non-dimensional
$G_P(\alpha)$	Normalized erosion rate for PDMS or PTFE	Non-dimensional
$G_g(\alpha)$	Normalized erosion rate for PDMS or PTFE	Non-dimensional
H_p	Hardness of particle	GPa
H_t	Hardness of target	GPa
h	Nozzle standoff distance	mm
h_c	Convective heat transfer coefficient	W/m^2K
k	Velocity exponent	Non-dimensional
k_2	Empirical constant	Non-dimensional
K_{90}	Empirical constant	Non-dimensional
$\dot{M}$	Mass flow of erodent	kg/s
$\dot{m}_\alpha$	Mass flow of erodent during machining of a channel at a nozzle angle attack of α	kg/s
$\dot{m}_{90}$	Mass flow of erodent during machining of a channel at a nozzle angle attack of 90°	kg/s
M(x)	Scaling function for mass flux accounting for mask edge effects	Non-dimensional
n	Empirical constant	
n_1, n_2	Parametric exponent	Non-dimensional
Nu	Nusselt number	Non-dimensional
r	Radial position within the abrasive jet	μm
V(x)	Velocity distribution of erodent particles within the abrasive jet	m/s

z_t	Partial derivative of profile depth with respect to time, t.	μm/s
z_x, z_y	Partial derivative of profile depth with respect to location within the channel, x and y.	Non-dimensional

Greek Symbols

α	Angle between the nozzle and the target material	°
β	Nozzle focus coefficient	Non-dimensional
$\varphi(r)$	Particle mass flux distribution	kg/s
θ	Local impact angle between the incoming erodent particle and the target surface	rads
ρ	Density of the target	kg/m^3

1 Introduction

1.1 Motivation

Abrasive jet micromachining (AJM) is a relatively new micro-fabrication technology in which a jet of pressurized air is used to accelerate small particles towards a target surface which is thus machined by solid particle erosion mechanisms. Figure 1-1 shows a basic AJM machining setup.
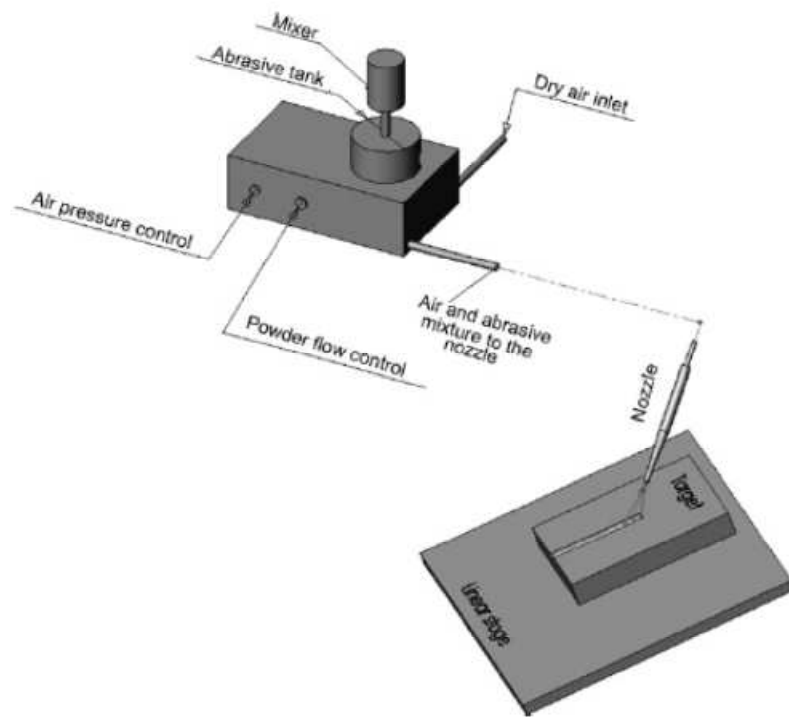
Figure 1-1 Experimental apparatus for basic AJM [1].

Erosion resistant masks patterned with small openings are typically used to define the features to be machined. Below is an example of two metal masks placed parallel to one another in order to produce a channel.
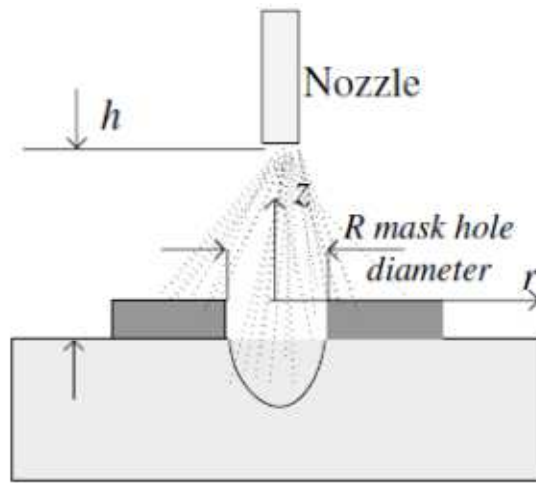
Figure 1-2 Channel cross sectional view showing the placing of metal shims (dark grey) used as a mask.

AJM is a relatively low cost process that can have high etch rates which can be directionally controlled. For example, wet etching in glass typically occurs at a rate of 4-8 µm/min uniformly in all directions [2] whereas AJM can achieve directional etch rates of 100 µm/s in glass. AJM can be used to machine glass, ceramics, ferrous materials and a variety of polymers. Plastics such as polydimethylsiloxane (PDMS) and polymethylmethacrylate (PMMA) are widely used in, e.g., microfluidics since the fabrication of polymeric chips does not require expensive equipment (i.e. soft lithography and hot embossing) [3, 4]. The elastomer Polydimethylsiloxane is of particular interest in microfluidics because it is chemically resistant, biocompatible, and relatively easy to mold and seal [5]. Polymeric materials such as PDMS and PMMA have problems of adsorption, absorption and incompatibility with organic solvents. PDMS, for instance, is known to swell when exposed to most alcohols. Using PTFE (polytetrafluoroethylene) as substrate material solves these problems since it is highly inert, non-adhesive and is resistant to solvents [6]. Also, PTFE is known to be more stable over a wide range of temperatures than other polymers due to its high melting point of 340°C [7]. PTFE is also known to retain ductility in tensile tests even at low temperatures (-196°C)[8]. For these reasons, PTFE shows great potential in the microfluidic sector.

Previous research found that it was impossible to machine cured PDMS using AJM at room temperature with 25 µm aluminum oxide particles impacting at approximately 140 m/s due

to its ability to absorb the energy of the impacting particles [3]. Getu et al. [3] were able to machine PDMS with 25 μm aluminum oxide particles at an impact velocity of approximately 140 m/s [9] using a cryogenic abrasive jet micromachining (CAJM) apparatus that cooled the surface region to approximately -150°C. Due to lack of cryogenic flow control, this experimental setup was only capable of blasting at the lowest temperature attainable while the surface was being flooded with liquid nitrogen. It was therefore unknown as to how erosion behaved at the intermediate temperatures.

In summary, both PDMS and PTFE have shown an increase in solid particle erosion, and thus the machining material removal rate, when the machining temperature is dropped significantly [3]. It is not, however, known how the material removal rate and the erosion mechanisms change at intermediate temperatures, because the previous CAJM apparatus was capable of only flooding the surface with liquid nitrogen, giving a single machining temperature. A change in erosion mechanism usually manifests itself as a change in the dependence of the erosion rate on the nozzle inclination angle, which, in turn, strongly affects the shape of the machined feature [4]. As a result, the size and shape of micro-channels machined using CAJM at these intermediate temperatures is also unknown. The thesis objectives in Section 1.2 outline the steps that were taken to address this gap in the literature.

1.2 Thesis Objective

The overall objective of the thesis is to investigate how erosion in PDMS and PTFE are affected by temperature and nozzle angle of attack in the range of 17 to -196°C. In order to reach this primary objective, the following secondary objectives will be met:

(i) Design and implement a cryogenic abrasive jet machining apparatus which is capable of blasting consistently and predictably at temperatures between 17 and -196°C.
(ii) Investigate the erosion magnitude and angle dependency in PDMS, PTFE and high carbon steel (used as a mask material) at these temperatures.
(iii) Use the angle dependency results in existing surface evolution models in order to predict the size and shape in unmasked and masked channel profiles in PDMS and masked channels PTFE.
(iv) Isolate the erosion per unit kinetic energy of the erodent by extracting the particle velocity from the depth of a glass channel. Use this information to suggest optimal machining conditions.

2 Literature Review

2.1 Solid Particle Erosion

Solid particle erosion is a process in which material is removed through the repeated impact of small solid particles. This can be undesirable in processes involving turbines, pipelines, valve systems carrying particulate matter or any other industrial system exposed to a particle laden environment. Solid particle erosion can also be used to process materials, such as in surface hardening, burr removal, blast cleaning, and machining. An important example of a machining process which can be used for rapid prototyping of microelectromechanical systems (MEMS) and microfluidic chips is abrasive jet micro-machining (AJM).

2.1.1 Classifying Erosion

Erosion is typically quantified by mass of material removed per mass of erodent used, i.e., the erosion rate. It is also typically categorized as being either ductile or brittle [10]. Feng et al. state that brittle erosion due to angular particle impact is most commonly classified as being associated with lateral cracking due to residual stresses from impact[10]. For brittle materials, erosion is very sensitive to the hardness and fragility of erodents. Feng et al. state that higher residual crack driving forces are created when the ratio of erodent to target hardness is increased.

Material removal is considered to be dominated by a brittle mechanism when the erosion rate is maximized while the incident particle velocity is perpendicular to the surface. Alternatively, ductile erosion is considered to dominate when the erosion rate is maximized at a certain oblique angle, which depends on the material. Erosion rates at oblique angles in some ductile materials can be up to 16 times larger than erosion at perpendicular incidence [11].

Oka [11] explains brittle erosion as being caused by repeated deformation of the surface whereas ductile erosion is said to be dominated by particles cutting the surface. Brittle erosion is thought to mainly occur due to the vertical impact energy of the particles and ductile erosion mechanisms are thought to be caused by the horizontal impact energy of the particles responsible for cutting.

2.1.2 Erosion Mechanisms in Polymers

Walley and Field [12] investigated the solid particle erosion of polyethylene, which is a polymer considered to behave in a ductile manner since maximum erosion occurs when the nozzle is inclined between 20 and 30° from the surface. Steel spheres with diameters between 2

and 8 mm were used to model single impacts of smaller sand particles (300- 600 μm) since high speed photography had trouble capturing the small particles. The authors found that lips were produced at the crater edge beyond a certain velocity and within a specific range of impact angles. These lips produced by single particle impacts were typically weakly bonded to the surface in metals but in polyethylene, these lips were strongly bonded. The drawing out of filaments by rounded particles and the cutting off of chips by sharp particles were the two erosion mechanisms found.

Arnold and Hutchings [13] briefly mentioned that the erosion mechanism in natural and styrene-butadiene rubber is fatigue crack propagation. High tensile stresses in the surface are said to cause the fine cracks to grow which in turn results in material removal. These rubbers behaved in a ductile manner since erosion was maximized at about a 15° angle of attack. Scanning electron micrographic analysis of the rubber surface eroded at a 30° angle of attack with silica particles travelling at approximately 100 m/s resulted in a series of ridges running transversely to the impact direction. Arnold and Hutchings [14] published a second paper which successfully modeled erosion in rubber at normal incidence based on a material removal mechanism of fatigue crack growth. Frictional traction of the particles during impact was said to be responsible for crack growth.

Hutchings and Deuchar [15] investigated the solid particle erosion of unfilled elastomers. The high resilience rubbers displayed transverse ridges with large globular fragments of rubber attached and more rounded features on the surface. Besztercey et al. [16] found these same ridges on the surface of silicon rubber after solid particle erosion at oblique angles. The erosion mechanism of cyclic crack growth was proposed. The low resilience rubbers Hutchings and Deuchar studied showed no directionality on the surface; only evidence of loosely attached rubber fragments and numerous cracks and fissures were found. A catastrophic tearing process which removed small fragments of rubber was suggested as the erosion mechanism. Harsha and Thakre [17] also found micro-cracking to be the dominant failure mechanism in neat polyetherimide even though it is considered to be a ductile polymer. Erosion by plastic deformation at 60° was identified due to large fibrils that were cut from the substrate but still adhered to the surface. Zahavi and Schmitt [18] also saw a lack of directionality in the erosion of an elastomeric polyurethane coating at 15 and 30°. Elongated craters approximately 20% of the particle size along with cracks and fragments of material were seen.

Barkoula and Karger [19] mentioned the basic material removal mechanisms of tearing and fatigue for rubbers, cutting and chip formation for ductile polymers and crack formation/brittle fracture for brittle polymers. For elastomers specifically, they gave two main mechanisms of erosion. The first was tensile stresses due to frictional forces causing fine cracks to grow in the surface which eventually resulted in material removal. The second was an increase of steady strain because of incomplete strain relaxation between particle impacts. An interesting point was also made that amorphous polymers tended to show more brittle features when examined under microscope.

2.1.3 Erodent and Target Properties Affecting Erosion

Oka et al. [11] attempted to construct a direct correlation between material hardness and erosion. Single particle impacts on surfaces of various metal and polymers were investigated with respect to the volume of the impact site. The authors stated that the tested material hardness could not be used for the case of multiple impacts since strain hardening occurs in the material as well as softening due to the temperature rise caused by the particle impacts. To investigate this potential temperature rise, a thermocouple was mounted on the backside of an iron leaf which was impacted with a particle. A rise of 30 K occurred at the thermocouple. Analysis using a finite element program indicated that the temperature at the surface would have to be 973 K to produce such a temperature on the backside of the iron leaf. It appears this temperature rise would be highly dependent on the material since temperatures of that magnitude in polymers would cause melting. Oka's erosion rule is defined as:

$$E = K_{90}(H_P)^{-n} \tag{2-1}$$

where E is erosion measured as mass of materials removed per mass of erodent used, H_p is the hardness of the substrate material and K_{90} and n are empirically determined. This equation assumes that the amount of volume removed by a single particle impact is analogous to the volume of indentation in a hardness test.

Although Oka found a good correlation between material hardness and erosion for apparently ductile materials such as PMMA, Feng [10] believes this relationship to be irrelevant during ductile erosion but that hardness still plays a role in brittle erosion. Feng's results for

erosion on glass using diamond, silicon carbide, alumina and silica erodent particles gave the following relationship

$$E_p \propto \rho^{0.96} V^{2.37} D^4 (H_p : H_t)^{0.465} \tag{2-2}$$

where ρ is the density of erodent, V is the velocity of the erodent particles, D is the diameter of the erodent particles, H_p is the hardness of the particles and H_t is the hardness of the target. For ductile materials, Feng's study concluded that the shape of the particles also affects erosion. This dependence upon particle shape is not surprising since the main erosion mechanism in ductile materials is cutting, and one would expect that sharper, more angular particles would produce higher erosion rates.

2.1.4 Erodent Velocity

The velocity of the erodent particles is connected to the erosion rate through an empirical power law relation expressed as [10];

$$E \propto V^k \tag{2-3}$$

where E represents the volume or mass of material eroded per mass of erodent, V is the velocity of the impacting particles and k is the experimentally determined velocity exponent. This is one of the basic fundamental laws of erosion. The most basic of models would assume that the erosion rate is proportional to the kinetic energy of the particle so k would have a value of two. In reality, k values vary typically between 1 and 4.

2.1.5 Angle Dependence of Erosion

The angle at which maximum erosion occurs has important implications for the efficient machining of materials using an abrasive jet. Oka et al. [20] studied the angle dependence of erosion for various types of metals, a ceramic and a plastic material. The authors suggested a semi-theoretical model that differentiated between the two mechanisms of erosion mentioned in

Section 2.1.1. The semi-theoretical equation was expressed in terms of material hardness and impact angle as

$$E = K_{90}(Hv)^{-n}(sin \propto)^{n_1} \left[\frac{k_2 - sin \propto}{k_2 - 1} \right]^{n_2}$$

(2-4)

where α is the angle between the erodent trajectory and the substrate surface, K_{90} and n are constants at normal impact angles, Hv is the hardness of the substrate material, and k_2, n_1 and n_2 are constants determined by material properties. Oka et al. found that a plot of normalized erosion ($E(\alpha)/E(90)$) versus impact angle fit this model very well for all the metallic materials tested. It was found that the peak in erosion occurred at an angle which became smaller as the material hardness decreased. Therefore materials with a very large hardness value would be expected to have a maximum erosion rate closer to 90° whereas materials with low hardness values would have a maximum erosion rate closer to 15°. The shape of this normalized curve was found to be independent of particle velocity within the ranges used (50-130 m/s). Particle velocity was only seen to increase the amount of erosion by shifting the non normalized erosion curve upwards. Oka's model was unable to predict the erosive behavior of the ceramic material with respect to impact angle and material hardness. Oka et al. conclude that if the material hardness and erosion at normal angles is known, this formula can be used to effectively estimate erosion at various impact angles.

2.1.6 Temperature Dependence of Material Properties

The mechanical properties of materials are known to be temperature dependent. A brief review of how the erodent and substrate materials behavior changes with temperature is thus warranted.

PDMS and PTFE are both polymeric materials. Polymers are long chains which are made up of numerous single units called mers. The degree of polymerization is dictated by the length of these polymers which in turn is controlled by energy available (ie. heat input) during polymerization. There are three main categories of molecular structure for polymers. A linear polymer forms a single continuous path from one end to the other with no branches. A branched polymer has a main backbone with smaller branches leading from it. Finally, a cross linked polymer is more like a network analogous to a spider web but without the degree of order. The

polymer structure dictates the mechanical properties of the material. Elastomers such as PDMS, have a high degree of cross linking. PDMS is also considered to be an amorphous polymer due to the degree of random entanglements and highly disordered states of the polymer structure. Amorphous polymers tend to behave in a viscoelastic manner due to the Van der Walls bonds formed between various folds of the polymer chain. This results in high strain rates causing large amounts of stress due to the friction from the molecular motion [21]. PTFE, on the other hand, is considered to be a linear polymer. This is because PTFE cannot be crosslinked due to its chemical inertness [21].

Three main factors govern the ductility and toughness of polymers: strain rate, temperature and molecular structure. Temperatures well below glass transition and high strain rates result in the polymers fracturing as opposed to yielding. Upon fracture, the covalent bonds between carbon atoms must be broken (chain scission) but the aforementioned secondary forces of the Van der Walls bonds also play a major role. Stress concentrations can occur in polymers due to non homogeneous entanglements. This means that some polymer chains can experience large amounts of stress while others experience very little [21].

Boyer [22] performed an extensive review of research pertaining to the mechanical properties of various polymers used for structural purposes. The author used data published from electrical, electromagnetic and dynamic mechanical testing to infer how molecular motion affects the mechanical properties, specifically impact strength, of these polymers. Boyer, however, was quick to point out that using the stated glass transition and melting temperatures of the polymer as a tool for predicting mechanical behavior is not sufficient. The glass transition temperature is defined as the temperature in which a material transitions from ductile to brittle behaviour due to a decrease in molecular mobility. It has been found that other transitions and relaxations lie below and above glass transition (T_G). Boyer attempted to correlate the β relaxation parameter, which is a transition existing below T_G, with the polymers impact strength at room temperature. This was found to be a poor generalization since too many exceptions existed for other polymers. The results summarized by Boyer also indicate that impact strength decreases with temperature. This relationship is unique to each polymer so ultimately correlations cannot be made regarding polymer fracture at various temperatures with this data.

The properties of the erodent particles are also important when characterizing erosion from an abrasive jet. Temperature could affect the erosive behaviour of the particles themselves.

Since the most common type of abrasive used in AJM is aluminum oxide, a brief look into how the mechanical properties behave at various temperatures is useful. Gonzalez et al. [23] investigated the mechanical properties of alumina, specifically Young's Modulus and yield stress, from room temperature up to 1200 °C, where the onset of creep was observed. The results showed a clear decrease in Young's Modulus as temperature was increased. A linear decrease in the hardness of alumina as the temperature was increased was also found. These results could be extrapolated to lower temperatures in order to predict how the mechanical properties of alumina change at cryogenic temperatures.

Khanna et al. [24] investigated the wear characteristics of alumina at cryogenic temperatures. This study was motivated due to the need for appropriate material selection in cryo-turbopumps in the space shuttle main engine. Structural ceramics, such as alumina, have a low density and high hardness compared to the materials normally used (martensitic stainless steel). This makes alumina an ideal candidate to increase bearing life. Ceramics are said to be brittle due to the limited number of slip systems for plastic flow. The authors suggested that the cryogenic temperatures cause surface hardening which triggers the onset of brittle fracture. This type of fracture is confirmed by the presence of transgranular and intergranular fractures. Khanna et al. conclude that cryogenic temperatures enhance the brittle fracture of alumina. This conclusion suggests that fracture of the alumina particles upon impact of the cold susbtrate surface could decrease the erosion rate since energy is expended during particle break up.

2.2 Abrasive Jet Micromachining of Features

Features can be machined using AJM by selectively etching the surface using patterned masks which are highly resistant to solid particle erosion. Mathematical models have been constructed in order to predict the growth and profile shapes of features such as micro-holes, channels and planar areas.

ten Thije Boonkkamp and Jansen [25] took a mathematically rigorous approach to surface evolution modeling which included finding an analytical solution to a partial differential equation. They proposed a model which predicted the position of the machined surface based on a brittle erosion process (i.e. only the normal component of the particle velocity contributes to erosion). The erosion rate (ratio of mass of target material removed to the mass of abrasive used to remove it) was related to the velocity as follows

$$E = C(|v|\cos\vartheta)^k \tag{2-5}$$

where θ is the angle between the velocity vector and the surface normal vector, v is the velocity of the particles, C is the erosion constant and k is the velocity exponent.

A partial differential equation for the surface position was obtained which was based upon the speed in which the surface progresses, c, along with the partial derivatives of depth, z, with respect to time, z_t, and location z_x and z_y:

$$z_t - c\sqrt{1 + z_x^2 + z_y^2} = 0 \tag{2-6}$$

Slikkerveer's model was then used to calculate the speed of the surface as

$$c = \frac{1}{\rho_s} E\varphi\cos\theta \tag{2-7}$$

where E is the erosion rate, ρ_s is the substrate density, φ is the particle mass flux in the direction of velocity and θ is the angle between the velocity and the normal to the surface. Substituting the equation for erosion rate, E, and the speed of the surface, c, into Eq. 2-6 results in:

$$z_t - \frac{C}{\rho_s} v^k \varphi (1 + z_x^2 + z_y^2)^{-k/2} = 0 \tag{2-8}$$

Characteristic strip equations are then obtained to transform this partial differential equation into a set of ordinary differential equations with initial conditions. An analytic solution is obtained using a k value of 2. The resulting profiles obtained have much sharper features than the experimental results. Also, the flat bottom predicted by their solution was not seen in the experiment. ten Thije Boonkkamp and Jansen ignored second strike effects so the model was unable to predict the udder shape at increasingly larger depths. Boonkamp suggested that further study is required to predict how second strike effects alter the feature profile.

2.2.1 Abrasive Jet Micromachining of Ductile Materials

Most of the aforementioned studies focused on eroding brittle materials (mostly borosilicate glass) at normal angles of attack. Getu et al. [4] and Ghobeity et al. [26] developed surface evolution models that allow the prediction of the size and shape of features such as micro-channels and micro-holes machined using AJM in ductile erosive polymers such as PMMA [4, 26]. Getu et al. [4] found that the ductile erosion mechanism in polymers affected the angle dependency of erosion, leading to feature shapes which were markedly different from those in brittle materials such as glass. They found that micro-channels machined in PMMA developed steep sidewalls and broad, flat bottoms, rather than the more V-shaped channels typical of AJM in glass. A surface evolution model for ductile materials was used to predict the profile of holes in PMMA.

The equation describing the depth, z, of feature shapes machined in ductile materials using AJM, as a function of time, t, was expressed as [4]:

$$z_{t^*}^* = \left(E^*(x^*) \sqrt{(1 + z_{x^*}^{*2})} \right) G(\theta) \tag{2-9}$$

where Eq.(2-9) has been nondimensionalized by normalizing the length variables to the nozzle standoff distance; i.e. $z^*=z/h$, $x^*=x/h$, The nondimensional time $t^*=t/T$ has been normalized to the amount of time, T, required to propagate the surface to a depth equal to the nozzle standoff distance. $z^*_{t^*}$ and $z^*_{x^*}$ are the partial derivatives of the nondimensional depth of the surface with respect to t^* and x^*, respectively.

For ductile erosion, which is thought to be the main mechanism of erosion in polymers [19], an angle dependency, $G(\theta)$, must be added to the surface evolution equation. The local angle of attack, θ, depends on the local slope of the surface, z_x, as

$$\theta = \left[\frac{\pi}{2} - arccos \left(\frac{1}{\sqrt{1+z*_{x*}^2}} \right) \right] \tag{2-10}$$

$G(\theta)$ expresses the dependence of the erosion rate on the local impact angle θ, between the component of the velocity vector in the plane of the channel cross section and the local surface

tangent (See Fig. 4-2). It can be interpreted as the ratio of the erosion rate at the impact angle θ divided by the erosion rate at 90°.

Ghobeity et al.[26] experienced a problem in predicting the surface evolution of deeper holes due to an increase in particle embedding at around an aspect ratio of 0.6. It was thought that this particle embedding slowed the erosion process.

Getu et al. [1] also investigated the surface evolution of holes and channels machined in polymers, specifically PMMA, at oblique angles of attack. Since the already known velocity distribution and mass flux for this particular setup at 90° cannot be inferred at other angles, a first pass fit was used to determine the erosive efficacy of the jet for masked holes and channels. The authors saw a significant difference in channel depth between the cases of forward scanning and backward scanning. The scan direction was considered to be backwards when the horizontal component of the particle velocity was moving in the same direction as the substrate. This difference was attributed to particle embedding. Intermediate angles, specifically 55°, showed the most noticeable difference in erosion with regards to scan direction. The forward scan speed required more particles to erode the surface to a certain depth than the backwards scanning process. This difference was attributed to the energy flux distribution difference between the leading and trailing edges of the jet, which was said to affect particle embedding. Shipway et al. [27] have suggested that the level of particle embedding is a function of the particle impulse which is related to the normal component of velocity with respect to the surface. Getu et al. also confirmed that particle embedding decreased erosion rate in PMMA by machining a hole with particles initially embedded into the surface. The depth of this hole was shallower in comparison to a hole with initially no particle embedding.

2.2.2 Second Strike Effects

Slikkerveer et al. [59] attempted to account for second strike effects in order to model the udder shape evident at a certain depth to width ratio for stationary holes in AJM. It was assumed that the particles rebounded with 20 to 50% of their original impact velocity. The rebound angle was also kept as a variable between 0.8 and 1.2 for the purposes of fitting the experimental results. Slikkerveer modeled second strike effects by introducing another term into the partial differential equation that resulted in the prediction of an udder-like shape in the centre of the feature which agreed with experimental observations. The PDE (Eq. 2-8) was then solved using

a numerical method (adapted Roe's algorithm). Slikkerveer noted that the profiles became increasingly difficult to predict as the features became deeper. This difficulty was suggested to arise from particle spatial hindering as the feature became narrow at larger depths. It was claimed that larger particles are not capable of eroding the deepest portion of the feature. The mask was also thought to impede the particles from eroding the surface close to the boundaries. Slikkerveer concluded by saying that the model could be improved by further investigating the angle dependence of erosion for glass.

2.2.3 Particle Mass Flux and Velocity Distribution

Ghobeity et al. [46] modified ten Thije Boonkkamp and Jansen's a surface evolution model to include the particle flux and velocity distributions in the abrasive jet. The authors experimentally verified their model along with a new method of determining the effects of the mask on the erosive power distribution. Thick masks were used and were found to improve channel edge definition. A phase Doppler particle analyzer (PDPA) was used to determine the particle velocity distribution within the jet.

A novel method of obtaining the erosive efficacy was also introduced by Ghobeity et al. in another study. By obtaining the surface profile of a shallow hole, the angle dependence of erosion could be ignored in Eq. 2-9 (Section 2.2.3) and the erosive power distribution of the jet could be inferred from a fitted polynomial of the surface,

$$E^*(x^*) = V^*(x*)^k \varphi^*(x*) \tag{2-11}$$

where $V^*(x^*)$ and $\varphi^*(x^*)$ are the particle velocities and mass flux distributions within the jet respectively, normalized by their values at the centre of the jet.

The particle velocity distribution from the centre to the periphery of the jet was found to be linear. A Weibull distribution was the most appropriate fit to particle mass flux, $\varphi(r)$.

$$\varphi(r) = \frac{\dot{M}}{\pi}\left(\frac{\beta_w}{h}\right)^2 e^{-(\beta_w r/h)^2} \tag{2-12}$$

Eq. 2-12 shows that mass flux depends only on the radial location in the jet, *r*, and not the angular position in the plane of the nozzle exit. $\dot{M}$ represents the total mass flow rate of the jet, β_w is the experimentally determined nozzle focus coefficient and *h* is the standoff distance. This flow focus coefficient is found to be unique for each nozzle and particle system.

Ghobeity et al. [46] had some unique results with a *k* value of 1.43. This value differs from most quoted *k* values which lie between 2 and 4. This new *k* value was confirmed to be correct for the blasting setup since it improved model predictions. These results were used to obtain results for masked channels which accounted for mask interference effects (Section 2.2.5). This "first pass" method greatly improved feature depth predictions from 32% errors down to only 8% errors up to feature aspect ratios of 1.

2.2.4 Jet Divergence

Since the particle velocity distribution and mass flux are pertinent to the shape of the eroded features, the characteristics of nozzles which affect these two parameters are briefly reviewed.

Stevenson and Hutchings [7] investigated how the jet divergence was affected by the particle velocity and the nozzle length. A novel method was used which measured the rate at which a thin blue film was removed from a surface. This information was then used to determine the nozzle focus coefficient, *β*. A nozzle with a larger *β* is more focused than one with a smaller *β*. The authors found that the particle exit velocity was only slightly affected by the nozzle length assuming the same pressure drop across the nozzles inlet and outlet. Also, length to internal nozzle diameter ratios of over 30 were found to have a constant divergence angle. The authors attributed this to the aerodynamic entry length of each nozzle. If the nozzle length was well above the flow entry length then the flow focus coefficient would remain unchanged. The flow focus coefficient was found to depend on particle velocity, but remained relatively constant above a certain velocity threshold.

Shipway and Hutchings [28] found motivation for their study based on the fact that erosion rates have appeared different under seemingly similar gas blast erosion tests. The authors found that the gas plume was unaffected by the nozzle internal roughness whereas the particle plumes were. Shipway and Hutchings found that the flow focus coefficient was smaller for rough nozzles than for smooth nozzles, implying that smooth nozzles produce a more focused

jet. This is a logical result since the divergence of the particles is caused by interactions with the nozzle wall. A rougher nozzle will result in larger rebound angles as the particles exit the nozzle. For this reason, it is important to frequently replace nozzles since the flow of particles against the nozzle wall will alter surface roughness over time. Shipway and Hutchings conclude that the nozzle internal roughness plays a major part in the erosive efficacy of a jet. They suggest quoting the flow focus coefficient while performing gas blast erosion tests so that the tests can be directly compared.

2.2.5 Mask Edge Effects

Materials which have a high resistance to solid particle erosion are used to protect the substrate surface and hence provide selective erosion. High carbon steels can be patterned or strategically placed on the substrate surface in order to machine small holes or channels. The presence of the mask is known to effect the erosive efficacy, $E^*(x^*)$, near the mask edges. The erosive efficacy describes the potential of an abrasive jet to remove material based on the distribution of particle velocity and mass flux.

ten Thije Boonkamp and Jansen assumed the mask had an effect of linearly decreasing the erosive efficacy near the channel edges. This resulted in a sharp transition point between the mask affected area and the non mask affected area that, however, was not seen in experiments. To better predict mask effects, Ghobeity et al. used a shallow first pass method to determine the effect of the mask on the erosive efficacy for the channel. In another paper, Ghobeity et al. [29] presented an analytical solution for modeling how the erosion profile was affected by mask width and particle size distribution. In their model, if any portion of the particle hit the mask, it was assumed to not contribute to erosion. The probability of a particle of a specific size travelling through a certain position within the mask opening was transformed into the mass probability by using the known density of the particle material. The result was nondimensionalized with respect to the incoming mass flux at the centre of the jet, and incorporated into the erosive efficacy expression for shallow features:

$$E^*(x^*) = M^*(x^*)\varphi^*(x^*)v^*(x^*)^k \qquad (2\text{-}13)$$

where the velocity and particle flux to the mask opening have been normalized to their values at the centre of the jet, at $x=0$, i.e. $V^*=V(x)/V(0)$ and $\varphi^*= \varphi(x)/ \varphi(0)$. Oscillating the abrasive jet in a direction perpendicular to the scanning direction resulted in a non-dimensional velocity flux and particle mass flux of one incident to the mask opening. This simplified the erosion equation making the erosive efficacy through the mask opening, $E^*(x^*)$, directly equal to $M^*(x^*)$, an expression for the mass flux accounting for mask edge effects. The analytical model was compared to experimental results by substitution into the surface evolution model (Eq. (2-9)). It was found to be in good agreement with the obtained profiles. A parametric study was also performed which indicated that particle size distribution could have a major effect on the channel profile and maximum depth. Using smaller particles could increase the sidewall slope and result in deeper channels compared to using larger particles.

2.2.6 Cryogenic Erosion of Polymers and Steels

Getu et al. [3] investigated the erosion of PTFE, ABS and PDMS at room temperature and cryogenic temperatures. The liquid nitrogen entraining into the abrasive jet at a 10 degree angle was said to produce a surface temperature of about -150 °C.
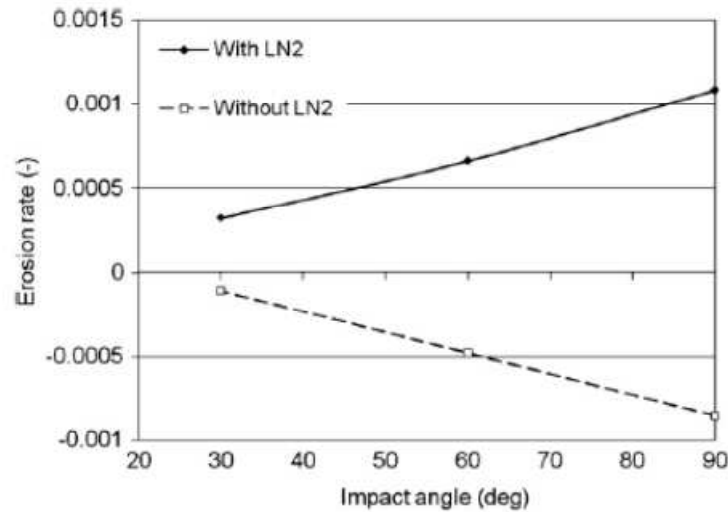
Figure 2-1 Erosion improvement of PDMS at low temperatures [3]

Figure 2-1 shows how cooling by liquid nitrogen (LN2) can increase the erosion rate, which only exhibits particle embedding at room temperature. The figure also reveals that PDMS

17

exhibits maximum erosion at normal angles of impact suggesting that LN2 causes a ductile material to behave in a brittle manner. In all three polymers, the erosion rate at normal incidence was increased but with PTFE the maximum erosion rate still occurred around 60 ° suggesting a mix between ductile and brittle erosion still existed. Getu et al. also noted a decrease in the amount of particle embedding and smoother surfaces under cryogenic blasting conditions. Cryogenically assisted abrasive jet machining resulted in erosion at normal angles of incidence in all three polymers, when at room temperature this was impossible.

Getu et al. also published another paper [30] which investigated the temperature distribution beneath the abrasive jet for a stationary and moving substrate of PDMS using their CAJM setup. The authors found that the thermal front moved approximately 12 times faster than the material removal front. Temperature profiles beneath the scanning jet for various scans speeds were produced using a finite element analysis. The model results and temperature readings of embedded thermocouples again suggested that PDMS could be machined at temperatures above the glass transition.

Urbanovich et al. [31] used nitrogen gas flowing within a coiled heat exchanger to investigate the low-temperature erosion of ball bearing steel at various angles of attack, and polyamide at 90° with quartz sand (0.2-0.315 mm diameter). The erosion rate of polyamide increased by a factor of about six when cooled to -120°C. In another study, Urbanovich and Kramchenkov [32] observed an erosion increase in steel (ShKh15) by a factor of 1.7 when the blasting temperature was dropped from 293 K to 120 K.

2.2.7 Temperature Dependence of Erosion in Glass

Muju and Pathak [33] cooled a glass slide to liquid nitrogen temperatures to investigate the possibility of increasing the erosion rate of glass while cooling during particle erosion. It was found that the erosion rate was increased consistently by approximately 10-12%. The results are shown in Figure 2-2 which compares hole depth for various standoff distances at room temperature and liquid nitrogen temperatures.
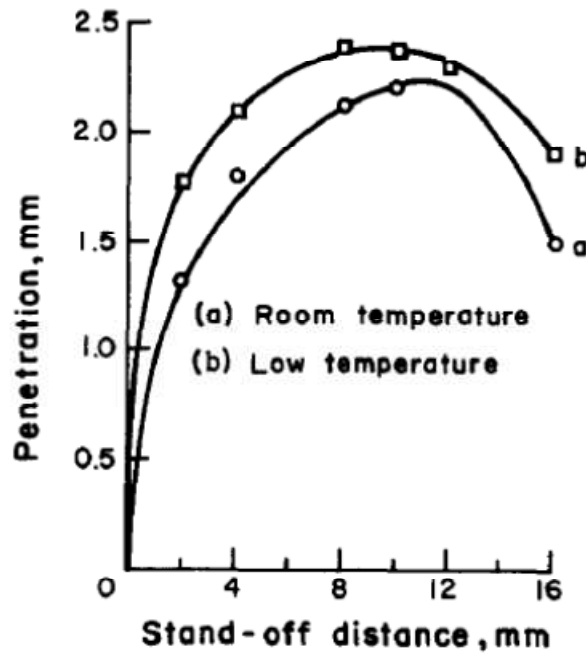
Figure 2-2 Brittle erosion enhancement in glass at low temperature [33]

It should be noted that since the jets impinged upon opposite sides of the glass, the surface temperature of the glass at the site of impact was not at -196 °C. The authors suggest that the low temperatures increased the yield strength which in turn decreased the fracture toughness of the material thereby allowing larger lateral cracks to form upon particle impact. The authors also presented a surface pressure model which attempted to explain the increase in material removal. Due to the suspected increase in the modulus of elasticity and the supposed decrease in Poisson's ratio, it was suggested that the surface pressure due to impact increased by about 9% at low temperatures. Another experiment was performed where the glass was exposed to the abrasive jet for short periods. It was found that the features were wider for the cryogenic case which led the authors to conclude that lateral cracks were therefore larger. Since the authors used such small particles (30 µm) it is not expected that the size of the lateral cracks would affect the jet footprint. This is likely dictated instead by the nozzle flow focus coefficient, nozzle roughness and standoff distance. If in fact colder temperatures result in larger lateral cracks, single particle impacts under cryogenic conditions should instead be investigated.

2.3 Basic Heat Transfer

Knowledge of the heat transfer mechanisms cooling the abrasive jet and the substrate material will be useful when investigating how the polymer surface temperature evolves during CAJM, and in the design of the CAJM apparatus (Section 3.1). To gain an understanding of these mechanisms, some heat transfer theory is briefly reviewed.

2.3.1 Boiling Regimes of Heat Transfer

The phase of the impinging fluid exiting the nozzle will affect the magnitude and mechanisms of convective heat transfer at the target surface. If the impinging jet is a liquid there is an opportunity for phase change into a gas, referred to as the boiling regime. When air is used as the carrier gas, oxygen is the first element to liquefy at approximately -182°C. For example, if the heat exchanger of Section 3.1.4 cools the air enough to sufficiently liquefy it, large convective heat transfer coefficients can be obtained. Various boiling regimes exist which depend on the difference between the surface temperature and the liquid saturation temperature (T_e=$T_{surface}$-$T_{saturation}$). Stated in an order of increasing T_e, the boiling regimes are; free convection, nucleate, transition and film boiling [34]. A maximum heat flux exists in the upper end of the nucleate boiling regime and is referred to as the critical heat flux (CHF). Nucleate boiling can be identified by little bubbles forming at the heat transfer surface.

2.3.2 Pool Boiling Heat Transfer

Pool boiling is a method of heat transfer which could be used to cool the substrate or the abrasive air mixture as it travels through the tubing (Section 3.1.4). Vader et al. [35] combined submersion pool boiling with jet impingement cooling in order to cool a central processing unit. Heat flux values of up to 80 W/cm^2 (800000 W/m^2) were reported with a submerged sub-cooled impinging liquid nitrogen jet. Assuming a temperature difference between the substrate and the jet of 220°C, a convective heat transfer coefficient of about 3600 W/m^{2}K is obtained. Submersing the substrate provides a modest improvement in heat flux but also requires an enclosure to contain the liquid which would be an added complication to the cooling system. Pool boiling alone results in modest heat flux values compared to liquid jet impingement. Vader states that typical values of pool boiling heat flux in liquid nitrogen are between 15 and 30 W/cm^2 although critical heat flux values have been reported to be around 19 W/cm^2. Drach et al.

[36] use the Kutateladze critical heat flux correlation to obtain similar critical heat flux values for pool boiling in liquid nitrogen. Using this correlation along with the parameters for liquid nitrogen, a critical heat flux of 17 W/cm^2 is obtained.

A drawback to pool boiling is that variable heat transfer rates cannot be obtained since the only variable in pool boiling is the refrigerant. With jet impingement, many factors can change the heat flux including nozzle dimensions, liquid velocity and nozzle standoff distance. Pool boiling was found to produce sufficient heat flux values in order to cool the abrasive jet mentioned in Section 3.1.4 without resulting in the need for inconveniently large heat exchangers.

Kida et al. [37] study pool boiling heat transfer with liquid nitrogen to obtain heat flux results for nucleate boiling. The authors state that heat flux versus T_e values are difficult to match to other experiments since the material surface plays such a critical role during nucleate boiling. Due to this fact, it is difficult to predict exactly what length of heat exchanger would be required to obtain the desired abrasive jet temperatures.

2.3.3 Flow Oscillations in Internal Cryogenic Flows

In order to conserve liquid nitrogen, equipment which delivers the minimal amount required to cool the substrate surface had been proposed. Therefore the flow of cryogenic fluid at a small scale was of interest. While studying the flow of liquid nitrogen in micro-channels, Zhang et al. [38] found a temperature fluctuation with a frequency between 4 and 5 Hz. This frequency corresponded to the same frequency of bubble formation in the flow. Hetsroni et al. [39] also studied the pressure drop fluctuations with low amplitudes and high frequencies ranging from 3.6 to 6.6 Hz. Wu and Cheng [40] observed lower frequency oscillations that were said to be due to the fact that two phase and single phase flow alternate once the onset of nucleate boiling occurs. Qi et al. also found oscillations but with a much larger period of about 60 s [41]. This oscillation is thought to be caused by a vapour bubble forming before the outlet valve in the experimental setup. Sudden expansions in the flow line can therefore result in flashing and undesirable two phase flow. These oscillations must be minimized in order to obtain consistent cooling of the substrate surface.

Qi et al. [41] also mention a flow blocking phenomenon that occurs in a particular case of nucleate boiling. It is thought that the discharge rate of the vapour patch in the outlet valve is

less than the flow rate through the micro-tube. Qi [41] states that if the generated vapour rate is larger than the discharge rate of the vapour patch, the onset of nucleate boiling block will be observed. A critical mass flow is suggested which predicts the onset of flow instability. It is thought that if the mass flux is below this critical value, the vapour bubbles can be discharged freely. This flow blocking phenomenon is proposed to be responsible for the failure of the manifold design of Section 3.1.2 to produce liquid nitrogen at the four tube exits.

2.3.4 Impinging Cryogenic Jets and their Nusselt Number

The properties along the axis of the jet are critical when selecting jet impingement design parameters. Chorowski [42] used the jet temperature, measured with a T-type thermocouple, and a vane anemometer to determine the jet velocity in order to estimate heat transfer intensity for a cryogenic flow for applications in cryosurgery. The cone angle of the cryogenic jet was found to be constant at 13° independent of the various orifice sizes. Chorowski also experienced a large increase in jet temperature from the nozzle exit to about 10 cm. Past this point, the jet temperature remained constant. The large temperature increase in the region close to the nozzle exit was attributed to a large amount of air mixing with the jet. This fact demonstrates that jet temperature can also be controlled with the nozzle stand-off distance.

The Nusselt number is a dimensionless parameter in convective flow. It is used to describe the ratio of convective heat transfer to conductive heat transfer within the fluid.

$$Nu = \frac{h_c L}{k} \qquad \text{(2-14)}$$

where L is a characteristic length, h_c is the heat transfer coefficient and k is the thermal conductivity of the fluid under study.

Huang and El Genk [43] experimentally determined an equation for the average Nusselt number for an air jet cooling a uniformly heated flat plate. This Nusselt number was based on the radial coordinates of the impinging jet at the substrate surface. The authors found that as long as the dimensionless standoff distance H (standoff distance divided by nozzle diameter, D) was greater than 2.0, the maximum Nusselt number occurred at the stagnation point. For values below 2.0 the maximum Nusselt number was seen to occur at an r/D of 1.8-2.0. The maximum Nusselt at the stagnation point was seen to occur at an H of 4.7. This Nu_{max} was found to be

highly dependent on the dimensionless radial coordinate in the jet. In other words, when the stagnation heat transfer is maximized, the heat transfer in the periphery of the jet is not necessarily at a maximum.

The Nusselt number can also be calculated based on correlations which are dependent upon Prandtl number, Reynolds number, jet diameter and stand-off distance. Two such correlations are the Martin correlation [44] for a gas jet and the Dittus Boelter correlation for fully developed cryogenic flow [34].

3 Design of Cryogenic Abrasive Jet Micromachining Apparatus

A new CAJM apparatus was used to measure the solid particle erosion of PTFE, PDMS and high carbon steel using 25 μm alumina particles at various angles of attack and at temperatures between 17°C and -182°C. This chapter describes various prototype CAJM devices that were designed and tested. In the final design, instead of using a separate cryogenic jet as in Getu et al. [3], a heat exchanger was used to cool the pressurized abrasive air jet. This provided better temperature control than the apparatus used by Getu et al. [3], and ensured that the target surface was cooled symmetrically. This new device also enabled longer blasting periods.

3.1 Prototypes

Multiple prototypes were built and tested in order to achieve a blasting apparatus which was capable of machining material at temperatures between room temperature and -196°C. Initial prototypes focused on entraining a jet of liquid nitrogen with the abrasive particle after the nozzle exit.

3.1.1 Surface Flooding with Single Jet Entrainment

The previous liquid nitrogen setup created by Getu et al. [3] used a pressure pot, which contained a 500 mL Dewar full of liquid nitrogen pressurized by warm air at approximately 25 psig. Once pressurized, the liquid nitrogen flowed through an on/off plastic ball valve and out a 1.5 mm nozzle which was directed at the substrate surface. Getu et al used this apparatus to obtain initial erosion results on PDMS at surface temperatures of approximately -150°C. This equipment worked well for proof-of-concept, but it could not blast for extended amounts of time and the flow rate of liquid nitrogen was not controllable.

In the first prototype of the present work, a nozzle holder was designed which allowed the liquid nitrogen jet to be repeatably positioned with respect to the abrasive jet at various angles and standoff distances. This setup also allowed an extra liquid nitrogen jet to be positioned to either pre-cool the substrate surface or keep the abrasive jet cool before it hits the surface. Figure 3-1 shows the design of this nozzle positioning system. This apparatus includes a self pressurizing vessel which is kept at a constant pressure depending on the "pop" pressure of the relief valve. A pop valve rated at 35 psi was typically used. The liquid nitrogen is forced out of the vessel and through a ¼" stainless steel tube which contains a precise metering valve used

for flow control. Depending on the application, either a 1.5 mm nozzle or 0.76 mm diameter nozzle is used to direct a nitrogen jet on the substrate surface.
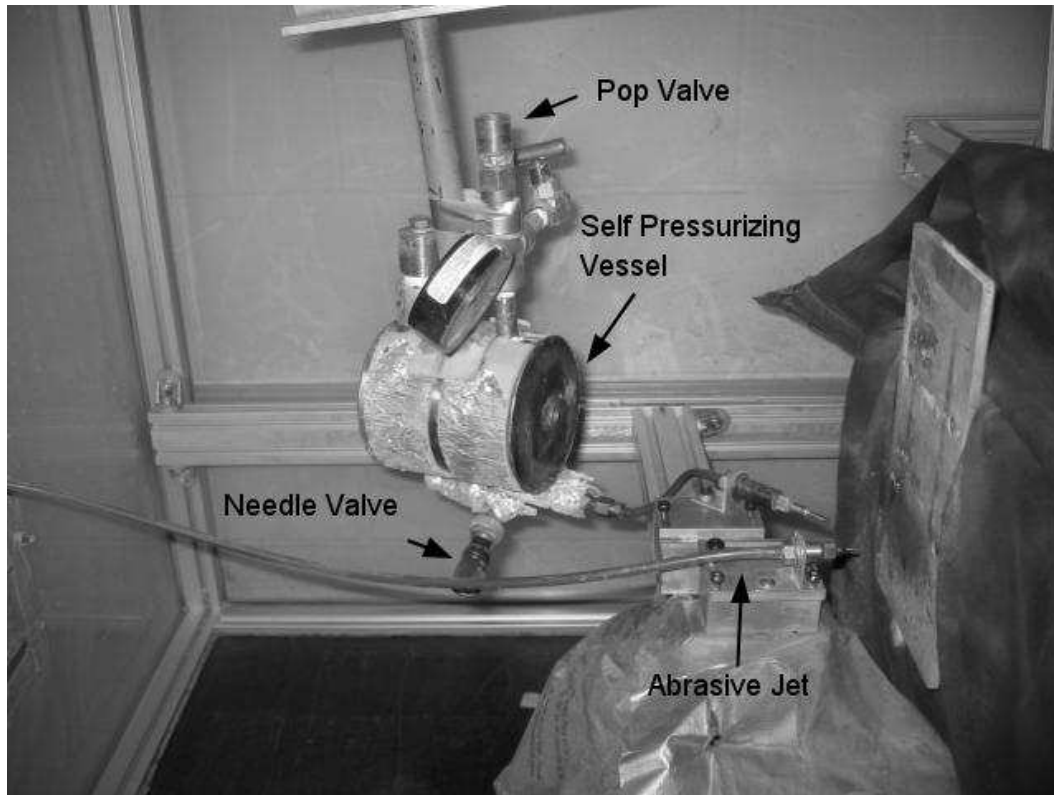
Figure 3-1 Liquid nitrogen self pressurizing vessel setup

Machining the surface at intermediate temperatures while only entraining one liquid nitrogen jet presented a few problems. One problem was unsymmetrical cooling of the surface. This was seen by investigating the profile of a stationary hole blasted in PDMS.
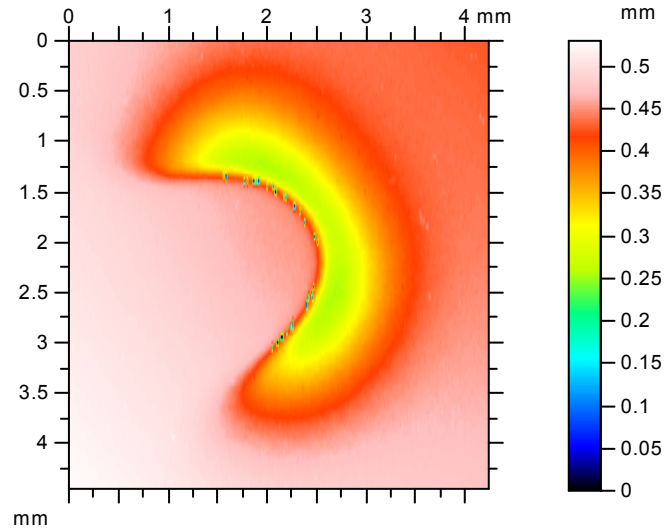
Figure 3-2 Contour plot of a hole drilled at an average temperature of -90°C using an external liquid nitrogen jet.
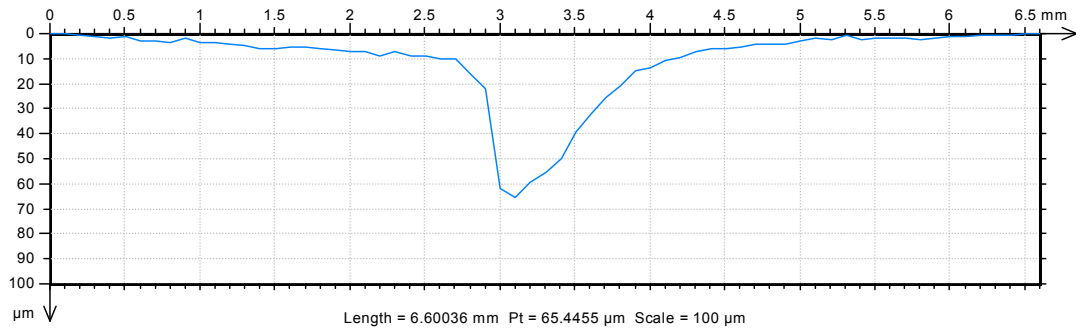
Figure 3-3 Cross sectional profile of a hole drilled with a jet lacking uniform temperature.

It was thought that since the amount of liquid nitrogen flooding the surface was decreased compared to the original flow rate used by Getu et al. [3], the heat flux created by the warm abrasive jet warmed portions of the surface back up to a temperature at which erosion did not occur in PDMS. Due to the obvious lack of symmetry of the profile, single jet entrainment at intermediate temperatures was not possible. Nevertheless, this self pressurizing apparatus could still be used for surface flooding to investigate erosion at the coldest temperature of -196°C.

3.1.2 Symmetrical 90 Degree Entrainment with Manifold Mixing

As a second prototype, a method which symmetrically injected liquid nitrogen into the abrasive jet in order to uniformly cool the substrate surface was constructed. This was designed

so that the injection nozzles had a repeatable position with respect to the abrasive nozzle. An acrylonitrile butadiene styrene (ABS) ring was machined which positioned four 18 gauge hypodermic needles symmetrically around the abrasive nozzle. It was intended that the liquid nitrogen flow through these small needles, mix with the abrasive jet and obtain a constant temperature over the jet footprint. Figure 3-4 shows a schematic the equipment used for the symmetrical entrainment setup. Figure 3-5 displays the manifold used to diverge the single stream of LN2 into four equal streams.
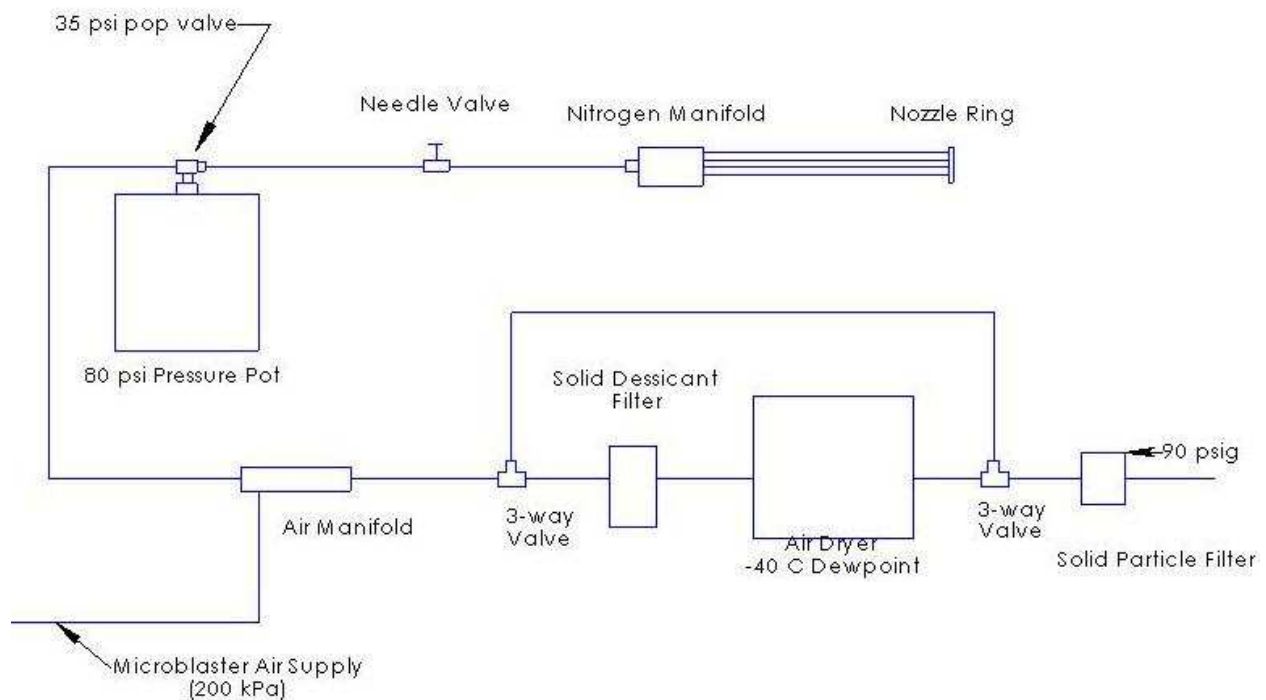
Figure 3-4 Schematic of the equipment setup for symmetrical external entrainment.
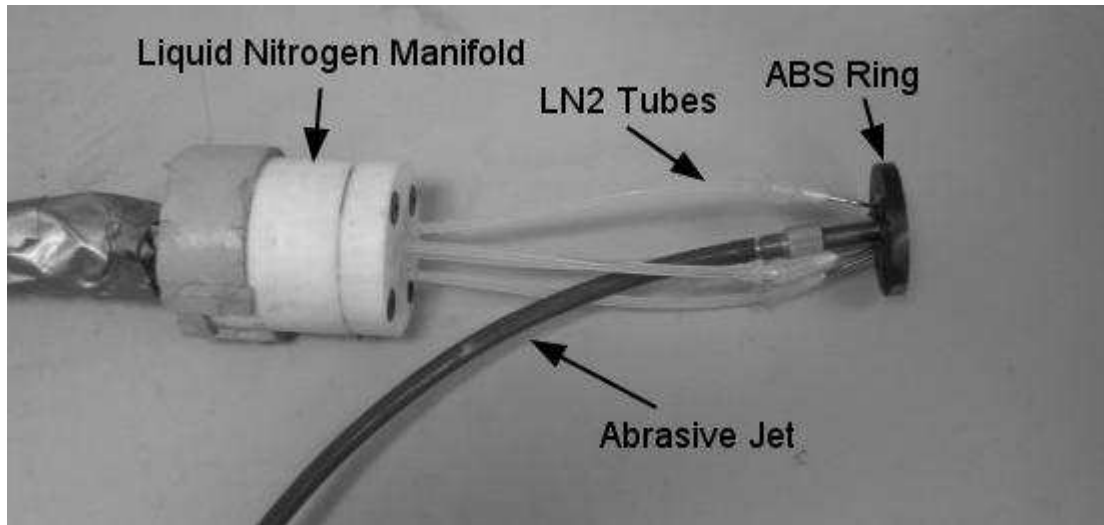
Figure 3-5 Nitrogen manifold and ABS ring in place with abrasive jet.

This method was unsuccessful in producing liquid nitrogen at the four needle exits. The likely reason was that the evaporation rate of liquid nitrogen in the lines could not match the flow rate. This caused only small amounts of gas to exit the nozzles which was not sufficient enough to cool the air stream. The blasting pressure was increased in order to overcome this issue but it resulted in the fracturing of the cold ABS manifold. It might be possible to cool this entire system in a liquid nitrogen bath, but that would not be an efficient use of LN2 and would lead to an unnecessarily complicated and potentially dangerous setup.

3.1.3 Upstream entrainment

A third prototype apparatus to attempt injecting the liquid nitrogen into the particle/air stream before the nozzle exit was also designed and constructed. It was thought that the air stream could be uniformly cooled to a temperature based on the amount of liquid nitrogen injected.

Figure 3-6Figure 3-6 and 3-7 show the smaller diameter inlet where liquid nitrogen was injected into the air/abrasive mixture.
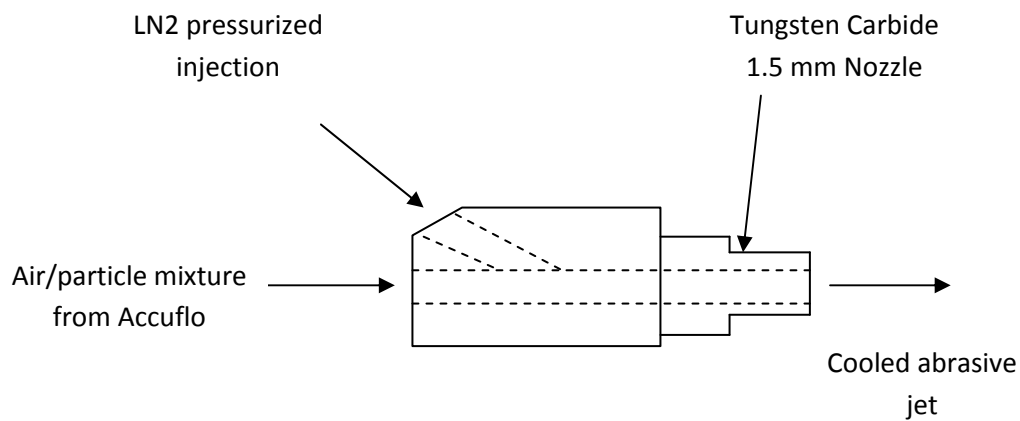
Figure 3-6 Schematic of the apparatus machined to allow upstream injection of LN2.
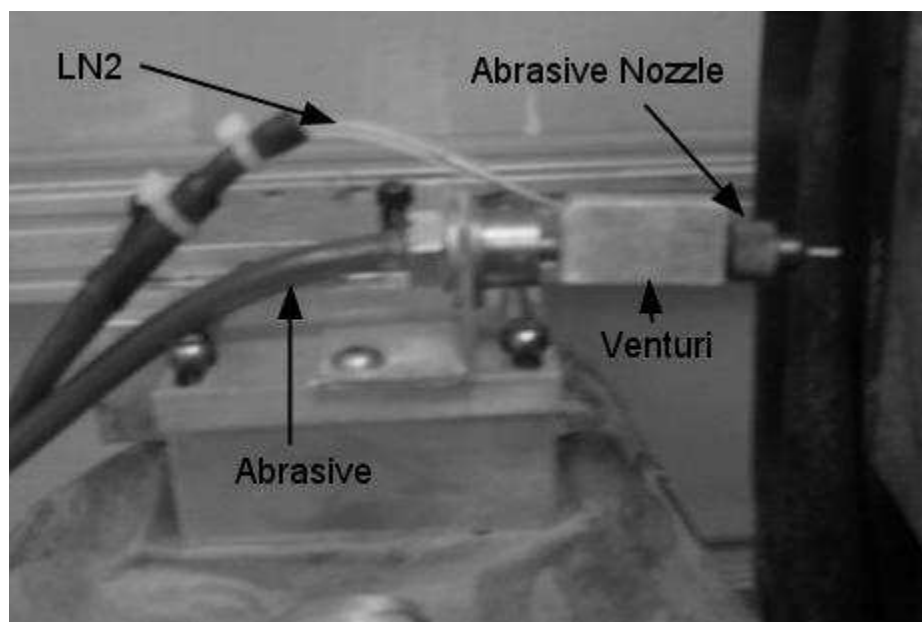
Figure 3-7 Upstream injection equipment in place.

This method of mixing the liquid nitrogen with the particle laden air stream resulted in an oscillatory flow due to the phase change of liquid nitrogen when it was initially introduced into the warm air stream. Therefore it was impossible to keep the jet at a consistent temperature over a period of time.

3.1.4 Indirect Heat Exchanger/Cryogenic Abrasive Jet Machining Setup

The final apparatus which solved all of the aforementioned problems involved the use of an indirect heat exchanger to cool the air and abrasive upstream of the nozzle exit. This final experimental setup was used in almost all of the experiments in this thesis to study the temperature dependence of erosion in PDMS, PTFE and high carbon steel. The CAJM apparatus consisted of an AF10 AccuFlo Micro-Abrasive Blaster (Comco Inc., Burbank, CA) that fed a mixture of abrasive media and pressurized air through an indirect heat exchanger of various lengths; i.e. 50, 64 and 80 cm long 6.4 mm outer diameter copper tubing immersed in liquid nitrogen (Figure 3-8). The resulting abrasive jet temperature was a function of the tubing length and the air pressure which affected the flow rate. This apparatus was similar to the low temperature gas blast setup of Urbanovich et al. [31], except that air was used as the carrier gas rather than nitrogen.

The target sample was clamped to the computer-controlled motorized stage to minimize deformation due to thermal shrinkage. A holding device was specially designed and fabricated (Figure 3-9) in order to consistently clamp the samples to the computer controlled stage at various angles of attack. The nozzle was a round high efficiency tungsten carbide nozzle (Comco Inc., Burbank, CA) with an inner diameter of 1.5 mm that could be rotated to produce various angles of attack.
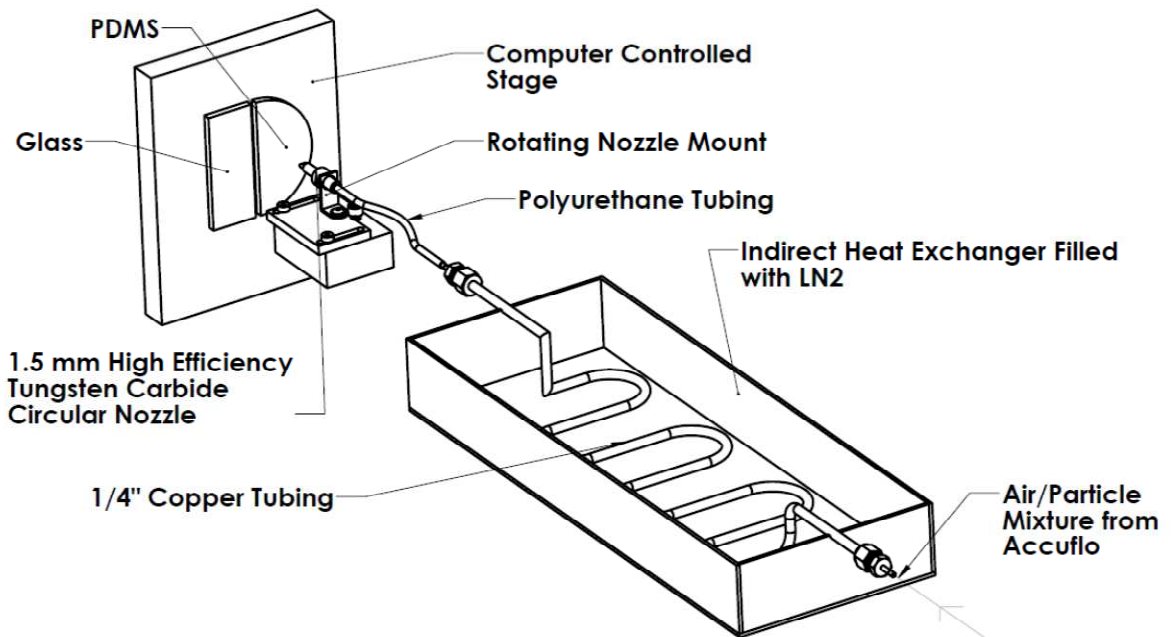
Figure 3-8 Schematic of final CAJM setup.
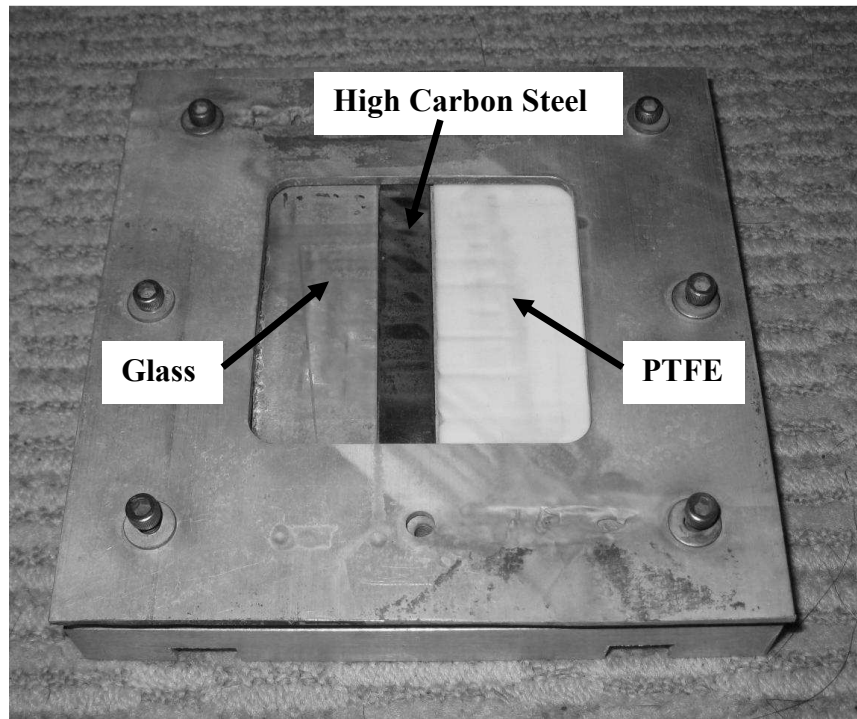
Figure 3-9 Sample holding device for the experiments done using PTFE, steel and glass.

This CAJM apparatus had some advantages over the system described in Section 3.1.1 [3] which used separate liquid nitrogen and abrasive jets, mixing the streams at the surface of the PDMS. In the present setup, the abrasive jet temperature could be controlled by changing the length of the heat exchanger, and the single cooled abrasive jet produced a much more symmetrical temperature distribution across the blast zone on the target surface. A drawback of the device was the coupling of the jet velocity, pressure and temperature. As the jet was cooled, the air density increased, and due to the conservation of mass, the velocity decreased for a given pressure at the inlet to the heat exchanger. This introduced a complication when comparing the erosion rates at various temperatures since the velocity could potentially change. Also, raising the pressure to increase the velocity at lower temperatures reduced the residence time within the heat exchanger, thereby increasing the temperature. In the present experiments, velocity and temperature were regulated using combinations of the heat exchanger length and pressure.

4 Cryogenic Abrasive Jet Machining of Polydimethylsiloxane at Different Temperatures

The elastomer polydimethylsiloxane (PDMS) is of particular interest in microfluidics because it is chemically resistant, biocompatible, and relatively easy to mold and seal [5]. It has been used for many novel components in a microfluidic chip such as valves [45], mixers and pumps. Previous research found that it was impossible to machine cured PDMS using AJM at room temperature with 25 µm aluminum oxide particles impacting at approximately 140 m/s due to its ability to absorb the energy of the impacting particles [3]. Getu et al. demonstrated that the polymer could be machined if cooled to approximately -150°C.

This chapter investigates how the angle dependency, magnitude and mechanisms of erosion change with temperature in the range of 17 to -178°C. An existing surface evolution model was used to predict masked and unmasked channels in the PDMS.

4.0.1 Preliminary Evidence for the Ability to Machine Polymers at Temperatures Above Glass Transition

The glass transition of PDMS is quoted in the literature as being -120 ºC[3]. It had been previously suspected that PDMS could only be machined below the glass transition. Using the self pressurizing setup of Section 3.1.1, a channel was machined under variable temperature. One of the unwanted characteristics of this apparatus was that at intermediate valve positions, it was possible for foreign particles to partially clog the needle valve and slow down the flow of liquid nitrogen. This phenomena was used to machine a channel at varying temperatures along its length. A T-type thermocouple was used to confirm the temperature at the beginning and the end of the channel by placing it in the two jets for approximately 15 seconds.
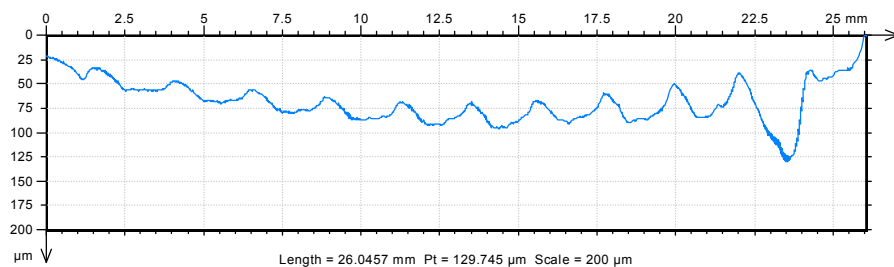
Figure 4-1 Lengthwise profile of the variable temperature channel.

Figure 4-1 shows a lengthwise profile of the resulting channel, with decreasing jet temperature gradually occurring from left to right (-60ºC at left and -196ºC at right). This result suggests that cryogenic erosion can begin at a temperature as high as -60ºC, although it is significantly less than that seen at -196ºC.

4.1 Experiments

4.1.1 Polydimethylsiloxane Sample Preparation

Sylgard 184 (Dow Corning Corp., Midland, MI, USA) was cured by mixing the cross-linking agent with the PDMS in the suggested mass ratio of 1:10. The mixture was then poured into a 100 mm diameter glass petri dish to a depth of approximately 2.5 mm, degassed under a vacuum of 84 kPa for 15 min, and then cured at 70°C for 4 h.

4.1.2 Characterization of Erosion Rate at Different Temperatures and Angles of Attack

The angular dependence of the erosion rate of the PDMS at -82, -127 and -178°C was obtained by machining channels with the nozzle inclined 15, 30, 45, 60, 75 and 90° to the surface in the "backwards scan" direction at either 0.5 or 1 mm/s (Figure 4-2) [1]. The nozzle to surface standoff distance (h) was kept constant at 20 mm, measured along the jet centerline. The jet temperature was measured using a T-type or a J-type thermocouple placed approximately in the centre of the jet on the PDMS surface. A thermocouple data logger was used to record the temperature every 2 s.
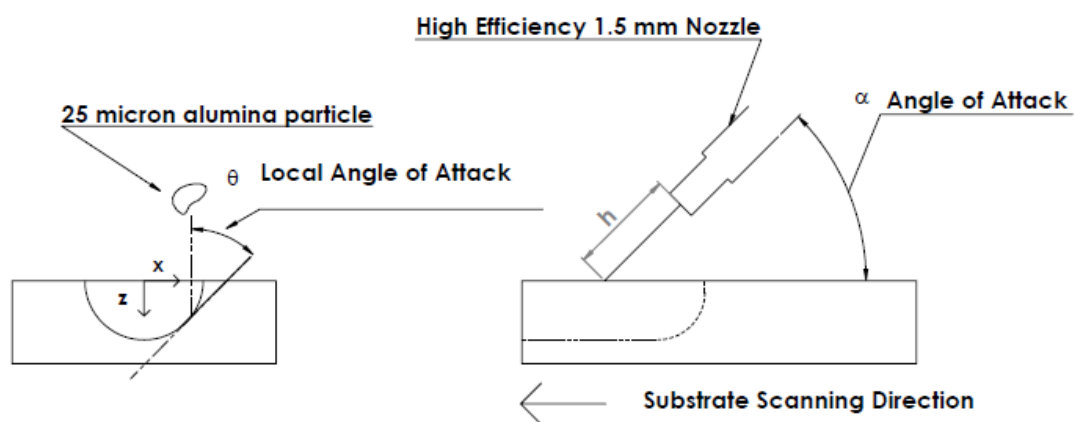
Figure 4-2 Front and side view of the abrasive jet nozzle orientation and direction of PDMS target movement during the machining of a channel in the "backwards" mode.

The microblaster was operated continuously, for reasons explained below, at each of the three temperatures while 25 mm long channels were machined in the PDMS and glass at each of the six angles of attack using 25 μm nominal diameter aluminum oxide particles. This increased the consistency of the blasting conditions amongst the channels at the different angles. Furthermore, each of these experiments was repeated three times. Blasting pressures were between 260 kPa and 400 kPa, depending on the desired jet temperature and heat exchanger length. Measuring the erosion rate using channels offered an advantage over the more traditional approach of drilling a hole in a stationary target. The uniformity of the channel cross-section along its length provided a good means of verifying the constancy of the abrasive media mass flow rate and velocity during the experiment.

The normalized erosion rate $G(\alpha)$, is the ratio of the volumetric erosion rate (volume of material removed per mass of launched particles), at a given angle of attack, $E(\alpha)$ to its value at normal incidence, $E(90°)$, i.e.

$$G(\alpha) = \frac{E(\propto)}{E(90°)}$$ (4-1)

The particle velocity depended only on the jet temperature and pressure, and was therefore constant for the duration of each experiment. For experiments performed at a given angle of attack, the scan speed and mass flow rate could be assumed to be the same for both the channels in the PDMS and the glass, since they were machined one directly after the other. However, as mentioned previously, the mass flow rate, $\dot{m}$, fluctuated up to 20% between experiments at the different angles. Under these conditions, the erosion rate of a material at any α is directly proportional to the centerline depth of the channel $z(\alpha)$, multiplied by the mass flow rate, i.e. $E(\alpha) \propto \dot{m}z(\alpha)$. In other words, since the present erosion rate experiments at a given angle of attack were performed at different mass flow rates $\dot{m}_\alpha$, than that at normal incidence, $\dot{m}_{90}$, then

$$G_P(\alpha) = \frac{\dot{m}_\alpha z_P(\alpha)}{\dot{m}_{90}\frac{\dot{m}_\alpha}{\dot{m}_{90}}z_P(90°)} \quad \text{and} \quad G_g(\alpha) = \frac{\dot{m}_\alpha z_g(\alpha)}{\dot{m}_{90}\frac{\dot{m}_\alpha}{\dot{m}_{90}}z_g(90°)} \tag{4-2}$$

where the subscripts '*p*' and '*g*' refer to PDMS and glass target specimens, respectively. Combining these two equations yields,

$$G_P(\alpha) = \frac{z_P(\alpha)}{z_P(90°)}\frac{z_g(90°)}{z_g(\alpha)}G_g(\alpha) \tag{4-3}$$

It has also been established that the erosion rate in glass, E_g, is proportional to the component of velocity, *v*, perpendicular to the surface raised to a velocity exponent (e.g., [46]), i.e.

$$E_g = C(v\sin\alpha)^k \tag{4-4}$$

where *C* is an empirically determined erosion constant that depends on the erodent particle size and shape, and on the target material. Therefore, for the present case of constant particle velocity, $G_g(\alpha)$ can be expressed as

$$G_g(\alpha) = \frac{C(v\sin\alpha)^k}{Cv^k} = (\sin\alpha)^k \tag{4-5}$$

Combining Eqs (4-3) and (4-5) yields an expression for $G_p(\alpha)$, based on measurements of channel depths in glass and PDMS machined at a constant particle velocity, provided that the same mass flow rate and nozzle scan speed are used to machine the glass and PDMS at a given angle of attack:

$$G_P(\alpha) = \frac{z_P(\alpha)/z_g(\alpha)}{z_P(90°)/z_g(90°)}(\sin\alpha)^k \tag{4-6}$$

A key point is that the depth ratios are only a function of temperature; i.e. they are independent of the jet velocity and mass flux. Therefore, the ratio of PDMS and glass channel depths at 90° measured in one experiment can be used to calculate $G(\alpha)$ at the other angles, where the term $sin(\alpha)^k$ accounts for the angle dependency of erosion in borosilicate glass [25]. For the same particles and glass substrates used in the present study, k=1.43 [46]. This method is also useful because mass flow rates do not necessarily have to be the same at the six angles of attack studied.

An optical profilometer (ST400, Nanovea, Irvine, CA) was used to measure the size and shape of the channel cross-sections. Channel depths were kept below 250 μm to ensure that the local slope of the substrate remained sufficiently small to not affect the erosion rate. The angular spread of the particle velocities within the jet were also considered to produce a negligible variation in the local impact angle. The channel depths were measured for the various angles of attack, collected from four locations every 5 mm along the channel length. The average of these four depths was used to calculate $G(\alpha)$ in Eq. 4-6.

The standard deviation of channel depths was calculated for one channel at each angle and temperature as a separate study. The channels had a relatively uniform depth, with a standard deviation less than 10% of the mean depth. As will be discussed in Section 4.3.2, the dependence of the channel depth on the impact angle varied with the temperature, displaying a more brittle characteristic (maximum material removal at 30-60°) at -178°C.

The mass flow rate could vary by as much as 20% between experiments due to uncontrollable variations in the powder flow within the pressurized reservoir [47]. Since the dependence of the erosion rate in borosilicate glass on the velocity and angle of attack was known from previous work [25], glass channels machined directly after each PDMS channel (i.e. at the same mass flow rate) were used in order to account for potential mass flow fluctuations. As will be discussed in Section 4.3.1, the glass channel depths at 90° could also be used to calculate the particle velocity at the jet centre for each temperature. The validity of this technique, however, relied on establishing that the erosion rate for the borosilicate glass samples was only a very weak function of the temperature. This was investigated by machining a channel while flooding the glass with a separate liquid nitrogen jet at approximately -196°C and then continuing to machine at room temperature with the cooling jet turned off (scan speed 1.5 mm/s, particle mass flow rate 140 mg/s). Although it has been claimed that cryogenic

temperatures increase erosion in glass [33], the present results suggest only a negligible decrease in the erosion rate at cryogenic temperatures. The average of three repetitions of the room temperature channel depth was 84 μm with a standard deviation of 3.9 μm (9 measurements, 3 from each of 3 channels). The average depth of the corresponding cryogenic channels was 77 μm with a standard deviation of 4.5 μm (9 measurements). This 8% difference, although statistically significant (t-test, 95% confidence), was relatively small, and was therefore assumed negligible for the purposes of inferring particle velocity at the different temperatures.

4.1.3 Measurement of Mass Flow Rate

As mentioned in Section 4.1.2, fluctuations in the mass flow rate are taken into account in the calculation of $G(\alpha)$ by simultaneous machining of shallow channels in both glass and PDMS under the same conditions. Therefore, Eq. (4-6) does not require knowledge of the particle mass flow rate. However, measures of mass flow rate were required in order to determine the volumetric erosion rate in PDMS at 90°, E(90°), the volumetric erosion per unit kinetic energy (Section 4.3.8), and to extract the particle velocity from the glass channel machined at 90° at the three temperatures (Section 4.3.2). The particle mass flow rates were measured by catching the particles exiting the nozzle in a 38 cm long 2.54 cm diameter clear plastic tube, over a one minute period. The measurement was complicated by the tendency for moisture in the room temperature air in the tube to condense, thus introducing errors in the gravimetric measurements. To avoid this, a diverging section of pipe, 18 cm long and approximately 100 mm in diameter, with filter paper at the end was attached to the tube to slow the air and particles, and water was used to wash the particles from the tube and pipe. The water was then boiled off and the aluminum oxide particles were weighed using a digital mass balance (±0.05 mg).

4.2 Surface Evolution Modelling

As defined in Section 2.2, the equation describing the depth, z, of feature shapes machined in ductile materials using AJM, as a function of time, t, can be expressed as [4]:

$$z_{t^*}^* = \left(E^*(x^*) \sqrt{(1 + z_{x^*}^{*2})} \right) G(\theta) \tag{4-7}$$

37

$G(\theta)$ expresses the dependence of the erosion rate on the local impact angle, θ, as defined in Fig. 2. It can be interpreted as the ratio of the erosion rate at the impact angle θ divided by the erosion rate at 90°. For erosion testing using gas blast type erosion rigs, Oka suggested [20] the following relation

$$G(\alpha) = (sin\alpha)^{n_1} \left[\frac{k_2 - sin\alpha}{k_2 - 1}\right]^{n_2} \tag{4-8}$$

where α is the global impact angle between the incident jet and an initially flat substrate, and n_1, n_2 and k_2 are curve fitting variables [20]. Equation (4-8) accounts for both the cutting action of erosion and material removal by repeated deformation. As has been previously done [4, 1], Eq. (4-8) was used to describe the dependence of the local erosion rate on the local angle of attack in the plane of the channel cross section, θ. For a brittle material such as glass, $G(\alpha)=(sin(\alpha))^k$, where k is the velocity exponent of Eq. (2-11). It should be noted that Eq. (4-8) is used for curve fitting purposes only, and that the physical significance of the constants n_1 and k_2 cannot be interpreted as described by Oka et al. for a variety of metallic materials [20].

Equation (4-7) was solved to predict the shapes and depths of the channels machined in PDMS at the various temperatures. To assess the accuracy of the surface evolution model, unmasked channels were machined at 90° using 1, 3, 5 and 7 nozzle passes at mass flow rates ranging from 85 to 220 mg/s and scan speeds of either 1 or 0.5 mm/s. As was done in the erosion rate experiments of Section 4.3.2, the entire area of each channel was scanned using the optical profilometer to determine the uniformity of the channel cross-section. As a separate study, three profiles were then taken, approximately 2 mm apart, for each set of nozzle passes. The average channel depth was quite uniform with an average coefficient of variation of 0.05 (standard deviation/average). Masked channels were also machined in the PDMS. Instead of using the nozzle standoff distance to normalize the profile dimensions, the spacing between the mask edges was used.

4.3 Results and Discussion

4.3.1 Centerline Particle Velocity and Surface Temperature

As mentioned in Section 3.1.4, the CAJM apparatus did not allow for the independent control of temperature and velocity, thereby complicating the identification of the temperature dependence of the PDMS erosion rate; i.e. the experiments at the three temperatures may have corresponded to three different particle velocities. As also discussed in Section 3.1.4, it was possible to measure the velocity indirectly at the various jet temperatures by using the shallow reference channels machined at 90° in borosilicate glass, a material with an erosion rate that was shown to be relatively independent of temperature. These velocities will be used in Section 4.3.6 to compare the absolute volumetric erosion per unit kinetic energy at the four blasting temperatures.

A complication however, is that the centerline depth of a channel represents an average jet velocity, since the jet scanned over a given channel cross-section. In order to obtain a measure of velocity at the centerline of the jet, it was necessary to correlate the depths of holes (stationary target) with the depths of channels machined under the same blasting conditions. The derivation of the relationship is given in Appendix A. Figure 4-3 shows the depths of channels machined at 90° in glass at room temperature using a scan speed of 0.5 mm/s at pressures between 50 and 200 kPa. It also shows the depth of a hole drilled for an arbitrary period (10 s in this case) under identical conditions.
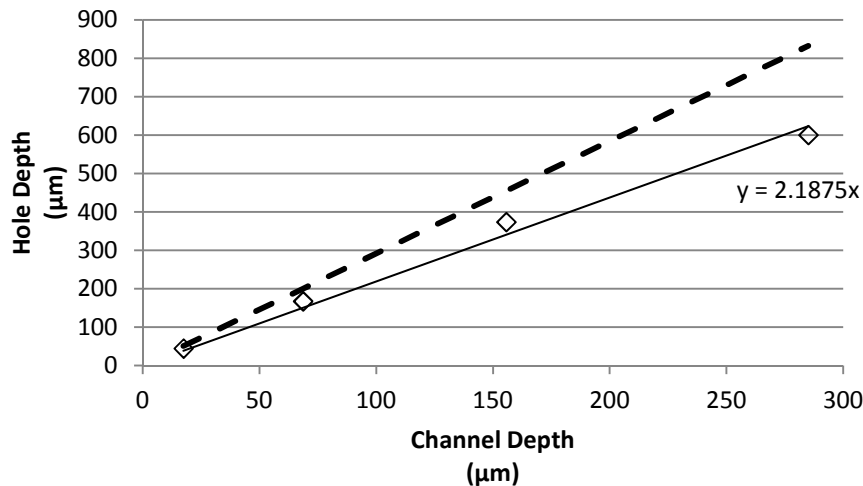
Figure 4-3 Measured (symbols) hole to channel depths for holes machined at α = 90˚ with dwell time Δt = 10 s, and channels machined at a scan speed vt = 0.5 mm/s.

The results indicated that a 10 s hole was consistently 2.2 times deeper than the channel (Appendix A). This relationship is only valid for holes and channels created at 90°.

For a jet at 90° having a distribution of particle flux, φ, the center depth of a shallow hole in glass, z, as a function of blasting time, t, can be expressed as [26]

$$\frac{dz}{dt} = \frac{C}{\rho_s} v^k \varphi(r) \tag{4-9}$$

where r is the radial coordinate within the jet, C is the erosion coefficient, ρ_s is the density of borosilicate glass (2,200 kg/m^3), v is the jet centre velocity (m/s) and k is the velocity exponent. Ghobeity et al. found the abrasive jet had a particle flux at the jet centre described by the function [46]:

$$\varphi(r = 0) = \frac{\dot{M}}{\pi} \left(\frac{\beta_w}{h}\right)^2 \tag{4-10}$$

where, $\dot{M}$ is the mass flow rate of aluminum oxide particles (kg/s), β_w is the nozzle focus coefficient and h is the standoff distance (0.02 m). For the erosion of borosilicate glass at room temperature using the same nozzle (Comco Inc, Burbank CA) and erodent as in the present experiments, it was found that $C=8\text{x}10^{-6}$ (m/s)$^{-k}$ [48], $\beta_w=18$ [9], and $k=1.43$ [46].

In summary, for each heat exchanger length in Table 4-5, the three channels that were machined in glass at 90° were used in the calculation of the jet centerline velocity which was assumed to be constant while machining continuously over all six angles of attack since temperature fluctuations were minimal and pressure remained constant. The averages of these three depths were converted into hole depths using Fig. 4-3. Equations (4-9) and (4-10) were then used to infer the jet centerline particle velocities, v, as shown in Table 4-5 for each of the three temperature ranges. The velocities varied because the blasting pressure was adjusted in each experiment to obtain the desired temperature.

The jet temperature at the surface of the PDMS (Table 4-5) was recorded before each channel was machined by positioning the jet over the thermocouple for 20 s. A large part of the variability was due to differences in the alignment of the jet and the thermocouple; e.g. a 1 mm

shift in the jet centerline produced a temperature difference of up to 10°C. When the nozzle remained stationary over the thermocouple, a maximum standard deviation in temperature of approximately 7°C was produced for the -178°C case. Other authors have reported temperature fluctuations in cryogenic jets of up to 5°C due to droplet impingement on the thermocouple [49].

Table 4-5 Jet centerline velocities and target temperatures measured during erosion rate experiments. The temperatures are the averages of the values measured before machining each of the 3 repeat channels at each angle for a given heat exchanger length.

Angle of Attack (Degrees)	Heat Exchanger Lengths		
	80 cm	64 cm	50 cm
	Temperature (°C)		
15	-182	-123	-91
30	-180	-123	-81
45	-180	-126	-85
60	-174	-133	-74
75	-176	-137	-79
90	-175	-125	-81
Ave(SD)	-178 (6)	-127 (7)	-82 (6)
Velocity (m/s) (Trial – 1,2,3)	47, 46, 46	30, 50, 45	39,59,50

The grand average and standard deviation (SD) correspond to all 18 temperature measurements (1 measurement for each of 3 repeats at each of the 6 angles). Velocities inferred from depths of glass channels machined at 90°.

Shipway [28] found that temperatures at the particle impact sites can increase if the thermal conductivity of the target material is relatively low. Since PDMS has a relatively low thermal conductivity of 0.16 W/m·K [Dow Corning Product Information], it was a concern that large local temperatures at the impact sites could play a role in erosion. It was also suspected that

particle collisions on the thermocouple embedded in the PDMS might result in false temperature readings. An experiment was performed which compared the temperature of a T-type thermocouple placed on the surface of the PDMS with that of a thermocouple embedded approximately 330 μm under the PDMS surface. In each case, the jet was positioned directly over the thermocouple for approximately 20 s. There was no statistically significant difference between these two temperatures (t-test, 95% confidence), indicating that heating due to direct impact against the thermocouple was negligible, and that temperature gradients within the PDMS surface region were small. It is thought that the extremely high convective heat transfer coefficient of the cold jet removes the heat generated by particle impact on both the thermocouple and the PDMS.

4.3.2 Dependence of Erosion Rate on Angle of Attack in PDMS

Figure 4-4 shows the dependence of the normalized erosion rate on the angle of attack, $G(\alpha)$ for the three temperatures investigated. As explained in Section 4.1.2 , the variability in PDMS erosion due to mass flow fluctuations and small differences in nozzle standoff distance from one experiment to the next was eliminated by referring to the depths of the glass reference channels machined immediately after each channel in PDMS (Eq. (4-6)).

(a)
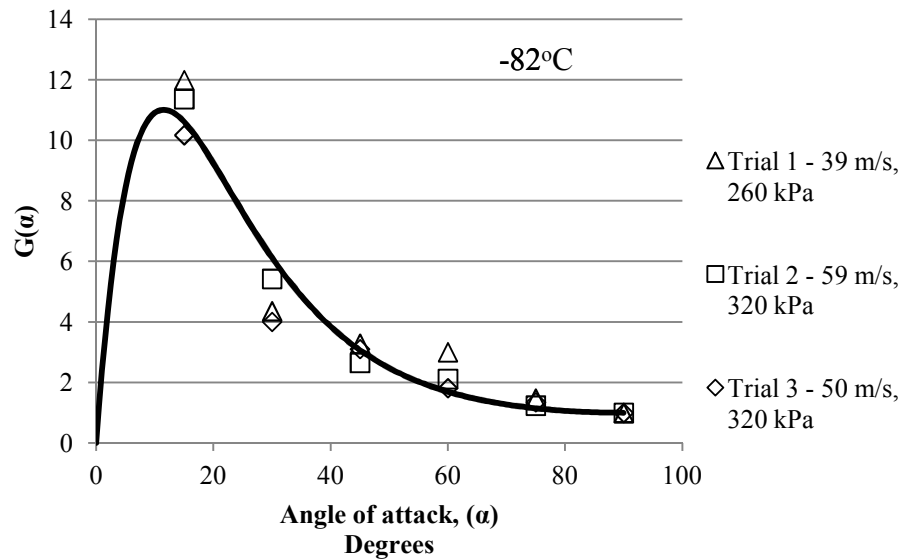
(b)
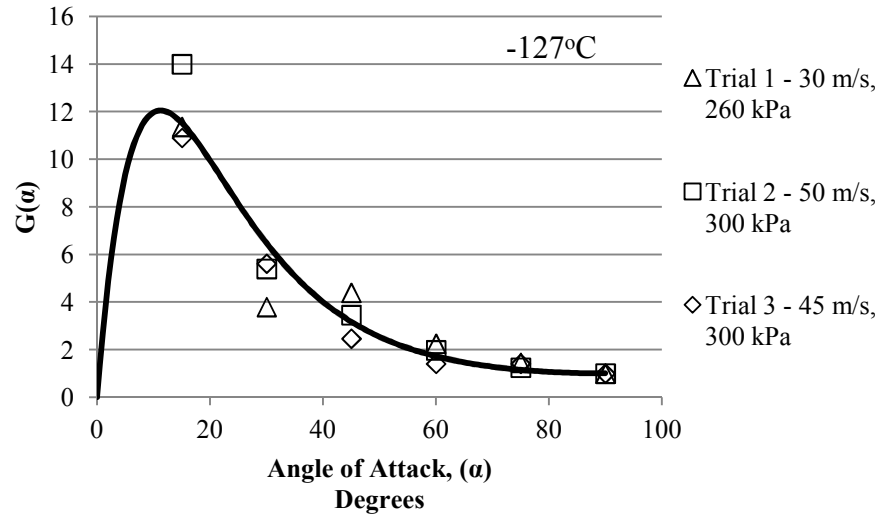
(c)
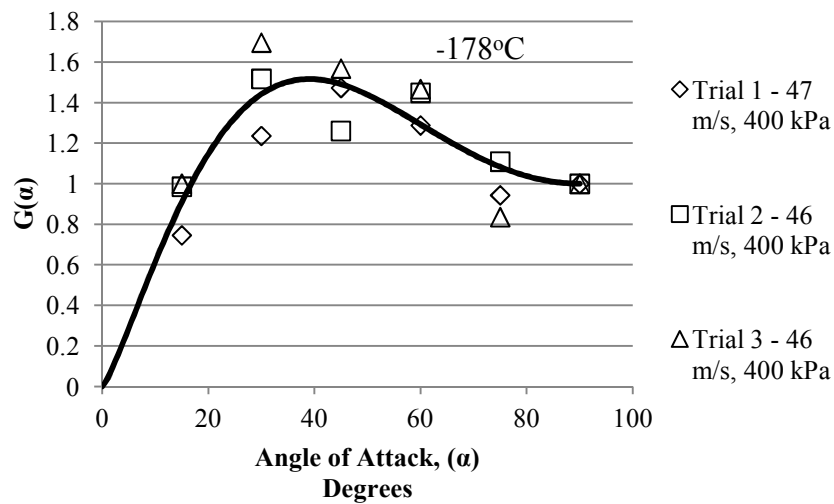
Figure 4-4 Normalized erosion rate as a function of angle of attack at: (a) -82°C, (b) -127°C, (c) -178 °C. Data points are the measurements and the solid line is the best-fit curve to G(α).

Each curve contains data points from the three repeat experiments. Jet centerline velocities varied between 30 and 59 m/s as can be seen in and Table 4-5. Since no trend is seen between the experimental scatter and particle velocity, it is concluded that *G(α)* was not affected by velocity within the range used. This is similar to the observations of Oka for the ductile

43

erosion of metallic materials [20]. Figure 4-5 plots the same $G(\alpha)$ results from Fig. 4-4 with temperature as the independent variable.
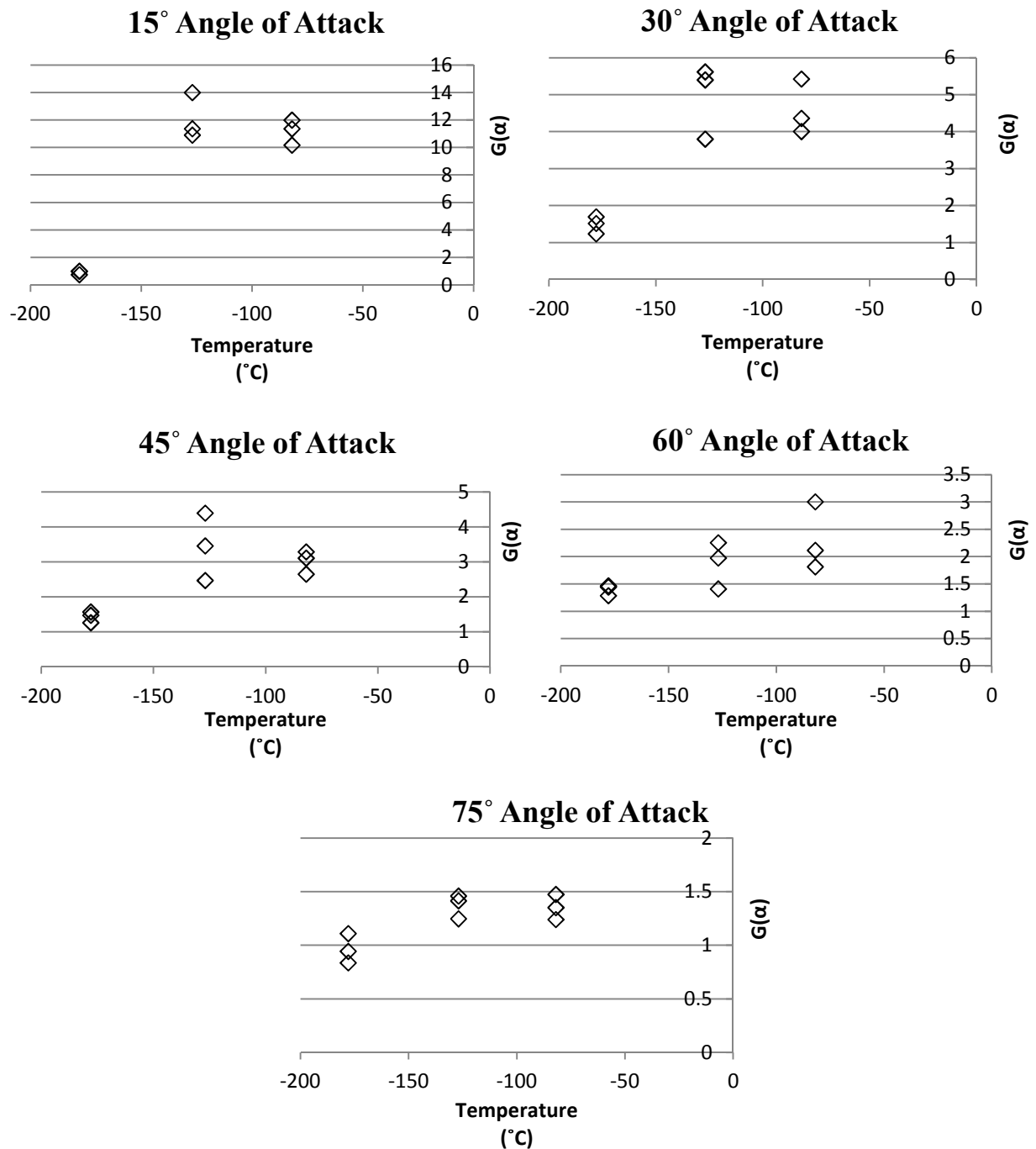
Figure 4-5 Normalized erosion rate as a function of temperature at all oblique angles of attack in PDMS.

Figure 4-5 clearly shows the magnitude of $G(\alpha)$ decreasing as the temperature is lowered.

Table 4-6 shows the measured PDMS volumetric erosion rates at an angle of attack of 90° for the three average temperatures shown in Table 4-5. The 90° erosion rate at -178°C was approximately 15 times larger than that at the two lower temperatures. The low erosion rates in Table 4-6 for Trial 1 (56 and 63) were due to the lower pressures and hence particle velocities in these two experiments (Table 4-5).

Table 4-6 Volumetric erosion rate of PDMS at normal incidence as a function of temperature.

	Erosion rate at 90° (mm^3/kg)		
Trial	-178°C	-127 °C	-82°C
1	1065	56	63
2	995	74	81
3	907	80	83

As has been previously done [4, 1], Eq. (4-8) was used to describe the dependence of the local erosion rate on the local angle of attack in the plane of the channel cross section, α. For a brittle material such as glass, $G(\alpha)=(\sin(\alpha))^k$, where k is the velocity exponent of Eq. (2-11).

The curve fits in Figure 4-4 were obtained by fitting Eq. (4-8) to the data points using the curve fitting tool, which uses a generalized least squares fitting method, in Matlab (MathWorks, Natick MA), to obtain k_2, n_1 and n_2. The variable n_1 was constrained to be between 1 and 2 since it represents the vertical component of erosion [20]. Table 4-7 gives the curve fit variables for each of the three temperatures.

Table 4-7 Best-fit variables of Eq. (4-8) for the curves of Figure 4-4.

	Temperature		
Variables	-82°C	-127°C	-178°C
n1	1	1	1.26
k2	1205	1828	1.42
n2	6034	9361	1.58
R^2	0.97	0.98	0.90

The $G(\alpha)$ curves for -82°C and -127°C show maximum erosion rates at shallow angles, suggesting ductile erosion. The $G(\alpha)$ curve for -178°C shows that the maximum erosion rate shifted to higher angles of attack, somewhere between 30° and 60°. This shift of the maximum erosion rate towards 90° reflects greater brittle erosion behavior, probably due to the physical changes corresponding to the glass transition which occurs in the vicinity of -120°C for PDMS [50, 3, 51].

4.3.3 Surface Evolution Prediction for Unmasked Channels in PDMS

To assess the accuracy of the surface evolution model in predicting the size and shape of deeper channels, unmasked channels were machined at 90° using 1, 3, 5 and 7 nozzle passes at mass flow rates ranging from 85 to 220 mg/s and scan speeds of either 1 or 0.5 mm/s. As was done in the erosion rate experiments of Section 4.3.2, the entire area of each channel was scanned using the optical profilometer to determine the uniformity of the channel cross-section.

Again, as a separate study, three profiles were then taken, approximately 2 mm apart, for each set of nozzle passes. The average channel depth was quite uniform with an average coefficient of variation of 0.05 (standard deviation/average).

The shapes of the unmasked channels machined in PDMS using multiple passes of the nozzle were predicted using Eq. (4-7). Since the solutions are symmetrical about the centre of the channel, only half of the profile is solved in order to minimize calculation time. Ghobeity et al. [46] and Getu et al. [4] obtained the erosive efficacy of the jet (E^* in Eq. (2-11)) by curve fitting a shallow first-pass profile, where the slope dependence of erosion in Eq. (4-7) can be ignored so that:

$$z_{t^*}^* = E^*(x^*) \qquad (4\text{-}11)$$

The functional form of E^* used in [46] was inappropriate for the present cryogenic jets, so a seventh degree polynomial was used to fit the first-pass channel profiles at each temperature. Equation (4-7) was then solved using a numerical method of lines procedure (MathCAD 14.0, Parametric Technology Corp. Needham, MA) as described in [1]. Figure 4-6 compares the experimental unmasked channel depth profiles with the predictions obtained from Eq. (4-7).

(a)

(b)

47
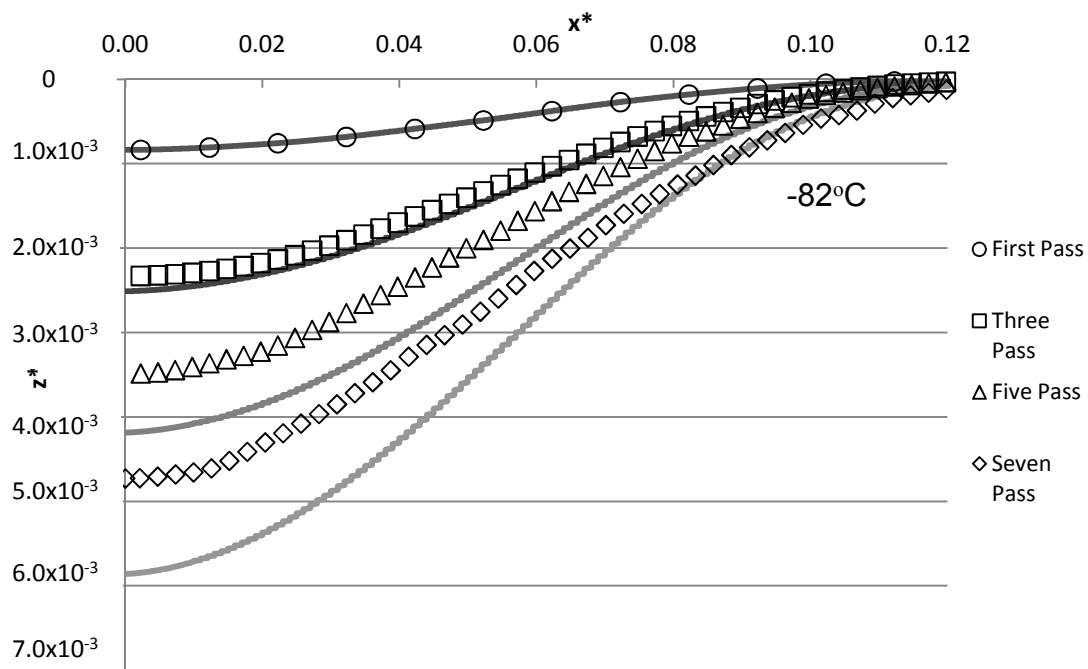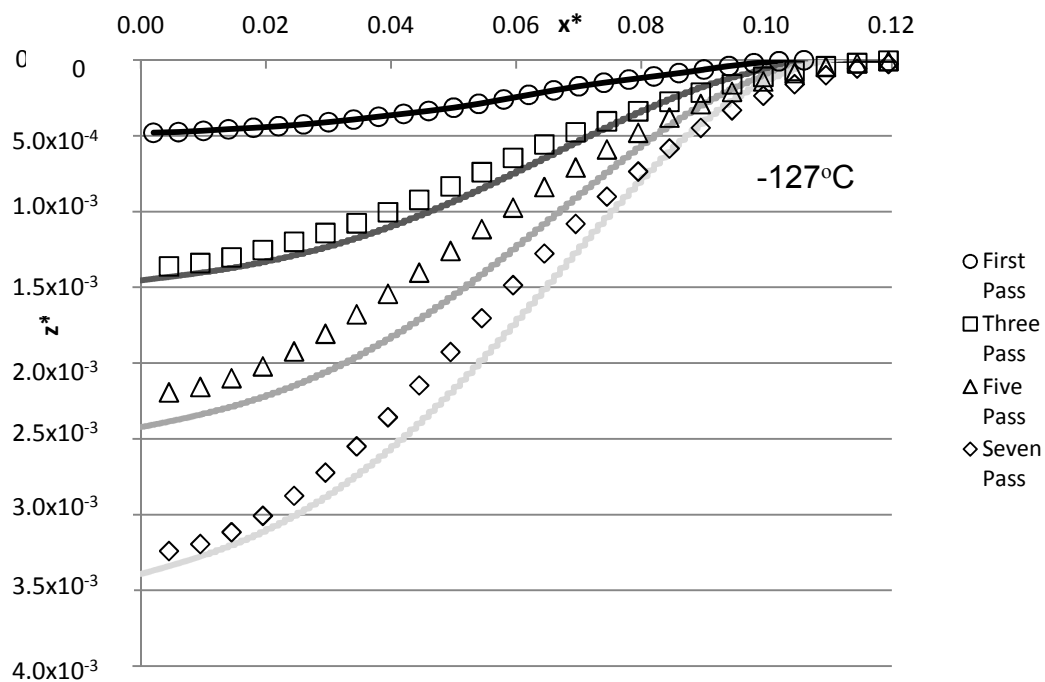
(c)
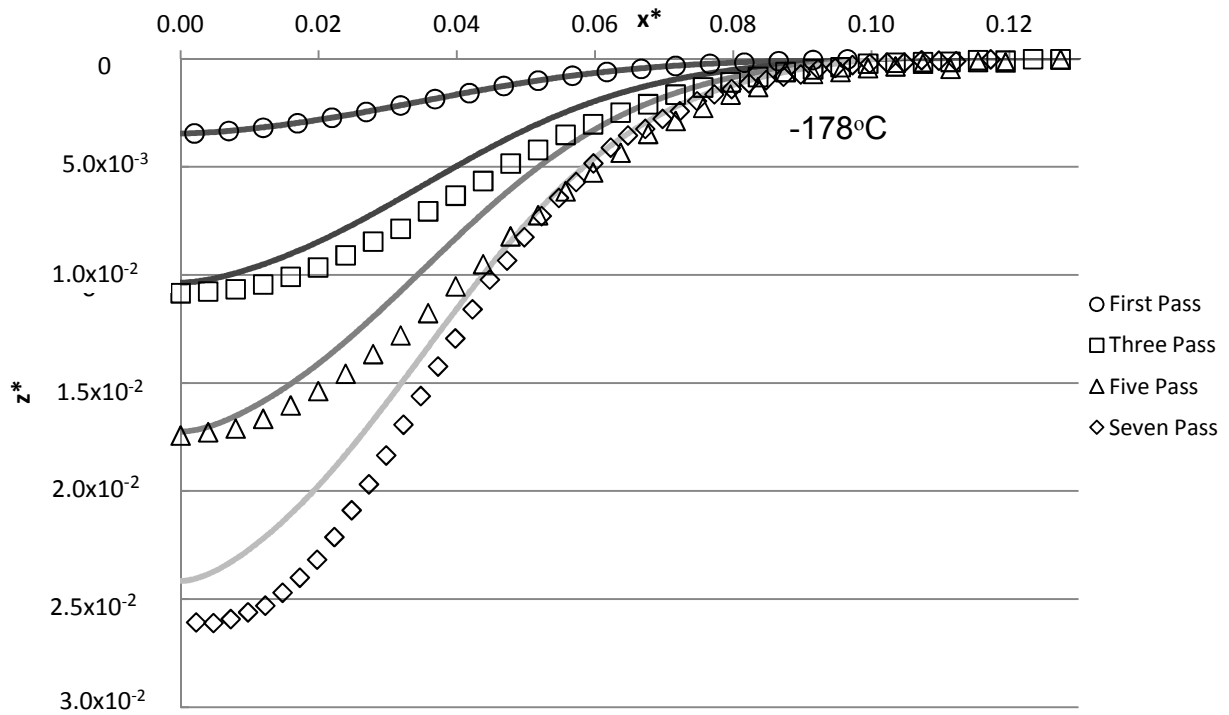
Figure 4-6 Comparison of measured channel profiles (symbols) and predictions (solid lines) of Eq. (4-7) for machining at: (a) -82°C, (b) -127°C, (c) -178°C. Note the change in depth scales at each temperature. 90° angle of attack.

Table 4-8 Percentage error in predicted channel depths (90° angle of attack).

Channel Depths (μm)				
- 82 °C				
Passes	Predicted	Experimental	% Error	Depth/pass (μm)
1	17	17	0	17
3	50	47	6%	15
5	84	70	17%	12
7	117	95	19%	13
- 127 °C				
Passes	Predicted	Experimental	% Error	Depth/pass (μm)
1	10	10	0	10
3	29	27	7%	9
5	48	44	8%	9
7	68	65	4%	11
- 178 °C				
Passes	Predicted	Experimental	% Error	Depth/pass (μm)
1	67	67	0	67
3	202	217	-7%	75
5	337	348	-3%	66
7	472	520	-10%	86

Table 4-8 shows that the largest over prediction of the profiles occurred for deeper channels at higher temperatures. This increased error may be due to the reduction in the erosion rate caused by an increase in particle embedding at the higher temperature (see Section 4.3.5). For example, at -82°C, Table 4-8 indicates that the per pass centerline depth increment decreased from 17 μm during the first pass, to a constant value of approximately 12 μm after the 3rd pass. It is

hypothesized that this was due to the effect of an increasing number of embedded particles, reaching steady state after the 3rd pass. In contrast, Table 4-8 shows that the per pass centerline depth increment was relatively constant at -127°C, indicating that the amount of embedding reached a steady state for all passes. At -178°C, the model under predicted the eroded profiles, indicating that reduced erosion due to particle embedding was not a concern.

Ductile materials, especially polymers, can exhibit an incubation period [15] during which the erosion rate increases with particle dose until a steady-state constant erosion rate is reached. Hutchings et al. [13] observed such an incubation period in the room temperature erosion of rubber, and attributed it to the initial growth of a fatigue crack network that evolved to a steady-state with a constant erosion rate. In contrast, the present experiments displayed an incubation period at -82°C where the erosion rate decreased to a constant value. As discussed in more detail in Section 4.3.6, this was thought to be caused by an increase in particle embedding to a steady-state embedded particle coverage and a constant level of surface shielding. Therefore, the $G(\alpha)$ measurements at -82°C represent an average erosion from a virgin surface to some level of particle embedding in a shallow channel that may not yet correspond to a steady-state level of embedding.

The $G(\alpha)$ curve at -82°C corresponding to steady-state erosion (constant embedded particle coverage) can be estimated by assuming that the magnitude of particle embedding is proportional to the velocity component normal to the surface [1], and that the erosion rate at steady state at 90° impact angle is 70% smaller than that measured in the first pass; i.e. Table 4-4 gives 17 μm/pass for the first pass and an average of 12 μm/pass thereafter. Therefore, the estimated $G(\alpha)$ for steady-state erosion at -82°C is approximated as

$$G(\alpha)' = \frac{[1 - 0.3\sin(\alpha)]G(\alpha)}{G(90)'} \qquad (4\text{-}12)$$

Figure 4-7 shows the new $G(\alpha)'$ points plotted with the original best-fit curve of Figure 4-4a. The shift in the data points is relatively small, except at 15° where the corrected values of $G(\alpha)$ are shifted significantly upward. This is simply a result of the reduced level of embedding and hence surface shielding predicted by Eq. (4-12) for this small normal component of the impact velocity.
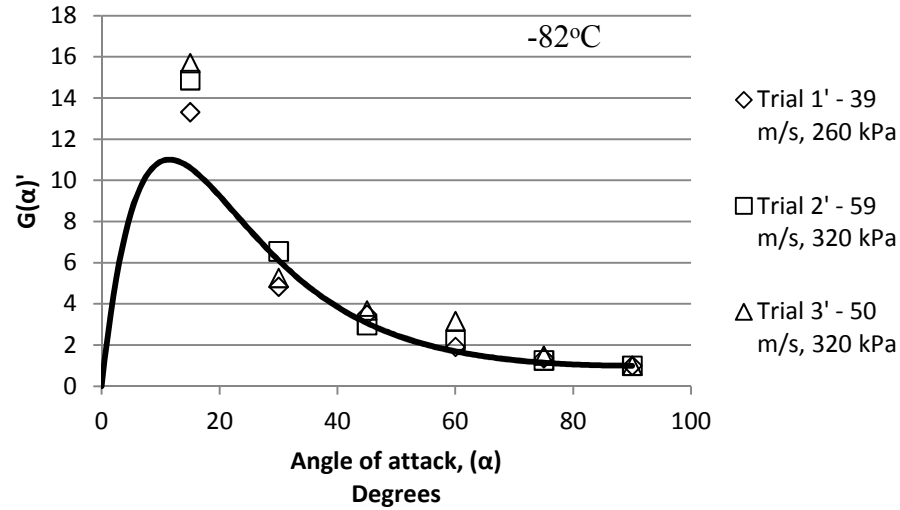
Figure 4-7 G(α) altered (data points) to account for the incubation period seen at -82°C. Original fit (solid line) from Figure 4-4 Normalized erosion rate as a function of angle of attack at: (a) -82°C, (b) -127°C, (c) -178 °C. Data points are the measurements and the solid line is the best-fit curve to G(α).

Similarly, the surface evolution predictions of Fig. 4a could be improved by calculating the erosive efficacy of the jet ($E*$ in Eq. (2-11)) using a fit to a channel profile corresponding to steady-state embedding rather than the first-pass profile. This would reduce the effective erosion rate and decrease the over-prediction of depth seen in the predictions of the fifth and seventh passes in Figure 4a (these cases had the greatest errors as seen in Table 4-4). For example, when the profile of 3 nozzle passes is used for $E*$, errors reduce to 8% for the fifth and seventh pass predicted depths.

4.3.4 Surface Evolution Prediction for PDMS Masked Channels

Masked channels were machined in PDMS at -181°C at 90° and -65°C at 15°. High carbon steel feeler gauge with a thickness of 1 mm was used as the mask material. Such thick masks were used in order to avoid buckling caused by particles impacting the mask creating a gap between the mask and substrate as described by Wensink et al. [52]. The edge of the feeler gauge was machined square to ensure a 90° edge with respect to the substrate. The masks were clamped to the surface using a special clamping device which used two plates to sandwich the substrate and mask together. A slot of approximately 5 mm in width and 60 mm in length was

machined in one of the plates so the substrate material and part of the masks could be exposed to the jet.
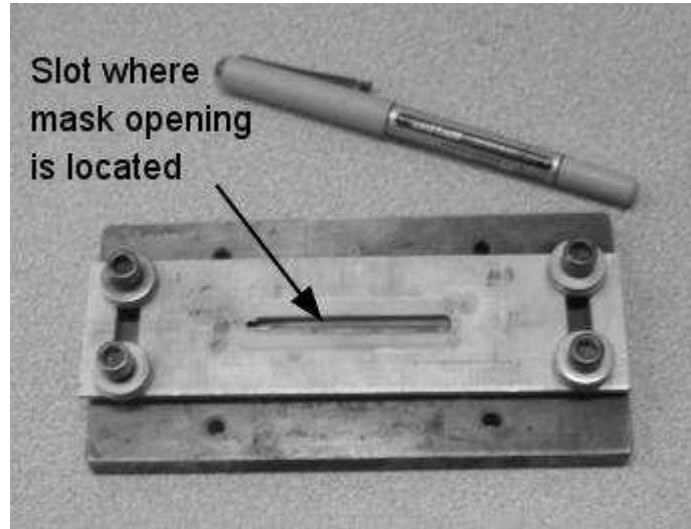
Figure 4-8 Mask holding device.

Once the masks were clamped in place, this spacing was confirmed using an optical profilometer by taking profiles every 5 mm along the 40 mm long channel. While blasting, the target oscillated rapidly in a direction perpendicular to the traverse direction at a frequency of 4 Hz and magnitude of either 6 mm or 10mm in order to provide a uniform particle flux across the mask opening as was done in [29].

Figure 4-9 shows the measured and predicted (Eq. (4-7)) masked channel profiles for various numbers of nozzle passes in PDMS at -180°C. Since the channels were symmetrical, the surface evolution equation for only half of the profile was solved to minimize calculation time. The average mask opening width was 350 μm with a standard deviation of 9.5 μm. The erosive efficacy was fitted to the first pass using an 11th order polynomial.

Figure 4-9 Predicted (solid lines) and experimental profiles (data points) for masked channels in PDMS at -180°C. The location of the mask edge is shown as a dashed line. The experimental first pass was used to fit the erosive efficacy (Eq. (2-11)) across the mask opening. 90˚ angle of attack.

Good agreement was obtained for the profile depths and the shapes in the middle of the channels, but a slight under-prediction of channel width occurred for the fourth and sixth passes of the nozzle. The measured profile points for these passes show an abrupt increase in profile width at the mask edge from the second pass. As explained below, the reason for this persistent observation of delayed erosion near the mask edge is unclear, because it was not attributable to either an incubation period or a reduced flux near the mask edge. Mask edge effects are typically seen to affect erosion about a particle radius (≈ 12 μm) away from the mask edge. Figure 4-9 shows that delayed erosion was present for more than 50 μm from the mask edge. In previous work using the same method to machine channels in glass, this erosion delay period near the mask edges did not occur.

It was hypothesized that the erosion rate of the target near the mask edge in Fig. 4-9 may not have attained steady state during the first two passes, due to the reduced particle dose in this region caused by particle collisions with the mask. To investigate whether PDMS exhibited such a transient in the in initial erosion rate, a sample of PDMS was uniformly machined at -181°C to a depth of 20 um by scanning it before the nozzle without any mask while simultaneously oscillating the stage at 6 Hz with an amplitude of 10 mm. However, when this preconditioned

PDMS surface was subsequently masked and machined as before, there was once again a pronounced delay in the erosion near the mask edge as in Fig. 4-9. Therefore, an incubation period was not the mechanism responsible for the erosion delay.

Figure 4-9 shows that using the first-pass channel profile to represent the erosive efficacy through the mask opening (Eq. (2-11)) is inadequate since it is initially too narrow and does not reflect the erosive flux across the entire mask opening. Ghobeity et al. [26] developed a procedure to infer an effective first-pass profile from the shape of a later, much deeper profile in which the local erosion rate depends on the slope. This method was implemented using the fourth pass of Fig. 4-8 to infer the erosive efficacy in Eq. (4-7), since at this point, the channel width had reached the mask edges. The following expressions were substituted into Eq. (4-7) in order to solve for $E^*(x^*)$.

$$(z^*_{t*})_i = \frac{z^*(x_i, t^*) - z^*(x_i, 0)}{t^*} \tag{4-13}$$

$$(z^*_{x*})_i = \frac{z^*(x^*_{i+1}, t^*) - z^*(x^*_i, t^*)}{x^*_{i+1} - x^*_i} \tag{4-14}$$
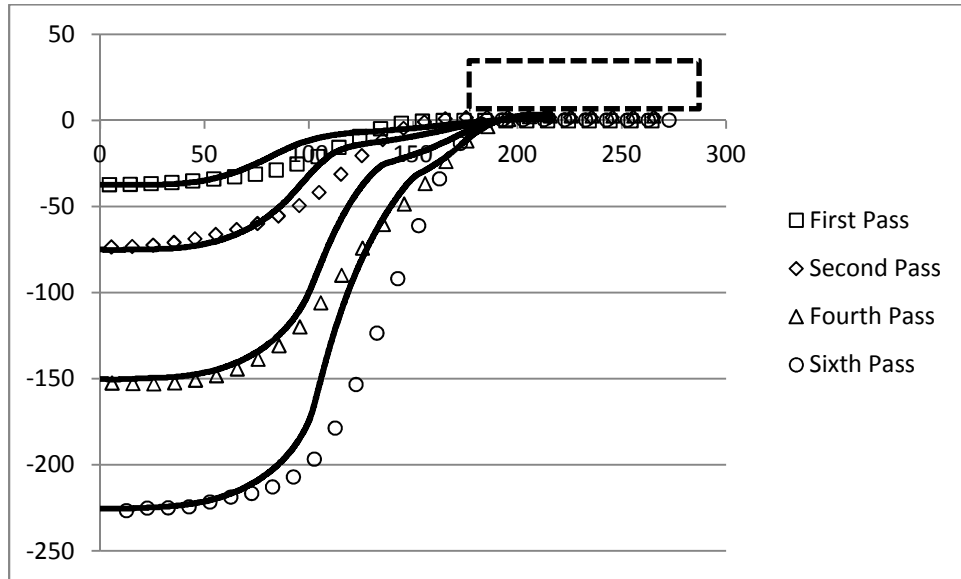
Figure 4-10 Predicted (solid lines) and experimental profiles (data points) for masked channels in PDMS at -180°C. The location of the mask edge is shown as a dashed line. The experimental fourth pass was used to infer the erosive efficacy (Eq. (2-11)) across the mask opening using the method of [26].

Figure 4-10 shows that this procedure resulted in better agreement near the mask edge, but the predicted fourth and sixth-pass profiles remained slightly too narrow, although the depth and the central portion of the channel profile were accurately modeled..

Figure 4-11 shows channel depths for 1, 3 and 5 passes of the nozzle in PDMS which was machined at -65°C at an angle of attack of 15° and a nozzle standoff distance of 43 mm. Previous work [53] showed that erosion rates were maximum at shallow angles at this temperature, suggesting that the erosion mechanism was predominantly ductile.
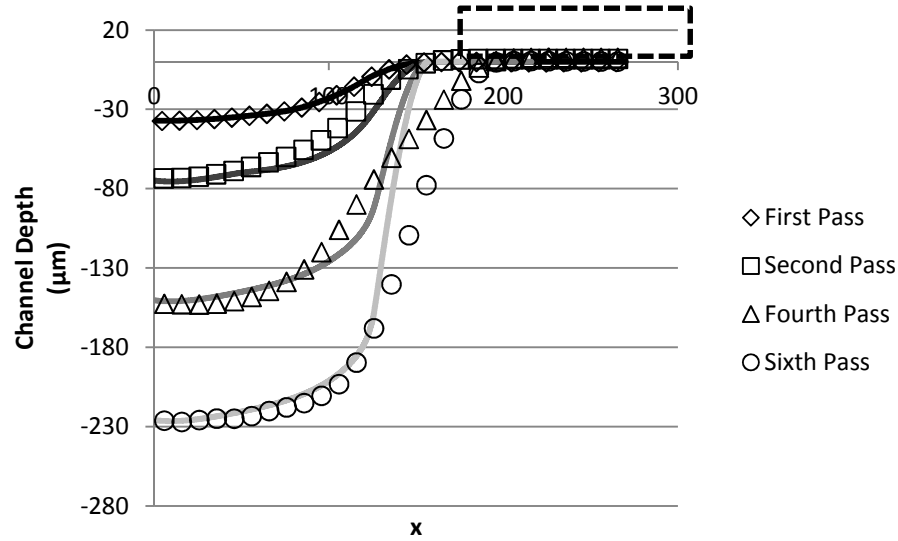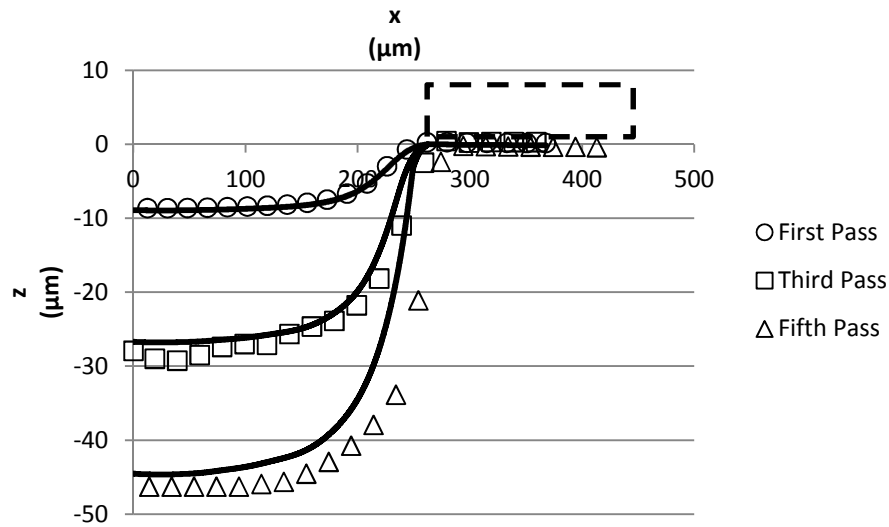

Figure 4-11 Predicted (solid lines) and experimental profiles (data points) for masked channels in PDMS at -65°C. The location of the mask edge is shown as a dashed line. The experimental first pass was used to fit the erosive efficacy (Eq. 2-11)) across the mask opening. 15° Angle of attack.

There was a good agreement between the experimental and predicted profiles. In contrast to the masked channels machined at -180°C (Fig. 4-9), there was no apparent delay in erosion near the mask edge, and the first-pass profile accurately reflected the distribution of the erosive efficacy (Eq. (6)).

Table 4-5 Percentage error in predicted masked channel depths in PDMS at two different temperatures.

Channel Depths				
PDMS				
- 65 °C, 15° Angle of Attack				
525 µm Mask Spacing				
Dosage Method: Nozzle Passes				
Passes	Predicted	Experimental	% Error	Depth/pass (µm)
1	8	8	0%	8
3	27	29	7%	11
5	45	46	1%	9
- 180 °C, 90° Angle of Attack				
350 µm Mask Spacing				
Dosage Method: Scan Speed				
Passes	Predicted	Experimental	% Error	Depth/pass (µm)
1	37	37	0%	37
2	75	73	-3%	36
4	150	152	1%	40
6	225	226	0%	37

4.3.5 Surface morphology and particle embedding in PDMS

Figure 4-12 indicates that there was much more particle embedding in the surface of the PDMS at -82 than at -178°C.

(a)   (b)
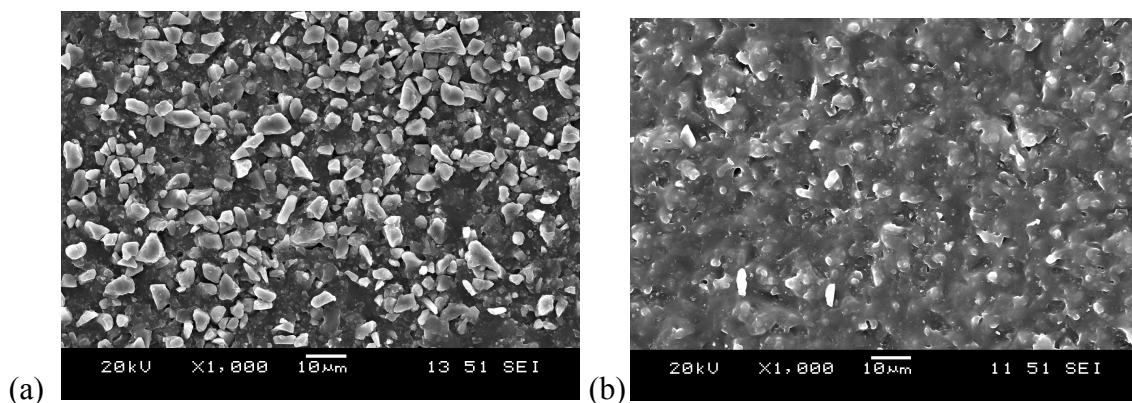
Figure 4-12 Scanning electron micrographs of PDMS blasted at 90° in a single pass at (a) -82°C and (b) -178°C.

This was also confirmed using energy dispersive X-ray spectroscopy (EDX) on two adjacent samples of PDMS machined at temperatures of -73°C and -180°C as shown in Figure 4-13. The presence of Al was widespread on the PDMS machined at -73°C, but almost nonexistent at -180°C.
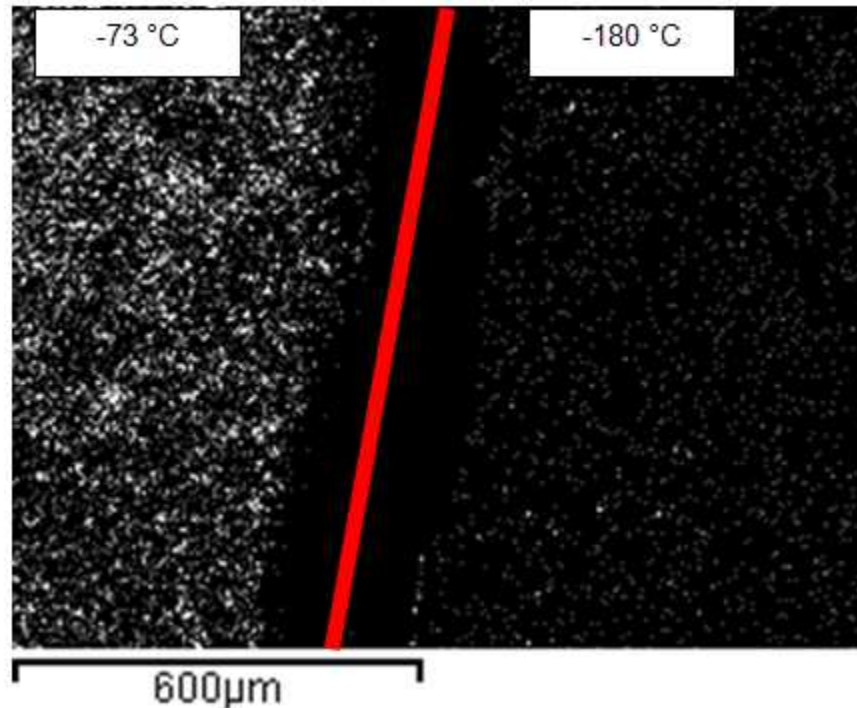
Figure 4-13 EDX mapping of the distribution of Al (white spots) on two samples of PDMS. The sample on the left was machined at -73°C and the sample on the right was machined at -180°C.

SEM photographs at an oblique view of approximately 50 degrees were taken of the surfaces machined at -73°C and -180°C. Both single and multiple particle impact surfaces are shown.
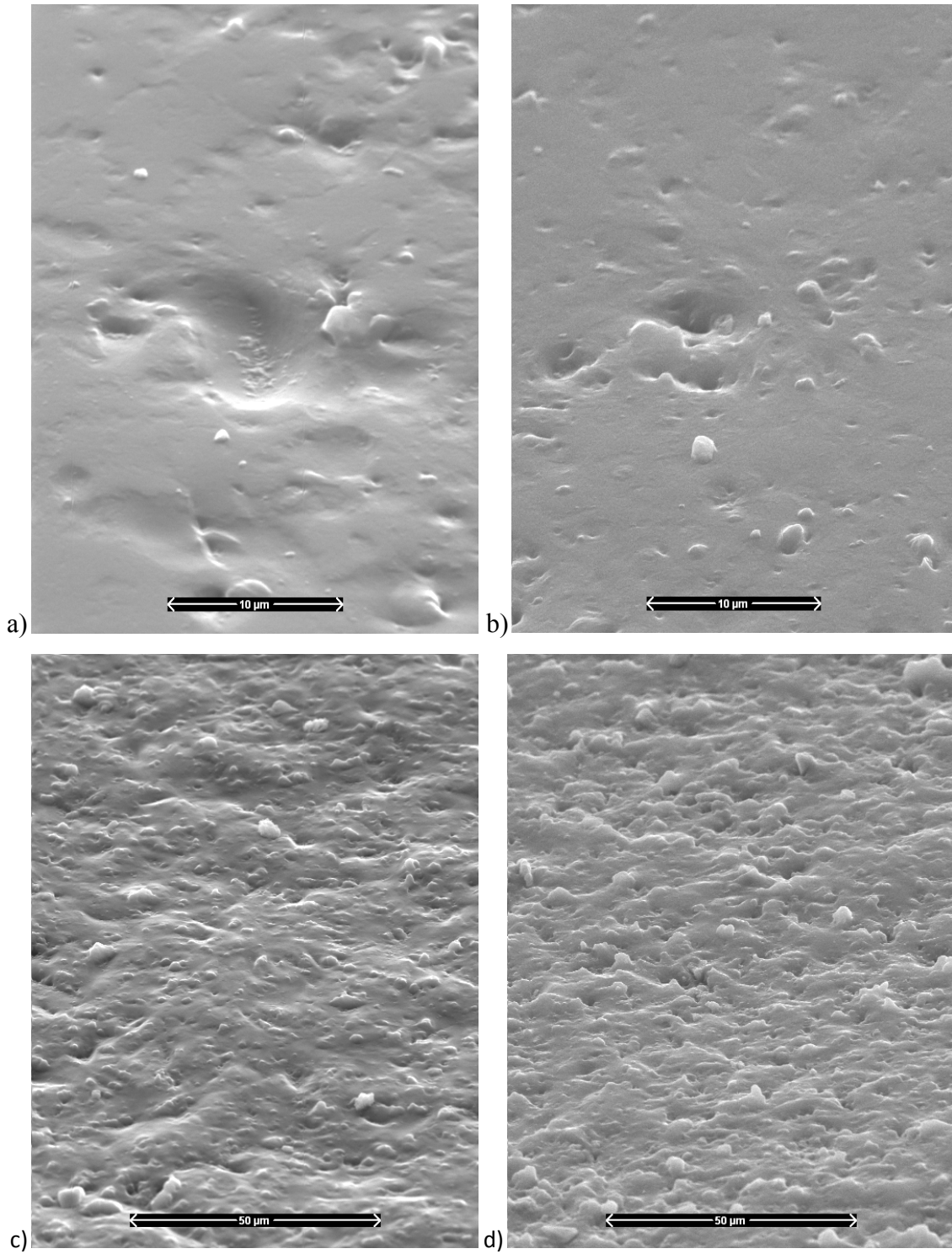
Figure 4-14 oblique views of the surface of PDMS a) single particle impact at -73°C, 30° angle of attack b)single particle impact at -180°C, 90° angle of attack c) repeated impacts at -73°C, 30° angle of attack d) repeated impacts at -180°C, 90° angle of attack.

The single impact site at the warmer temperature shows a smooth crater which is suggestive of micro-cutting whereas the impact site at the cooler temperature shows sharp ridges suggestive of material removal through crack propagation.

The -73°C surface, machined at a 30° angle of attack, appears to be slightly smoother than the surface machined at -180°C with gradual mounds. It is interesting to note that the surface does not show the typical transverse ridges synonymous with ductile erosion at oblique angles in most polymers. Barkoula and Karger reported that most elastomers tended to show more brittle features when examined under microscope [19]. The sharp ridges again appeared over the entire surface of the PDMS sample machined at -180°C.

Figures 4-15(a-e) are backscatter electron images obtained for the machined and untouched portions of the samples machined at -73 and -180°C.

e)
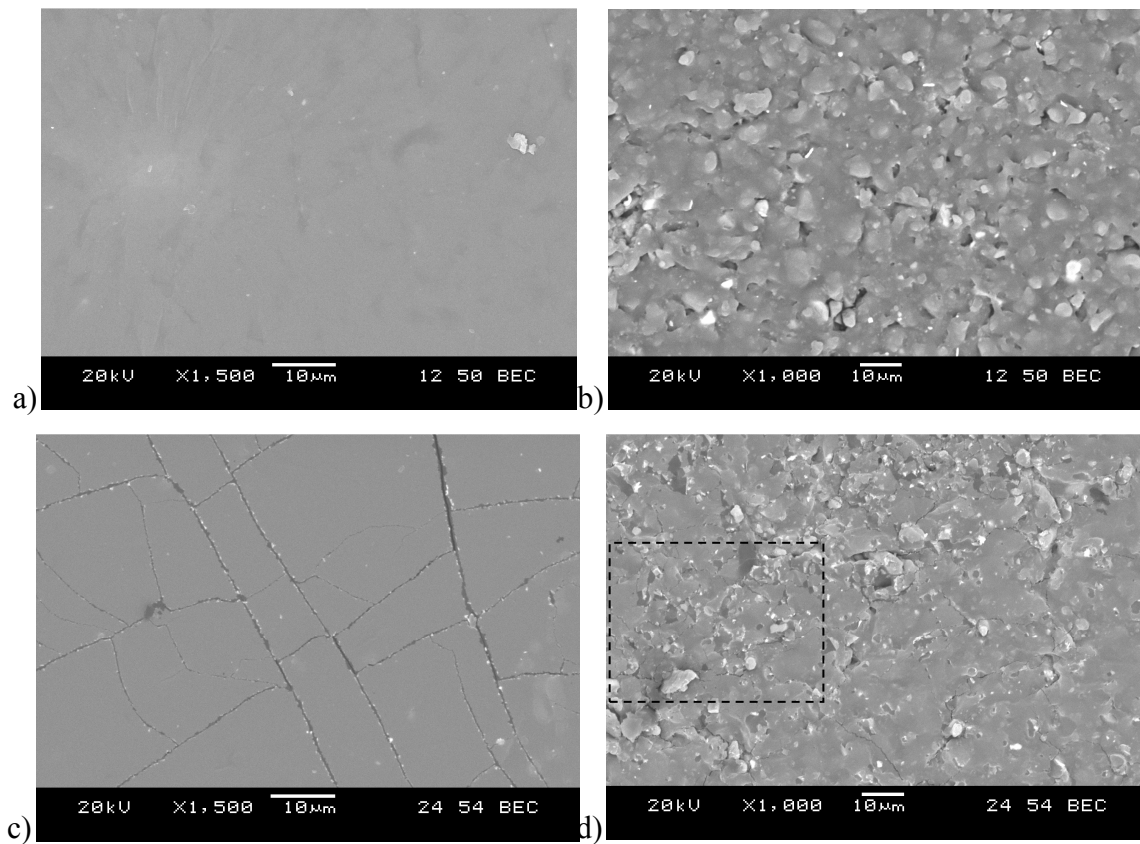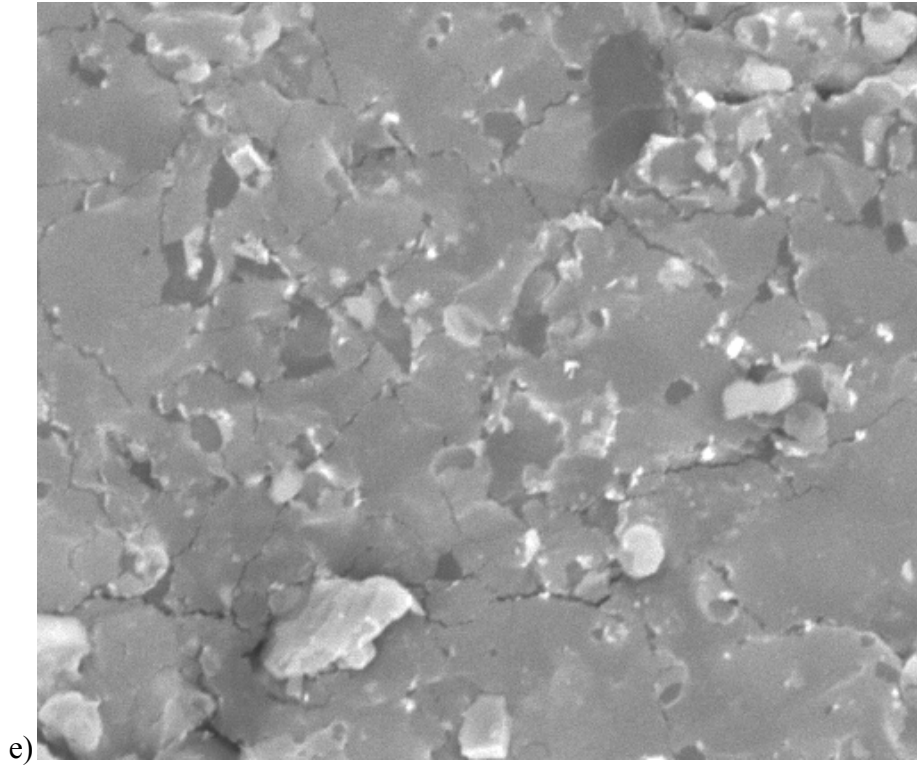
Figure 4-15 Scanning electron micrographs of PDMS: a) virgin surface that had been cooled to -73°C, b) machined surface at -73°C. c) virgin surface that had been cooled to -180°C, d) machined surface at -180°C, e) magnified view of dashed area shown in d.

Micro-cracks can clearly be seen for both surfaces at -180°C and are absent from either surface at -73°C. The microcracks in Figure 4-15c indicate that thermal strain caused cracking in the PDMS when it had been cooled to -180°C. Additional cracking due to particle impact is evident in Figure 4-15 d and e. These cracks originate from the impact sites and are therefore much more numerous and irregular than the thermal strain cracks of Figure 4-15c. Therefore, machining at -180°C introduces two effects that can influence the erosion rate: thermal strains generate cracks that might weaken the surface, and particle impacts generate cracks that are consistent with a brittle erosion mechanism.   It should be noted that cracks were not apparent in Figure 4-12b since secondary electron detection does not reveal microcracks of this size.

4.3.6 Volumetric Erosion per Unit Kinetic Energy in PDMS

In order to separate the effects of velocity and temperature, the volume of material removed per unit kinetic energy of the erodent was calculated, as shown in Figure 4-16 using the maximum centerline velocities in the jet (Table 4-1 and Fig. 4-4).

60
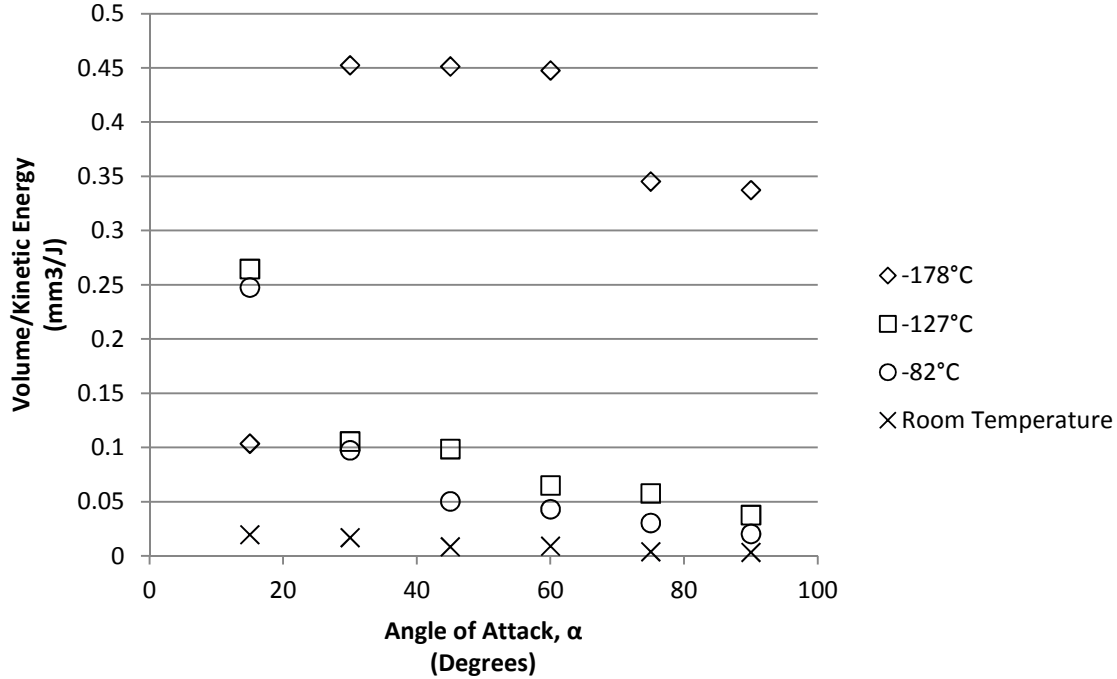
Figure 4-16 Volume of eroded PDMS per unit kinetic energy of incident particles as a function of impact angle for four temperatures.

It is interesting to note that curves at -82 and -127°C are very similar, suggesting that the erosion mechanism was the same. In contrast, between -127°C and -178°C the erosion mechanism changes markedly, producing greater erosion efficiency with a maximum in the vicinity of 45°. This is consistent with Fig. 4-4 where the $G(\alpha)$ curve at -178°C displayed a maximum erosion rate near 45°.

Although Fig. 4-16 provides an indication of machining efficiency, it neglects the energy cost of cooling which will increase approximately linearly with decreasing temperature. Therefore, machining at -178°C will require twice the LN2 as at -82°C.

4.4 Summary of Findings and Results

The dominant erosion mechanism in PDMS at temperatures of -82°C and -127°C appears to be ductile, because the normalized erosion rate, $G(\alpha)$, shows maximum erosion at angles of attack below 20°. The $G(\alpha)$ curve for -178°C shows a maximum erosion rate in the range of 30-60°, indicating a more brittle erosion mechanism below the glass transition temperature which is

in the vicinity of -120°C. The presence of micro-cracks in Fig 4-15e also suggest a brittle erosion mechanism at the coldest temperature of -178°C.

Glass channel depths at 90° were an effective way of inferring the velocity at the centreline of the jet at various temperatures. Glass reference channels machined at other impact angles during each PDMS erosion rate measurement, provided an accurate way of obtaining the $G(\alpha)$ curves that was independent of fluctuations in the mass flow rate.

The first pass profile fit to the erosive efficacy of the jet using a seventh order polynomial resulted in good unmasked surface evolution predictions. The largest error in channel depth prediction occurred at the warmest jet temperature, because of increased particle embedding.

The efficiency of PDMS machining, expressed as volume removal per unit kinetic energy, increased markedly below the glass transition of PDMS, being maximum between 30° and 60° angle of attack at approximately -178°C.

Masked channel profiles in PDMS were predicted very well with a maximum error of only 7%. The profile shape of a masked channel in PDMS at -180°C show there is a decrease in erosion near the mask edge. This causes initially narrower channels at small particle dosages (i.e. first and second pass) which render the first pass fit method inadequate for the deeper channels. Fitting the erosive efficacy using a pass which is beyond this small particle dosage resulted in better predictions of the deeper profile shapes. Preconditioning the surface by removing 20 μm appeared to have no effect on decreasing this effect. The channels machined in PDMS at -65°C showed good agreement with the predictions of Eq.(4-7). This indicated that no incubation period or effect of particle shielding or embedding occurred at these conditions.

5 Cryogenic Abrasive Jet Machining of Polytetrafluoroethylene at Different Temperatures

Inorganic materials such as glass and silicon were initially adapted from the integrated circuits industry as substrate materials for microfluidic chips. It is of interest to investigate the AJM of polytetrafluoroethylene (PTFE) in view of its superior inertness, high melting point of (340°C), and retention of ductility over a wide range of temperatures [6, 8], making it suitable for microfluidics applications.

This chapter investigates the dependence of erosion rate on temperature and angle of attack in PTFE and high carbon steel, often used as a mask material in AJM. The results are used to suggest an optimal machining condition which minimized mask wear while maximizing erosion in PTFE. Previously developed surface evolution models were used to predict the profile depths and shapes of micro-machined channels in PTFE.

5.1 Experiments

5.1.1 Cryogenic Abrasive Jet Machining Setup

The cryogenic machining setup is described in detail in Section 3.1.4. The abrasive jet air-particle mixture from a microblaster (Accuflo, Comco Inc., Burbank, CA) passed through a heat exchanger made of copper tubing immersed in liquid nitrogen [53]. Heat exchanger lengths of 50, 61 and 98 cm were used to produce jet temperatures of -76, -107 and -182°C respectively. A 1.5 mm high efficiency tungsten carbide nozzle (Comco Inc., Burbank, CA) was used to accelerate the particles toward the computer controlled stage where the samples were mounted. The nozzle was placed on a rotating mount which was used to change the angle of attack between the nozzle and the substrate materials.

5.1.2 Target Materials

Solid particle erosion experiments using 25 μm aluminum oxide particles were performed on 1.5 mm thick PTFE and 1 mm thick high-carbon steel (Rockwell C hardness of 48.5). As described in Section 4.1.2, in order to compensate for potential mass flow fluctuations and to determine the particle velocity in the centre of the jet, the depth of channels machined at normal incidence in 2.5 mm thick borosilicate glass (Borofloat, Schott North America, Elmsford, NY) were also measured immediately after each erosion test (Section 5.2.2).

5.1.3 Characterization of Erosion Rate at Different Temperatures and Angles of Attack

The dependence of the erosion rate on the nozzle angle of attack was measured at four temperatures (17, -76, -107, -182°C) for the PTFE, and at 17, -81 and -182°C for the steel. Channels were machined at 15, 30, 45, 60, 75 and 90° to the surface in the at a scan speed of 0.5 mm/s for the PTFE and glass, and 0.2 mm/s for the high carbon steel. Scanning at inclined angles was done in the "backwards" orientation, where the target motion (away from the fixed nozzle) was in the same direction as the jet flow along the channel [3]. The PTFE, steel and glass specimens were clamped adjacent to each other on the computer controlled stage. The nozzle to surface standoff distance (h) was kept constant at 23 mm, measured along the jet centerline. The central jet temperature was measured for 15 s at the beginning of each experiment using either a K-type or a J-type thermocouple with a 1-2 mm bead fixed to the PTFE surface. At each combination of angle and temperature, the microblaster was operated continuously while 25 mm, 12 mm and 20 mm long channels were machined in the PTFE, steel and glass, respectively, using 25 μm nominal diameter aluminum oxide particles. This ensured constant blasting conditions within a single experiment. Each of these experiments was repeated twice, with the exception of the results at 17°C, which were obtained from a single experiment. Blasting pressures at the colder temperatures were between 300 kPa and 400 kPa resulting in a range of jet centerline particle velocities between 23 and 49 m/s, depending on the desired jet temperature and heat exchanger length. As was done in Section 4.3.2, the glass channels were used to infer the erosion rate using Eq. (4-6). Since mass flow fluctuations of up to 20% between experiments have been reported previously with similar equipment [46], it was important to account for this variability by normalizing the erosion rate of the PTFE and steel by the erosion in the glass machined directly at the same mass flow rate. Borosilicate glass was a useful reference material because its erosion characteristics are well known [26], and are only a weak function of temperature [53]. Knowing the depth of the reference channels in glass, the dependence of the erosion rate of PTFE and steel on the angle of attack, α, can be expressed as was done in Section 4.1.2 [53]. As has been described previously, the glass channel depths at 90° could also be used to calculate the particle velocity at the jet centre for each temperature and the dependence of the erosion rate of PTFE and steel.

An optical profilometer (ST400, Nanovea, Irvine, CA) was used to measure the size and shape of the channel cross-sections. The angular spread of the particle velocities within the jet

were considered to produce a negligible variation in the local impact angle. The channel depths were measured at four locations along the channel length for the various angles of attack. The average of these four depths was used to calculate $G(\alpha)$ in Eq. 4-6.

5.1.4 Micro-machining of Masked Channels in PTFE

At -65°C, masked channels were machined in PTFE at 400 kPa and α=30°. The experiments were then performed at -180°C at 400 kPa and α=90° in PTFE. The mask consisted of two 1 mm thick steel strips (same steel as used in the erosion rate experiments), which was thick enough to remain flat in spite of the plastic deformation generated by particle impacts. The edges of the two steel masking strips were machined square, and they were tightly clamped to the target surface with gaps between 566 and 592 μm as shown in Table 5-4. Once the masks were clamped in place, this spacing was confirmed using an optical profilometer by taking cross-sectional profiles every 5 mm along the 50 mm long channel. While blasting, the masked target was oscillated rapidly in a direction perpendicular to the scan direction at a frequency of 4 Hz with an amplitude of at least 6 mm to create a uniform particle flux across the mask opening, as was done previously in [29]. The particle dose (g/mm^2), was controlled by either the number of nozzle passes or the scan speed (Table 5-4). Experiments showed that both of these methods produced identical results for the same particle dose (See Appendix B). Following the approach of [1, 3], the first-pass profile was used to determine the erosive efficacy of the portion of the jet within the mask opening, a method which is explained in Section 4.3.3. The first pass was fitted with a polynomial for each case except for the profile in PTFE at -180°C which was fitted with an exponential equation suggested by Ghobeity et al. [26] since a polynomial fit resulted in an unrealistic slope at the center of the channel.

5.1.5 Particle Velocity

The erosion rates at the different temperatures could not be directly compared since the particle velocity changed with the jet temperature [53]. To overcome this problem, erosion in PTFE was reported per unit kinetic energy of the particles in the centre of the abrasive jet. As was done in Section 4.3.2, the depths of the glass calibration channels were used to infer the jet centerline particle velocities, v (m/s), using the known mass flux and velocity distribution of the jet as follows:

$$v = \left(\frac{z\rho_s h^2}{\Delta t C \beta_w{}^2 \dot{M}}\right)^{1/k}$$

<div align="right">(5-1)</div>

where ρ_s is the density of the glass (2,200 kg/m^3), C is the erosion coefficient of glass (C=8x10^{-6} (m/s)$^{-k}$) [9], k is the velocity exponent for glass eroded with alumina particles (1.43), $\dot{M}$ is the particle mass flow rate in kg/s, β_w is the nozzle flow focus coefficient (18) [9], and h is the nozzle standoff distance (0.023 m).

5.2 Results and Discussion

5.2.1 Dependence of Erosion Rate on Angle of Attack in PTFE

Figure 5-1 shows the normalized volumetric erosion rate as a function of the impact angle, α, for PTFE at 17°C and the three cryogenic temperatures investigated. The normalized value, $G(\alpha)$, was obtained by dividing by the erosion rate at 90°. At room temperature, the erosion rate was nearly zero at 90°, and therefore the actual, rather than normalized, values were plotted in Fig. 5-1a. As described in Section 3.1.4, the velocity of the particles depended on both the blasting pressure and the degree of cooling of the air in the heat exchangers. Therefore, as described in Section 4.3.1, the particle velocities were calculated using the depth of the glass channel at 90° as indicated in each graph for the experiments at different pressures.

(a)

(b)

67
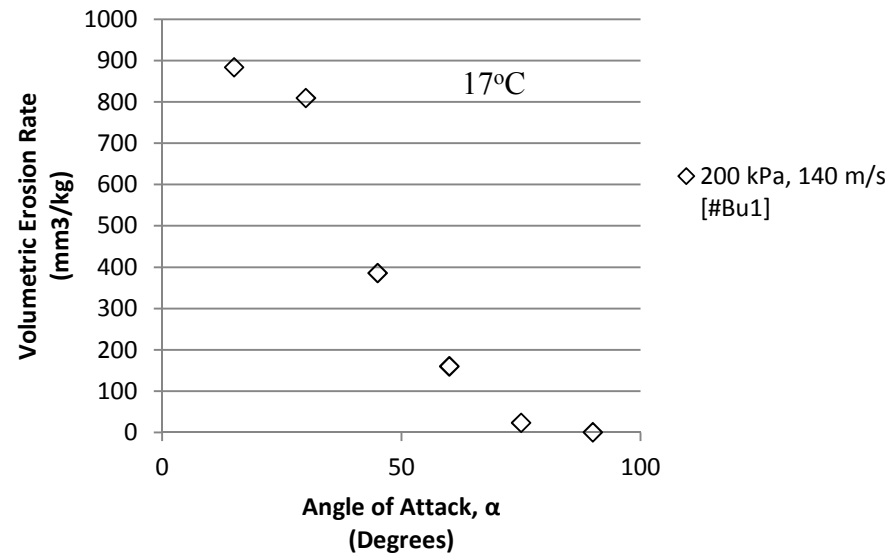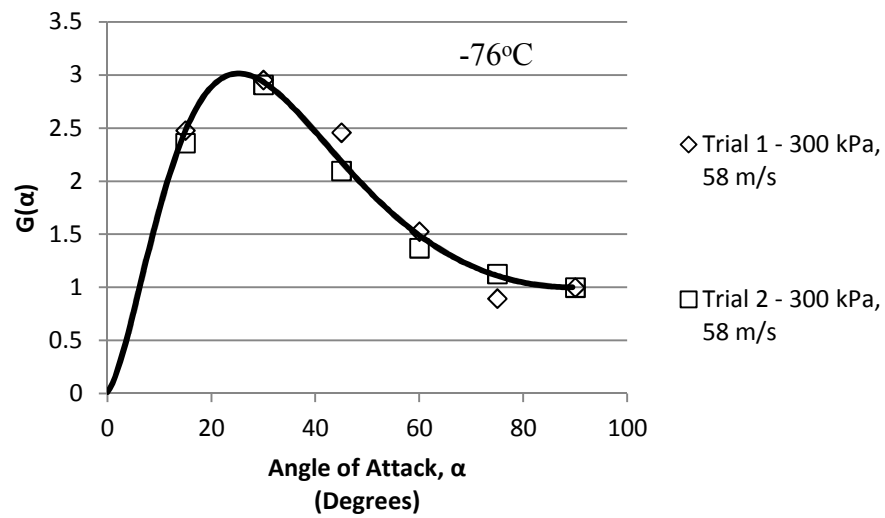
(c)
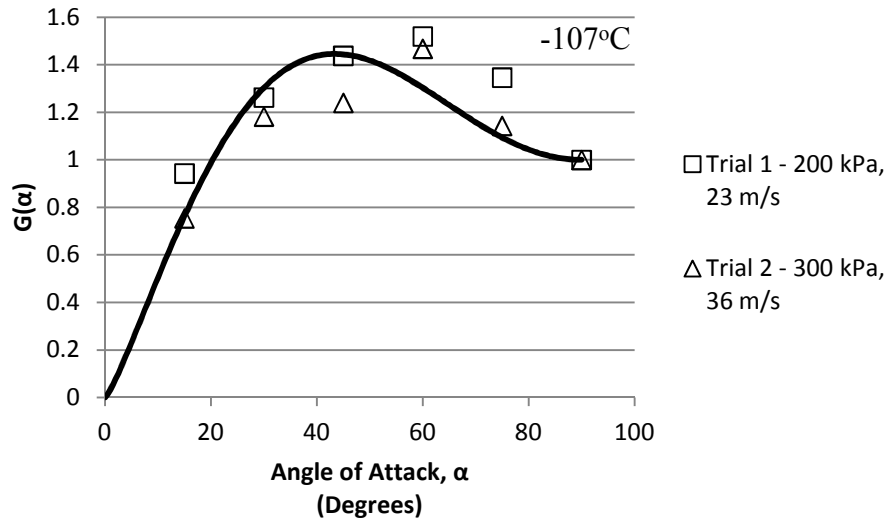
(d)
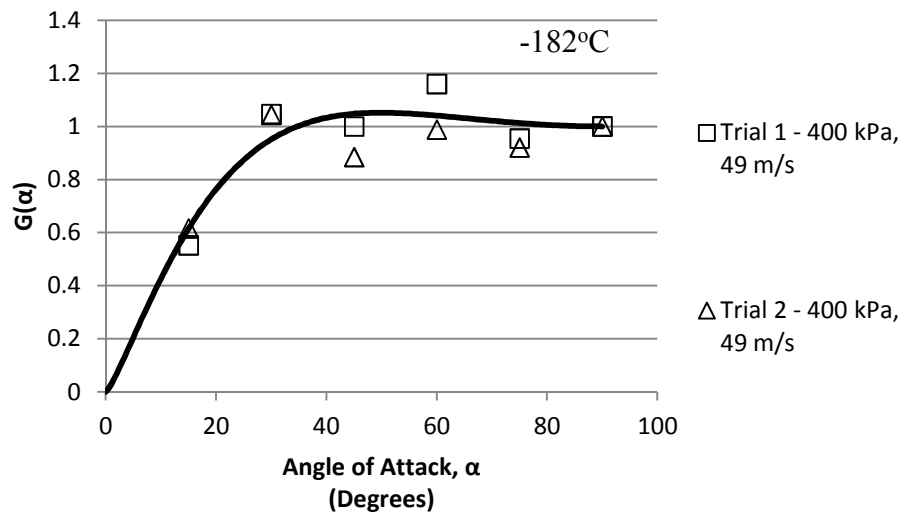
Figure 5-1 Normalized erosion rate in PTFE as a function of angle of attack at: (a) 17°C (b) -76°C, (c) -107°C, (d) -182 °C. Data points are the measurements and the solid line is the best-fit curve to *G(α)* Eq.(4-8).

As the jet temperature decreased, the peak in erosion began to flatten and shift towards 90°. At the coldest jet temperature of -182°C, the erosion rate in PTFE is almost independent of the incoming angle of the particles. This result indicates that a combination of brittle and ductile

erosion mechanisms exist at the lower temperatures. As was done in Section 4.3.2, the G(α) results are expressed with temperature as the independent variable in Figure 5-2.
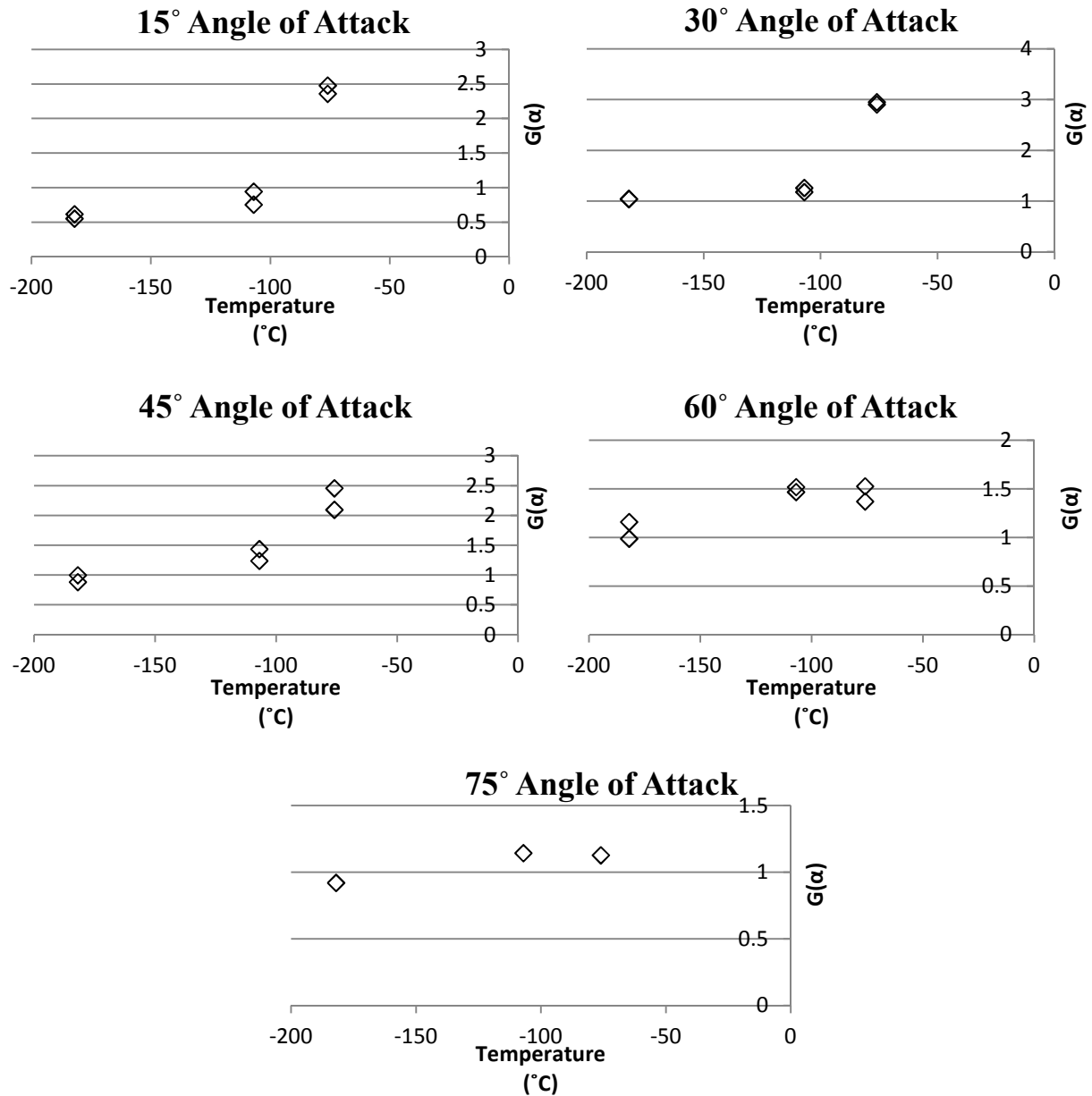
Figure 5-2 Normalized erosion rate as a function of temperature at all oblique angles of attack in PTFE.

Figure 5-2 again shows *G(α)* slowly decreasing in magnitude as the machining temperature is lowered.

Table 5-1 shows the measured PTFE volumetric erosion rates at an angle of attack of 90° for the three average temperatures. The low erosion rate in Table 5-1 for Trial 1 (269) was due to the lower pressure and hence particle velocity in this experiment.

Table 5-1 Volumetric erosion rate of PTFE at normal incidence as a function of temperature. These values were used to calculate the normalized erosion rate, $G(\alpha)$, in Fig. 5-1.

	Erosion rate at 90° (mm³/kg)		
Trial	-182°C	-107°C	-82°C
1	904	269	525
2	790	630	467

As in Chapter 4, curve fits in Figure 5-1 were again obtained by fitting Oka's equation (Eq. 4-8) using a generalized least squares fitting method, in Matlab (MathWorks, Natick MA). The variable n_1 was constrained to be between 1 and 2 since it represents the vertical component of erosion [20]. Table 5-2 shows the curve fitting variables used to obtain the fitted lines of Figure 5-1 for each of the three temperatures.

Table 5-2 Best-fit variables of Eq. 4-8 for the curves of Figure 5-1

Temperature °C	Variables		
	n1	k2	n2
-182	1.271	291.5	483.1
-107	1.242	1.24	1
-76	1.775	3.237	11.46

The shape of the $G(\alpha)$ function in Fig. 5-1 changed most between -76 and -107°C, which corresponds to the γ-relaxation found at approximately -100°C by Blumm et al. and attributed to rotation around the carbon-carbon bond [54]. This and other PTFE transition temperatures associated with crystal reordering and relaxation are listed in Table 5-3 [55]. The amorphous second order glass transition at -30°C could have influenced the increase in erosion measured from room temperature to -76°C. It is noted that the transitions of Table 5-3 typically occur over

a range of approximately 10-15°C, so correlating a single temperature to a certain transition is misleading.

Table 5-3 Transition temperatures of PTFE [55]

Transition	°C
α (Glass I)	126
β	19
β2	30
Amorphous 2nd Order	-30
γ (Glass II)	-80

Since PTFE (0.259 W/mK) [55] has a higher thermal conductivity than PDMS (0.15 W/mK) [55], heat generated from particle impact was ignored for the cryogenic blasting temperatures of -76, -107 and -182°C.

5.2.2 Dependence of Erosion Rate on Angle of Attack in High Carbon Steel

Figure 5-3 shows that $G(\alpha)$ for the high carbon steel was largely independent of temperature, although there was a weak dependency at the two smallest angles where erosion increased slightly with temperature.
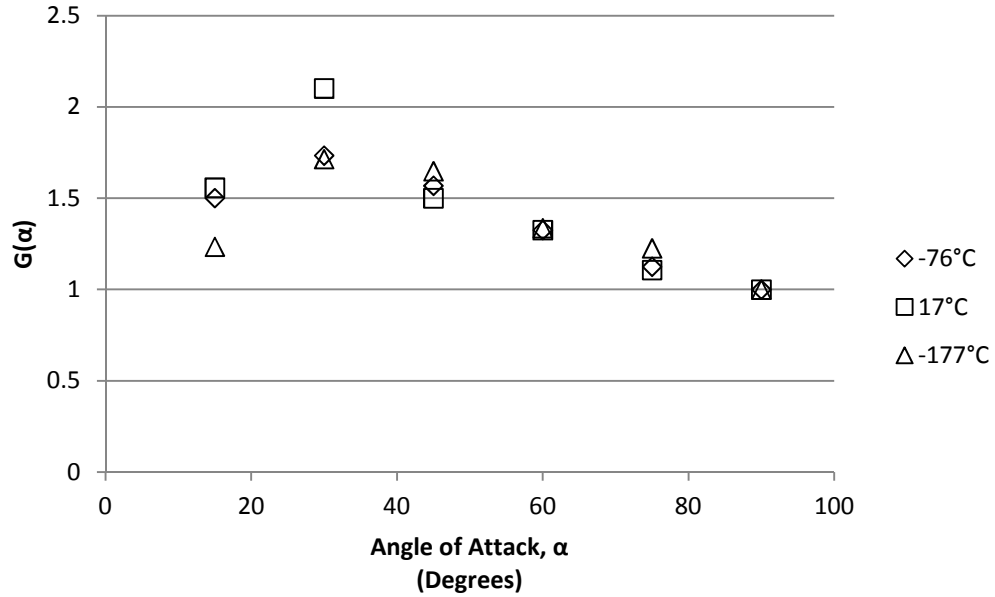
Figure 5-3 Angle dependency of erosion in high carbon steel as a function of temperature.

Oka et al. [11] found similar behavior for the room temperature erosion of aluminum ($G \approx 2$ at 20°). When the temperature decreased from 20 to -125°C, Urbanovich [31] reported a shift in the maximum erosion rate towards higher angles of attack in the low temperature solid particle erosion of a very hard bearing steel (ShKh15; 64 HRC [56]) at average particle (dry quartz sand, 200 – 315 μm) velocities of approximately 50 m/s. In contrast, Figure 5-3 indicates an erosion mechanism which does not depend on temperature for the range investigated.

5.2.3 Masked Channels in PTFE

As shown in Fig. 5-4 and Table 5-4, the surface evolution model predicted the masked micro-channel profile shapes at -180°C in PTFE more accurately than in PDMS (Fig. 4-9). As was done with the PDMS sample, the mask position was measured after it was clamped to the PTFE and found to be 566 μm (standard deviation 22 μm). The mask opening was not measured to be significantly narrower at the position of the first or second pass. This confirms that a narrow mask width is not responsible for the slightly smaller width of the first and second pass profiles. It is thought that a small amount of under-etching is responsible for the slightly wider profiles of the fourth and sixth pass.

72
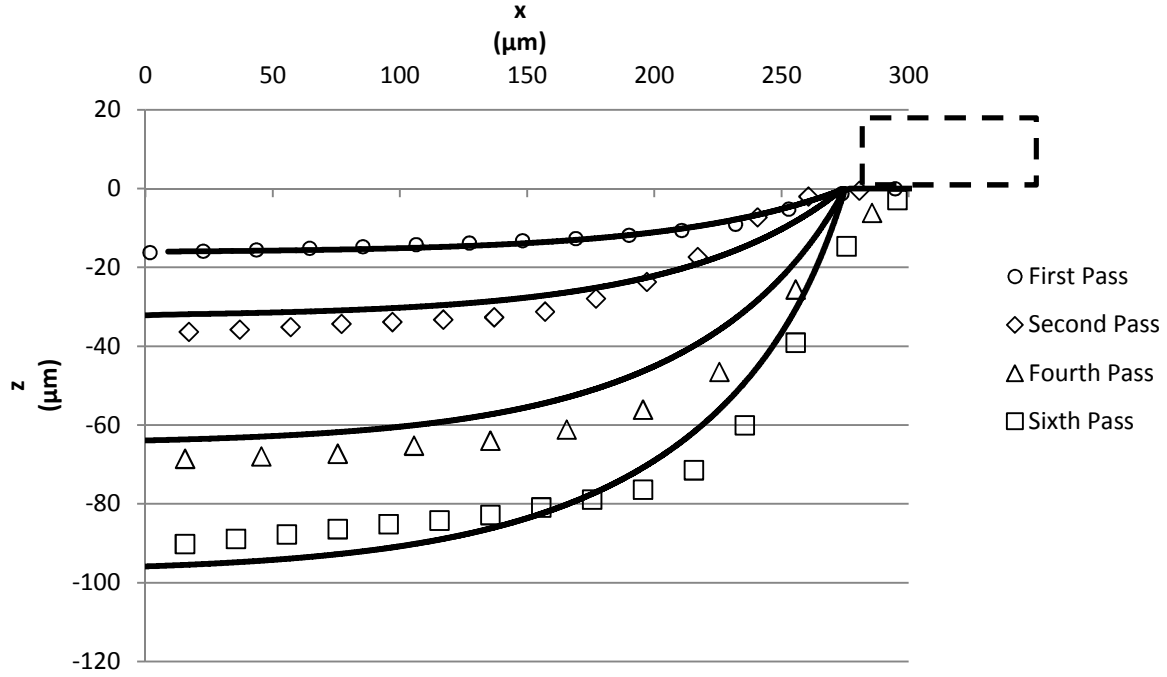
Figure 5-4 Predicted (solid lines) and experimental profiles (data points) for masked channels in PTFE at -180°C. The mask edge is shown as a dashed line. The experimental first pass was used to fit the erosive efficacy to Eq. (5-2), suggested by [26], across the mask opening.

The erosive efficacy of the jet was fit directly to the first pass in Fig. 5-4 using the function suggested by Ghobeity et al.[26] since the polynomial fit produced an unrealistic sharp point at the center of the channel,

$$E^*(x^*) = e^{B(-x^*+0.5)} - 1 \qquad (5\text{-}2)$$

where B is the curve fitting parameter which was determined to be -8.369 using a generalized least squares fitting method, in Matlab (MathWorks, Natick MA). The exponential term represents the effect of the mask edge impeding erosion. The -1 value represents the uniform flux, which as previously mentioned, was obtained by oscillating the nozzle over the mask opening. This function was used in order to force the slope of the profile to 0 at $x = 0$.

Figure 5-5 shows the surface evolution predictions in PTFE at a machining temperature of -65°C, at a nozzle angle of attack of 30° and a standoff distance of 23 mm. Although there was a small amount of mask under-etching, the first-pass profile provided an erosive efficacy distribution that accurately predicted the shapes of all the channel profiles.
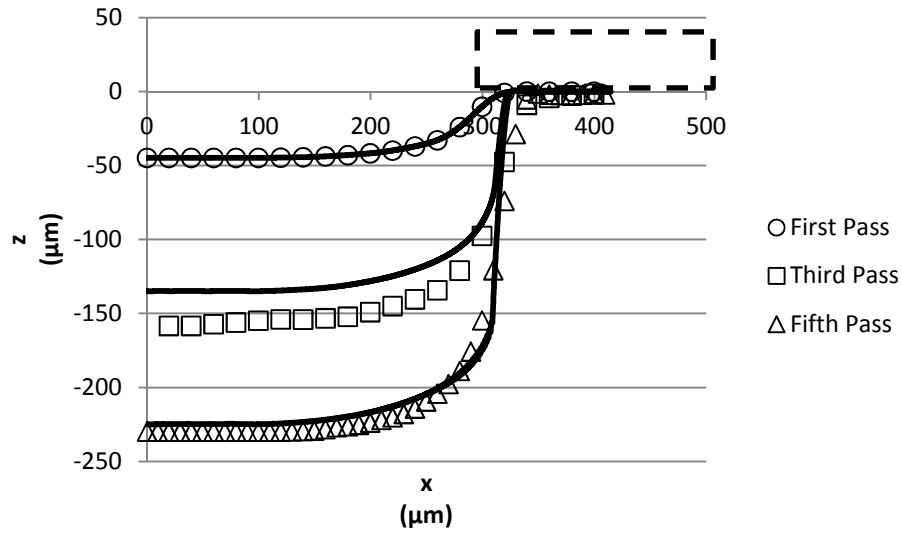
Figure 5-5 Predicted (solid lines) and experimental profiles (data points) for masked channels in PTFE at -65°C. The mask edge is shown as a dashed line. The experimental first pass was used to fit the erosive efficacy (Eq. (2-11)) across the mask opening.

The steep sidewalls shown in Fig. 5-5 are expected, as a result of the dominant ductile erosion mechanism in PTFE when blasting at -65°C. Table 5-4 summarizes the measured and predicted channel depths and the average erosion rates for the two masked channel surface evolution experiments in PTFE.

Table 5-4 Percentage error in predicted channel depths in PTFE at two different temperatures.

PTFE				
- 65 °C, 30° Angle of Attack				
592 µm Mask Spacing				
Dosage Method: Nozzle Passes				
Passes	Predicted	Experimental	% Error	Depth/pass (µm)
1	45	45	0%	45
3	135	158	15%	57
5	225	230	2%	36
-180°C, 90° Angle of Attack				
566 µm Mask Spacing				
Dosage Method: Scan Speed				
Passes	Predicted	Experimental	% Error	Depth/pass (µm)
1	16	16	0%	16
2	32	36	11%	20
4	64	69	7%	17
6	96	90	-7%	11

Table 5-4 shows that the material removed per scanning pass was relatively constant within a given experiment, indicating that there was no incubation period in any of the four cases.

5.2.4 Profile Shapes

Channel profile shapes play a major role in the flow characteristics of microfluidic channels [7]. Micro-channels fabricated using AJM tend to show steep sidewalls in ductile materials and more V-shaped profiles in brittle materials. This is due to the different angle dependency of erosion in brittle and ductile materials. Since ductile materials show maximum erosion at shallow angles, the sidewalls tend to rapidly become steep, while for brittle materials, erosion is typically maximum at high angles of attack so that sloped surfaces erode more slowly compared to flat bottoms. Figure 5-6 shows a comparison of the channel profiles resulting from AJM of the various tested materials. To allow a direct comparison of profile shapes, they have been normalized to their maximum depth and mask opening width (i.e. $z^*=z/z_{max}$, $x^*=x/w$). The glass channel was blasted at 200 kPa and room temperature whereas the more ductile PDMS and PTFE channels were both blasted at 400 kPa and -180°C and 320 kPa and -65°C. Even at such

low temperatures, the steeper sidewalls in both the PDMS and PTFE samples, when compared to the profile in glass, indicate there was still a significant amount of ductile erosion in these cases. This is consistent with the shapes of the $G(\alpha)$ curves for each polymer [53] that indicate that erosion mechanisms are still not fully brittle at the lowest cryogenic temperature of -180°C.
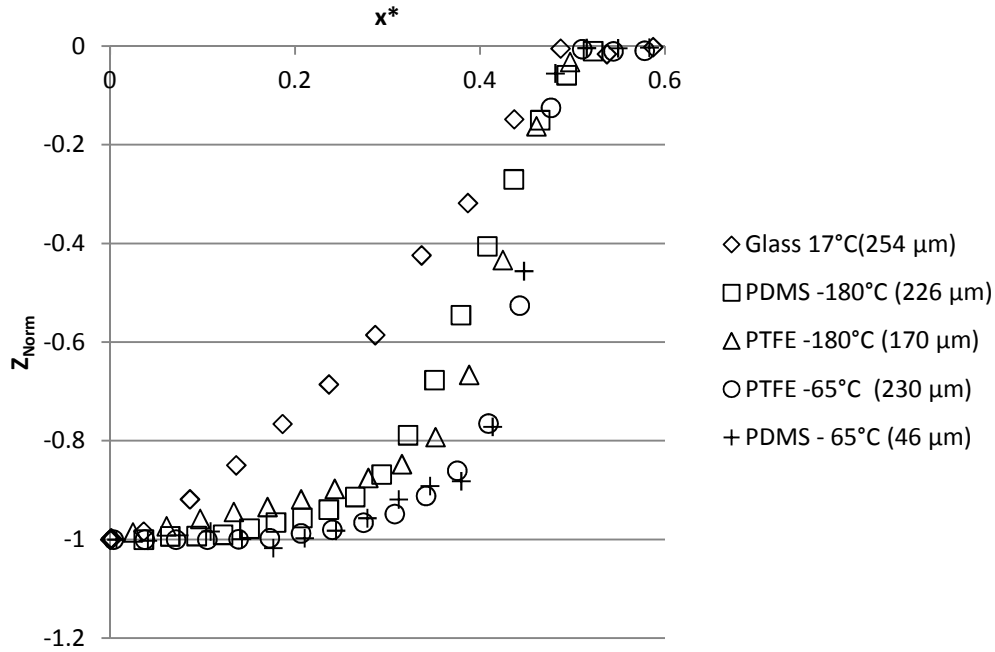
Figure 5-6 Normalized profile shapes in glass (room temperature), PDMS and PTFE (-180°C and -65°C). Actual channel depths in brackets. PDMS profiles are the deepest ones from Figs 4-9 and 4-10. PTFE profile at -180°C from a single channel blasted at 400 kPa with a scan speed of 1 mm/s. PTFE profile at -65°C from Fig. 5-5.

5.2.5 Surface Morphology and Particle Embedding in PTFE

The initially white PTFE became dark grey after blasting with the light grey 25 μm aluminum oxide particles at room temperature. Some authors have suggested that this discoloration is due to particle embedding [4], while other authors have suggested that the discoloration is caused by heat generation due to particle impact [57]. Below shows three channels blasted at room temperature at a 60, 75 and 90° angle of attack (the darkest channel being at 90°).
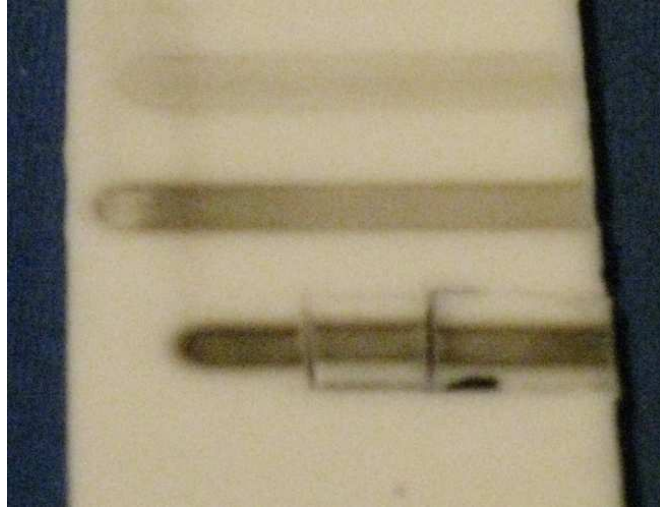
Figure 5-7 Particle embedding in PTFE at 17°C and 60, 75 and 90° nozzle angle of attack.

Figure 5-8 shows a backscatter image of the four PTFE samples used to obtain the results of Fig 5-1. Only the channels which were blasted at a 90° angle of attack were used.
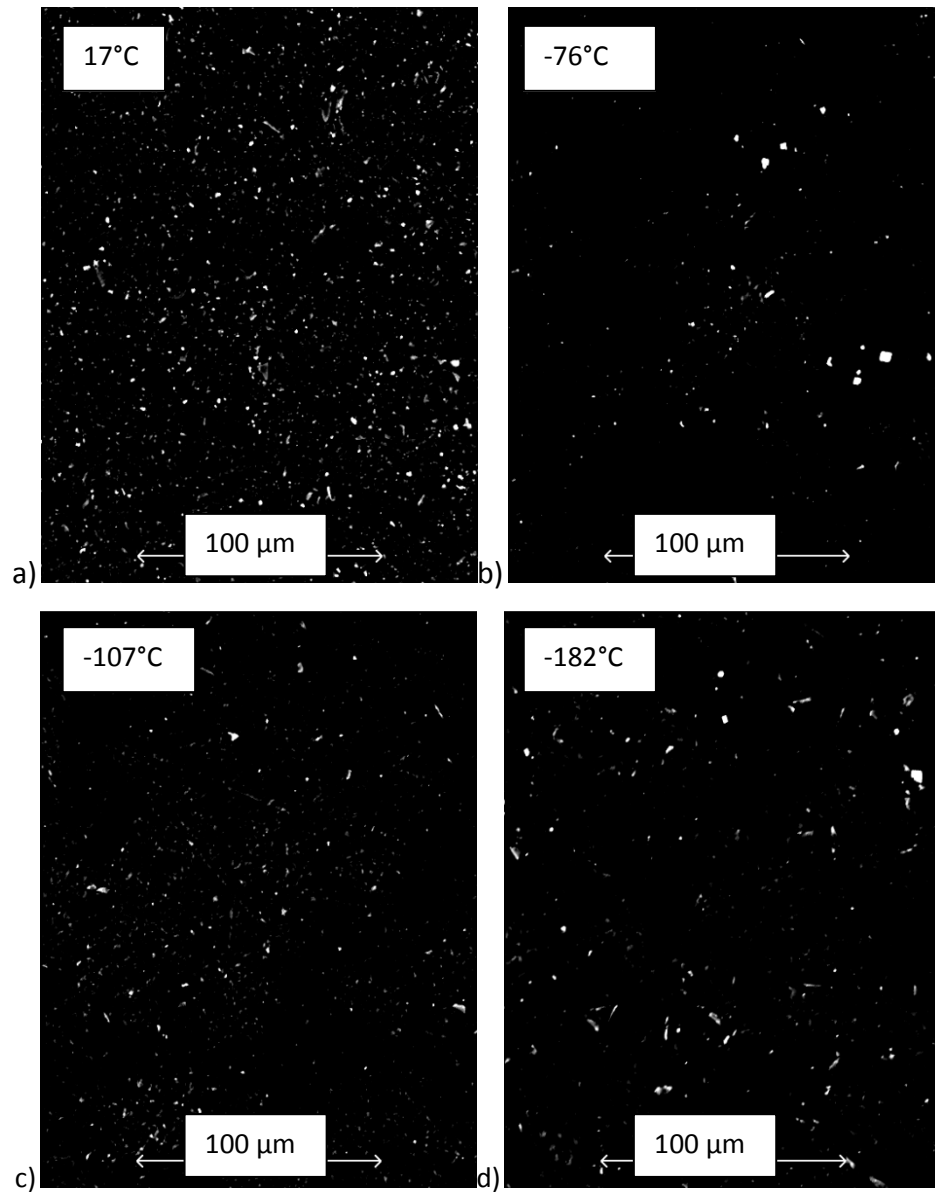
Figure 5-8 Backscatter image of aluminum oxide (white dots) embedded in Teflon at a)17°C (140 m/s), b)-182°C (49 m/s), c) -107°C (36 m/s), d) -76°C (58 m/s).

More particles were embedded at room temperature, but no significant difference in particle embedding was seen at the cryogenic blasting temperatures. This suggests that the progressive erosion increase in PTFE at the three lower temperatures was not caused by a decrease in particle embedding. The relatively large amount of embedding at room temperature is consistent with [4] which found that PTFE cannot be machined at room temperature due to particle embedding.

Further investigation is necessary to determine the erosion mechanisms present at the different temperatures and whether or not melting plays a role in impeding erosion at room temperature.

5.2.6 Volume of PTFE Removed Per Unit Kinetic Energy of Erodent

In order to compare the material removal at different particle velocities and mass flow rates, the volumetric erosion rate of PTFE was normalized by the kinetic energy of the abrasive particles, as was done in Section 4.3.6. Figure 5-9 shows how material removal in PTFE depended on the angle of attack and temperature.
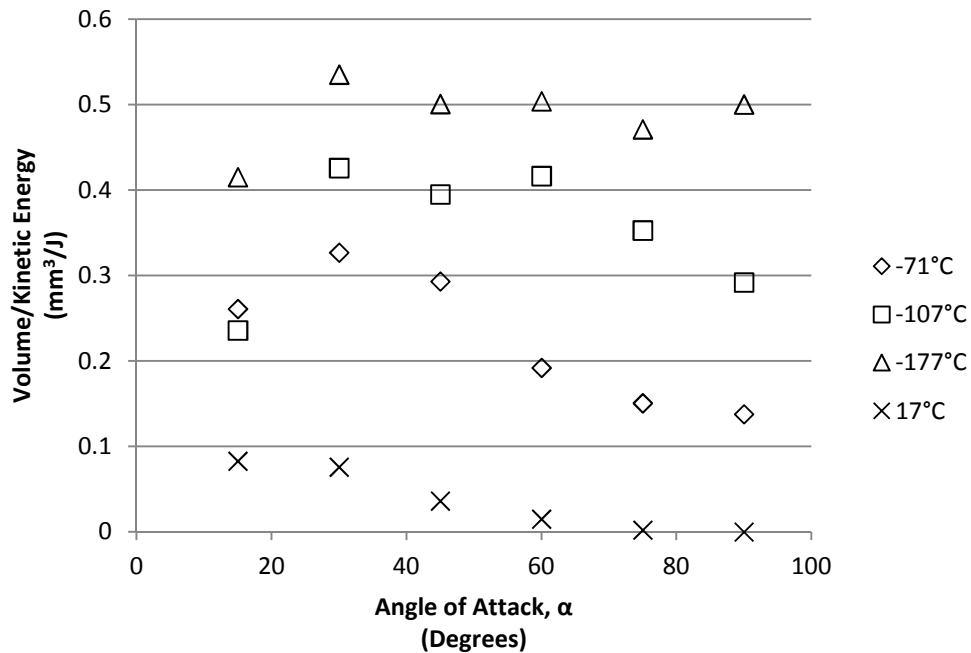
Figure 5-9 Volumetric erosion per unit kinetic energy of erodent in PTFE as a function of temperature and angle of attack.

The erosion of PTFE increased significantly with decreasing temperature (over five times greater at -182°C), and became much less sensitive to the impact angle.

5.2.7 Temperature Dependence of Erosion in High Carbon Steel

The temperature dependence of erosion in high carbon steel was investigated since it is arguably the most common mask material used in AJM. Since the dependence of erosion in glass has previously been shown to be a weak function of temperature, the ratio of the channel depths

in steel, z_S, to the channel depth in glass at 90°, z_{G90}, is solely indicative of how steel erosion changes with temperature. The erosion rate increase in high carbon steel at lower temperatures, shown in Fig. 5-10, was moderate when compared to that of PTFE (Fig 5-11).
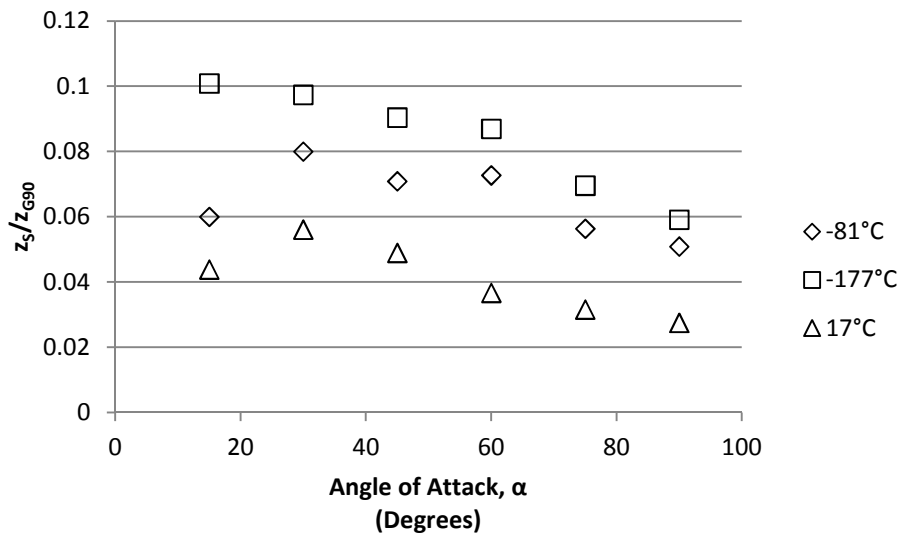
Figure 5-10 Ratio of channel depths in steel to glass as a function of angle of attack and temperature.
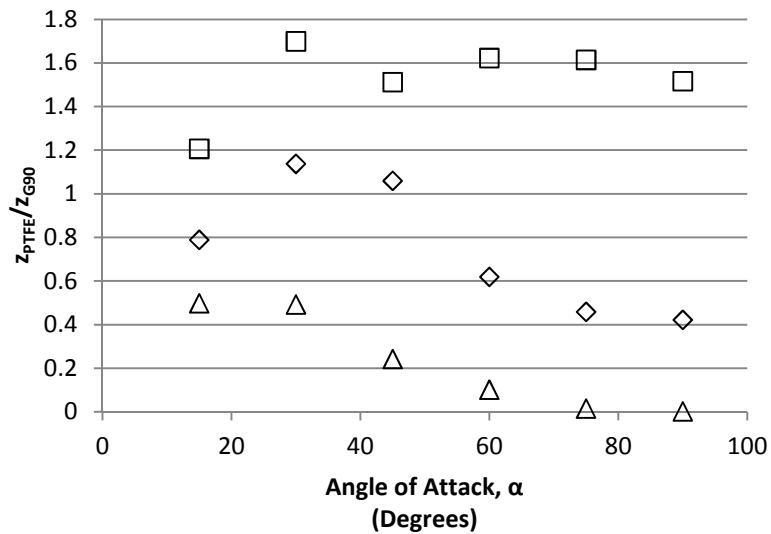
Figure 5-11 Ratio of channel depths in PTFE to glass as a function of angle of attack and temperature.

At 90° angle of attack, the erosion rate increased by a factor of two. This is similar to the increase of 1.7 reported in [31] for the erosion increase in steel (ShKh15) when the blasting temperature was decreased from 20°C to -150°C.

The erosion rate of the high carbon steel samples reached a minimum at α= 90°, and only moderately increased with a decrease in temperature while the erosion in PTFE was maximum at α= 90° and -177°C (Fig. 10).   Thus, in order to obtain a maximum erosion rate while performing masked CAJM in PTFE while also limiting the mask erosion, the CAJM should be performed at α= 90° at T=-177°C.

5.3 Summary of Findings and Results

The maximum erosion rates occurred in PTFE at the lowest blasting temperature of -182°C between the angles of 30° and 90°. Since the $G(\alpha)$ of high carbon steel showed a weak dependency on temperature and erosion only increased by a factor of approximately 2 when the steel mask material was exposed to the -182°C jet, this is also the scenario which maximizes mask life while keeping high erosion rates in the PTFE.

The shapes of the $G(\alpha)$ curves for PTFE suggest that erosion is still a mixture of brittle and ductile mechanisms even at the coldest jet temperatures. Figure 5-4 confirms this by showing the still relatively steep sidewalls in the masked channels of PTFE when compared to the sidewall slopes of glass.

Surface evolution predictions of machining at -65 and -181°C showed good agreement with experimental results which suggests that no incubation period or significant amount of particle occurs at these scenarios.

After post machining analysis of the PTFE samples, it was concluded that a decrease in particle embedding is not responsible for the increase in erosion seen at the cryogenic jet temperatures. As was seen in a previous study [4], particle embedding is proposed to be the mechanism which reduces erosion at room temperature. Further study is required to determine if melting occurs in PTFE during erosion at room temperature. Also, the erosion mechanisms which exist at the various machining temperatures remain unknown.

6 Conclusions

The dominant erosion mechanism in PDMS at temperatures of -82°C and -127°C appears to be ductile, because the normalized erosion rate, *G(α)*, shows maximum erosion at angles of attack below 20°. The *G(α)* curve for -178°C shows a maximum erosion rate in the range of 30-60°, indicating a more brittle erosion mechanism below the glass transition temperature which is in the vicinity of -120°C. The presence of microcracks in Fig 4-15e also suggested a brittle erosion mechanism at the coldest temperature of -178°C.

Glass channel depths at 90° were an effective way of inferring the velocity at the centreline of the jet at various temperatures. Glass reference channels machined at other impact angles during each PDMS, PTFE and steel erosion rate measurement, provided an accurate way of obtaining the *G(α)* curves that was independent of fluctuations in the mass flow rate.

The first pass profile fit to the erosive efficacy of the jet using a seventh order polynomial resulted in good surface evolution predictions in PDMS. The largest error in channel depth prediction for PDMS occurred at the warmest jet temperature, because of increased particle embedding.

The efficiency of PDMS machining, expressed as volume removal per unit kinetic energy, increased markedly below the glass transition of PDMS, being maximum between 30° and 60° angle of attack at approximately -178°C.

The profile shape of a masked channel in PDMS at -180°C shows there is a decrease in erosion near the mask edge. This causes initially narrower channels at small particle dosages (i.e. first and second pass) which render the first pass fit method inadequate for the deeper channels. Fitting the erosive efficacy using a pass which is beyond this particle dosage results in better predictions of the deeper profile shapes. Preconditioning the surface by removing 20 μm appeared to have no effect on decreasing this effect. The remaining channels machined in PDMS (-65°C at 15°) and PTFE (-180°C at 90° and -65°C at 30°) showed good agreement with the predictions of Eq.(4-7). This indicated that no incubation period or effect of particle shielding or embedding occurred at these conditions.

The shapes of the *G(α)* curves for PTFE and PDMS both suggest that erosion is still a mixture of brittle and ductile mechanisms even at the coldest jet temperatures. Figure 5-6 confirms this by showing the still relatively steep sidewalls in the masked channels of both polymers when compared to the sidewall slopes of glass.

Maximum erosion rates occur in PTFE at the lowest blasting temperature of -182°C between the angles of 30° and 90°. Since $G(\alpha)$ of high carbon steel shows a weak dependency on temperature and erosion only increases by a factor of about 2 when the steel mask material is exposed to the -182°C jet, this is also the scenario which maximizes mask life while keeping high erosion rates in the PTFE.

After post machining analysis of the PTFE samples, it was concluded that a decrease in particle embedding is not responsible for the increase in erosion seen at the cryogenic jet temperatures, but rather a change in the material properties of the polymer caused by the transition temperatures shown in Table 5-3. As was seen in a previous study [4], particle embedding is proposed to be the mechanism which deters erosion at room temperature.

6.2 Recommendations for Future Work

Erosion as a function of temperature has been investigated for two materials which have potential in microfluidics. Many aspects of this research can be investigated further:

- The mechanisms of erosion in PTFE at the various machining temperatures remain unknown. It is also suspected that melting is responsible for impeding erosion at room temperature in PTFE. Strong evidence for melting still has not been found.
- Microfluidic chips require smooth channels for predictable flow. Further investigation is warranted for determining how temperature and angle of attack can be used to minimize surface roughness.
- The effect of temperature on the erodent particles themselves should be quantified. If particles fracture upon hitting the substrate surface, energy is wasted which could otherwise contribute to erosion. It would be of interest to determine what type of erodent material is most effective at such low temperatures.
- Confirming the actual heat transfer coefficient of the jet at the various temperatures would be beneficial so that a finite element analysis could be performed to determine the temperature field within the polymer. Either a bank of tightly spaced micro thermocouples with a high acquisition rate or a thermal imaging camera could be used to confirm the results.

- The behavior of polymeric mask material at the colder jet temperatures could also be investigated since lithographic patterning is a much more efficient mask patterning method as opposed to machining metal masks. In particular, it would be useful to study whether a polymeric mask material can be easily patterned and still erosion resistant at even the coldest jet temperature of -196°C.

Appendix A

Ratio of hole to channel depth

At $\alpha=90°$, the ratio between the depth of a hole at a given dwell time, Δt and a single pass channel at a given scan speed v_t can be derived from first principles, knowing the particle and velocity distributions. Assuming a linearly decreasing velocity distribution with a slope A, and a flux distribution as

$$\varphi(r) = \frac{\dot{M}}{\pi}\left(\frac{\beta}{h}\right)^2 e^{-\left(\frac{\beta r}{h}\right)^2} \tag{A1}$$

the centerline depth of a channel, z_c, after one pass can be derived using Eq. (4-11), as

$$z_c = \frac{C\,\beta^2\,V_c^{\ k}\dot{M}}{\rho_s\pi h^2}\int_0^{\frac{2r_s}{v_t}}[1-A|(r_s-v_t t)|]^k e^{\frac{-\beta^2}{h^2}(r_s-v_t t)^2}\,dt \tag{A2}$$

where r_s is the radius of the footprint of the jet on the surface, and V_c is the centerline velocity of the particles in the jet. The depth of a hole, z_h, can be derived in a similar manner as

$$z_h = \frac{C\,\beta^2\,V_c^{\ k}\dot{M}\,\Delta t}{\rho_s\pi h^2} \tag{A3}$$

The ratio of Eqs. (A2) and (A3) is thus

$$\frac{z_h}{z_c} = \frac{\Delta t}{\int_0^{\frac{2r_s}{v_t}}[1-A|r_s-v_t t|]^k\,e^{\frac{-\beta^2}{h^2}(r_s-v_t t)^2}\,dt} \tag{A4}$$

For the holes and channels machined in the borosilicate glass under the conditions described in Section 7.0, $\Delta t = 10$s, $r_s \sim 3$ mm, $v_t = 0.5$ mm/s, $h = 20$ mm, $k = 1.43$ [46], and $\beta = 18$ [9]. The slope of the velocity distribution used in Eq. (A2), $A=3$, was obtained from a linear fit of the

Particle tracking velocimetry (PTV) results of [9]. From Eq. (30), $z_h/z_c = 2.92$ and is compared to the measured hole depth versus channel depth relationship in Fig 4-3.

Each data point in Fig. 4-3 was obtained by changing the velocity of the particles, by adjusting the blasting pressure. The solid line with slope of 2.19 represents the least squares best fit of the measured data, and the dashed line with slope of 2.92 is from Eq. (A2).

The slightly poorer agreement at the higher channel depths may be due to a nozzle focus coefficient that does not remain constant over the range of velocities considered.

It is noted that knowing the maximum velocity, the average velocity in the jet, V_{ave} can be obtained as

$$V_{avg} = \int_0^{r_s} V_C \left(1 - A\frac{r}{h}\right) 2 \left(\frac{\beta}{h}\right)^2 re^{-\left(\frac{\beta r}{h}\right)^2} dr \tag{A5}$$

Appendix B

Dependence of Erosion on the Slope of the Surface at the Leading Edge of the Abrasive Jet

Surface topography in AJM is dictated by controlling the amount of particle impacts, aka particle dosage, the feature is exposed to. Particle dosage can be controlled by scanning the nozzle over the surface multiple times or by changing the scan speed of the nozzle. Changing the nozzle scan speed is a much more versatile method since consecutive dosages do not have to be a multiple of the initial single pass dose. As Eq. (4-6) indicates, the erosion rate depends on the angle of particle impact, α. Since the slope of the material along the scanning direction at the leading edge of the channel varies with the depth of the channel, z, machined in a single pass, the apparent measured erosion rate may be affected by the method used to control dose. Since both methods were used in the following experiments, it must be confirmed that both will give the same amount of erosion for a specific particle dosage. Figure B-1 shows an example of the slope at the leading edge for a shallow and a deep channel made using a single pass at different scan speeds, v_t (1 mm/s and 0.2 mm/s). The slope of the leading edge for the deep channel would be similar to the slope of the leading edge for the method of altering dosage by the nozzle scan speed. The shallow channel would have a slope similar to the channel which used nozzle passes to control the dose of particles.
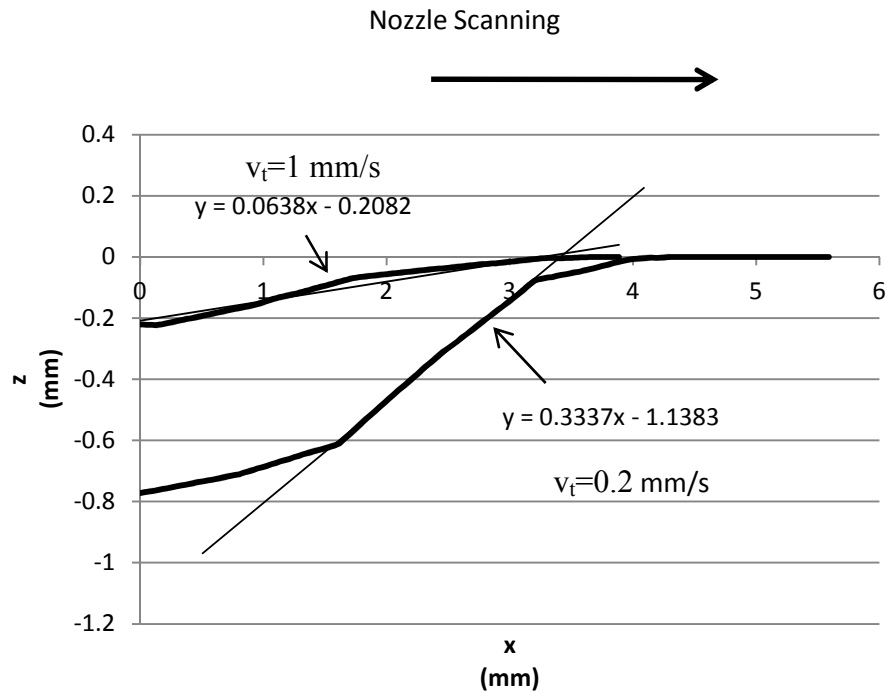
Figure B-1 Profile showing the slope of the leading edge in PTFE machined at -180°C and 400 kPa.

In order to determine whether the slope of the leading edge of the channel affected the magnitude of the erosion rate, two unmasked channels were machined in PTFE. The first channel controlled the particle dosage by changing the nozzle scan speed (1, 0.33 and 0.2 mm/s). The second channel controlled particle dosage by changing the amount of nozzle passes over the surface at 1 mm/s (1, 3 and 5 passes). This ensured the channel sections were exposed to overall the same dose of particles. Glass channels were machined before each PTFE channel to detect mass flow fluctuations. A heat exchanger of length 80 cm along with a blast pressure of 400 kPa was used with the abrasive nozzle 20 mm from the surface.

B1 Dependence of Erosion on the Slope of the Surface at the Leading Edge of the Abrasive Jet

For each of the three jet dosages attained which were equal between the two methods, five Teflon channel profiles were measured, as shown below in Table 1 along with the average and standard deviation of the channel depth. The jet temperature was recorded to be -179°C. The significantly larger standard deviations of channel depth when varying the scan speed suggests that using scan speed to change the particle dose to the surface, results in a magnification of the

mass flow fluctuations. Table B1 shows that altering the dose by changing the number of passes averages out the mass flow fluctuations and provides much more consistent channel depths than changing the scan speed

Table B1 – Channel depths for two different dosage methods.

		Varying Scan Speed		
		Scan Speed (mm/s)		
		1	0.33	0.2
Dose (kg/m^2)		90.2	273	451.2
Channel Depth (µm)		137	376	584
		146	295	538
		102	412	533
		161	260	568
		139	421	451
	Avg	137	352.8	534.8
	SD	21.71405	71.84497	51.37801
		Varying Number of Channel Passes		
		1	3	5
Dose (kg/m^2)		90.2	273	451.2
Channel Depth (µm)		138	372	496
		139	354	529
		109	335	509
		144	309	467
		116	333	499
	Avg	129.2	340.6	500
	SD	15.61089	23.73394	22.51666

The particle dose for each method, as shown in Table B1, can be confirmed to be equal by using the particle mass flux distribution found by Ghobeity et al.

$$Dose = \frac{\dot{M}}{\pi}\left(\frac{\beta_w}{h}\right)^2 \int_0^{\frac{r_s}{v_t}} e^{-\beta^2\left(\frac{r_s - v_t t}{h}\right)^2} \tag{B1}$$

where $\dot{M}$ is the mass flow rate (kg/s), β_w is the flow focus coefficient (9), h is the nozzle standoff distance (0.023 m), r_s is the scar radius of the jet (0.002 m) and v_t is the scan speed of the substrate. Using a scan speed of 1 mm/s results in a dose of 90.2 kg/m^2 whereas a scan speed of 0.33 mm/s gives a dose of 273.4 kg/m^2. This clearly shows that three nozzle passes at 1 mm/s will therefore be given the same dose as a single pass at 0.33 mm/s. The dose at 0.2 mm/s was calculated to be 451.2 kg/m^2.

A glass channel was machined before each of the Teflon channels in order to reveal the magnitude of the mass flow fluctuations. Four profiles were taken every 10 mm along both 50 mm glass channels. The average channel depth was 121.12 μm with a standard deviation of 16.1 μm.

Although the standard deviations of channel depth for each dosage method are clearly different, performing a t-test at a 95% confidence interval on the data from Table B1 shows there is no statistically significant difference between the average depths of the two dosage methods. Getu et al. attributed a difference of erosion for the forward and backwards scanning orientation to particle embedding. It was suspected that the leading edge profile shape affected the amount of particle embedding. Shipway et al. [27] have suggested that the level of particle embedding is a function of the particle impulse which is related to the normal component of velocity with respect to the surface. Since minimal particle embedding is seen in PTFE at the low temperature of -180°C (Fig 5-6), it is suspected that the profile of the leading edge of the channel has a minimal effect on erosion.

8.0 References

[1] Getu H., Ghobeity A., Spelt J.K., Papini M., "Abrasive Jet Micromachining of Acrylic and Polycarbonate at Oblique Angles of Attack", *Wear,* 265 (2008), 888-901.

[2] Iliescu C., Tay F.E.H., "Wet Etching of Glass", *Semiconductor Conference,* 1 (2005) 35-44.

[3] Getu H., Spelt J.K., Papini M., "Cryogenically assisted abrasive jet micromachining of polymers", *Journal of Micromechanics and Microengineering,* 18 (2008) 115010.

[4] Getu H., Ghobeity A., Spelt J.K., Papini M., "Abrasive jet micromachining of polymethylmethacrylate", *Wear,* 263 (2007) 1008-1015.

[5] Natarajan S., Chan-Yen D.A., Gale B.K., "Large-area, high-aspect-ratio SU-8 molds for the fabrication of PDMS microfluidic devices", *Journal of Micromechanics and Microengineering,* 18 (2008) 045021.

[6] Ren K., Dai W., Zhou J., Su J., Wu H., Whole-Teflon microfluidic chips, Proceedings of the National Academy of Sciences. http://www.physorg.com/news/2011-05-smooth-teflon-microfluidic-chips.html

[7] Starkweather, H.W., "Melting and Crystalline Transitions in Normal Perfluoroalkanes and Poly(tetrafluoroethylene), *Macromolecules,* 19(1986), 1131-1134.

[8] Dyment J., Ziebland H., "The tensile properties of some plastics at low temperature", *Journal of Applied Chemistry,* 8(1958), 203-206)

[9] Burzynski T., Papini M., "Measurement of the particle spatial and velocity distributions in micro-abrasive jets", *Measurement Science and Technology,* 22 (2011), 025104.

[10] Z. Feng, A. Ball. "The Erosion of Four Materials Using Seven Erodents – Towards an Understanding" *Wear,Vol 233-235, pp 674-684, 1999.*

[11] Y.I. Oka, M. Matsumara, T. Kawabata. "Relationship Between Surface Hardness and Erosion Damage Caused by Solid Particle Impact" *Wear,* Vol 162-164, pp 688-695, 1993.

[12] Walley S.M., Field J.E., "The Erosion and Deformation of Polyethylene by Solid-Particle Impact", *Phil. Trans. R. Lond.,* 321 (1987), 277-303.

[13] Arnold J.C., Hutchings I.M., "A model for the erosive wear of rubber at oblique impact angles", *Applied Physics Conference Paper,* 25 (1991) A222 – A229.

[14] Arnold J.C., Hutchings I.M., "Erosive wear of rubber by solid particles at normal incidence", *Wear,* 161(1993) 213-221.

[15] Hutchings I.M., Deuchar D.W.T., "Erosion of unfilled elastomers by solid particle impact", *Journal of Materials Science,* 22 (1987) 4071-4076.

[16] Besztercey, G., Karger-Kocsis J., Szaplonczay P., "Solid particle erosion of electrically insulating silicon and EPDM rubber compounds", *Polymer Bulletin,* 42 (1999) 717-724.

[17] Harsha A.P., Thakre A.A., "Investigation on solid particle erosion behavior of polyetherimide and its composites", *Wear,* 262 (2007) 807-818.

[18] Zahavi J., Schmitt G.F., "Solid particle erosion of polymeric coatings", *Wear,* 71 (1981) 191-210.

[19] Barkoula N.-M., Karger-Kocsis J., "Review Processes and influencing parameters of the solid particle erosion of polymers and their composites", *Journal of Material Science,* 37 (2002), 3807-3820.

[20] Oka Y.I., Ohnogi H., Hosokawa T., Matsumura M., "The impact angle dependence of erosion damage caused by solid particle impact.", *Wear,* 203-204 (1997), 573-579.

[21] W.D. Callister. "Materials Sceince and Engineering An Introduction" *John Wiley and Sons,* 2003.

[22] R.F. Boyer "Dependence of mechanical properties on molecular motion in polymers" Polymer Engineering and Science, Vol 8, pp 161-186, 1968.

[23] E. Sanchez-Gonzalez, P. Miranda, J.J.M Martinez, F. Guiberteau, A. Pajares "Temperature dependence of mechanical properties of alumina up to the onset of creep" Journal of the European Ceramic Society, Vol 27, pp 345-349, 2007.

[24] R. Khanna, B. Basu "Low friction and severe wear of alumina in cryogenic environment: A first report" Journal of Materials Research, Vol 21, pp 832-844, 2006.

[25] Boonkkamp J.H.M.T.T., Jansen J.K.M., "An analytical solution for mechanical etching of glass by powder blasting", *Journal of Engineering Mathematics,* 43 (2002) 385-399.

[26] Ghobeity A., Getu H., Papini M., Spelt J.K., "Surface evolution models for abrasive jet micromachining of holes in glass and polymethylmethacrylate (PMMA)", *Journal of Micromechanics and Microengineering,* 17 (2007) 2175 – 2185.

[27] Shipway P.H., Fowler G., Pashby I.R., "Characteristics of the surface of a titanium alloy following milling with abrasive waterjets". *Wear,* 258 (2005), 123-132.

[28] Shipway, P.H., Weston D.P., "Thermal effects in blasting and erosion of polymeric materials" *Journal of Materials Processing Technology,* 209 (2009) 6161-6167.

[29] Ghobeity A., Ciampini D., Papini M., "An analytical model of the effect of particle size distribution on the surface profile evolution in abrasive jet machining", *Journal of Materials Processing Technology*, 209 (2009), 6067-6077.

[30] Getu H., Spelt J.K., Papini M., "Thermal analysis of cryogenically assisted abrasive jet micromachining of PDMS", *International Journal of Machine Tools and Manufacture,* 51(2011), 721-730.

[31] Urbanovich L.I., Kramchenkov E.M., Chunosov Y.N., "Investigation of Low-Temperature Gas-Abrasive Erosion", *Soviet Journal of Friction and Wear,* 13 (1992), 80-83.

[32] Urbanovich L.I., Kramchenkov E.M., "Erosion of Steels and Alloys in Their Collision with a Flux of Abrasive Particles", *Journal of Engineering Physics*, 72 (1999), 519-525.

[33] Muju M.K., Pathak A.K., "Abrasive Jet Machining of Glass at Low Temperature", *Journal of Mechanical Working Technology,* 17 (1988) 325-332.

[34] F.P. Incropera, D.P. Dewitt. " Fundamentals of Heat and Mass Transfer" *John Wiley and Sons*, 2002.

[35] D.T. Vader, G. Chrysler, R. Chu, R.E. Simons "Experimental Investigation of Subcooled Liquid Nitrogen Impingement Cooling of a Silicon Chip" *Transactions on components, packaging, and manufacturing technology*, Vol 18, pp 788-795, 1995.

[36] V. Drach, J. Fricke. "Transient Heat Transfer from Smooth Surfaces into Liquid Nitrogen" *Cryogenics,* Vol 36, pp 263-269, 1996.

[37] M. Kida, Y. Kikuchi, O. Takahashi, I. Michiyoshi. "Pool Boiling Heat Transfer in Liquid Nitrogen" *Journal of Nuclear Science and Technology*, Vol 18. pp 501-513, 1981.

[38] H. Zhang, S. Wong, J. Wang "Experimental study on boiling flow in liquid nitrogen in inclined tubes – Velocities and length distribution of Taylor bubbles" Journal of the Taiwan Institute of Chemical Engineers, Vol 40, pp 431-438, 2009.

[39] G. Hetsroni, A. Mosyak, Z. Segal, G. Ziskind. "Uniform Temperature Heat Sink for Cooling of Electronic Devices" *International Journal of Heat and Mass Transfer*, Vol 45, pp 3275-3286, 2002.

[40] H.Y. Wu, P. Cheng, H. Wang. "Pressure Drop and Flow Boiling Instabilities in Silicon Microchannel Heat Sinks" *Journal of Micromechanics and Microengineering,* Vol 16, pp 2138-2146, 2006.

[41] S.L. Qi, P. Zhang, R.Z. Wang, L.X. Xu, "Flow boiling of liquid nitrogen in microtubes: Part I – The onset of nucleate boiling, two phase flow instability and two phase pressure drop" International Journal of Heat and Mass Transfer, Vol 50. 2007.

[42] R. Chu, "A review of IBM sponsored research and development projects for computer cooling". *IEEE SEMI-THERM Symposium.* 1999

[43] L. Huang, M.S. El-Genk "Heat transfer of an impinging jet on a flat surface" International Journal of Heat and Mass Transfer, Vol 37, pp 1915-1923, 1994.

[44] H. Martin, "Heat and Mass Transfer Between Impinging Gas Jets and Solid Surfaces" *Advances in Heat Transfer*, Vol 13, pp 1-59, 1977.

[45] Whitesides G.M., "The origins and future of microfluidics", *Nature,* 442 (2006) 368-373.

[46] Ghobeity A., Krajac T., Burzynski T., Papini M., Spelt J.K., "Surface evolution models in abrasive jet machining", *Wear,* 264 (2008), 185-198.

[47] Ghobeity A., Getu H., Krajac T., Spelt J.K., Papini M., "Process repeatability in abrasive jet micro-machining", *Journal of Materials Processing Technology,* 190 (2007), 51-60.

[48] Ciampini D., Papini M., "A cellular automata and particle-tracking simulation of abrasive jet micromachining that accounts for particle spatial hindering and second strikes", *Journal of Micromechanics and Microengineering,* 20 (2010) 045025.

[49] Aguilar G., Majaron B., Verkruysse W., Zhou Y., Nelson J.S., Lavernia E.J., "Theoretical and experimental analysis of droplet diameter, temperature, and evaporation rate evolution in cryogenic sprays", *International Journal of Heat and Mass Transfer,* 44 (2001), 3201-3211.

[50] Bar G., Brandsch R., "Effect of Viscoelastic Properties of Polymers on the Phase Shift in Tapping Mode Atomic Force Microscopy", *American Chemical Society,* 14 (1998) 7343-7347.

[51] Clarson S.J., Dodgson K., Semlyen J.A., "Studies of cyclic and linear poly(dimethylsilxones): 19. Glass transition temperatures and crystallization behaviour", *Polymer,* 26 (1986) 244-245.

[52] Wensink H., Jansen H.V., Berenschot J.W., Elwenspoek M.C., "Mask materials for powder blasting", *J. Micromech. Microeng.,* 10 (2000), 175-180.

[53] Gradeen A.G., Spelt J.K., Papini M., "Cryogenic abrasive jet machining of Polydimethylsiloxane at different temperatures", *Wear,* Accepted.

[54] Blumm J., Lindemann A., Meyer M., Strasser C., Characterization of PTFE using advanced thermal analysis techniques.

[55] Mark, J. "Polymer Data Handbook", Oxford Press, New York (1999).

[56] Antipov V.I., Vinogradov L.U., Lazarev E.M., Mukhina Y.E., Antoshchenkov A.E., Doronin D.I., Lukina Y.A., Kochetova I.V., "Increasing the Hardness of ShKh15 Steel in Its Products", *Russian Metallurgy,* 4(2009), 334-337.

[57] Rao P.V., Young S.G., Buckley D.H., "Solid spherical glass particle impingement studies of plastic materials" 1983 NASA Tech. Paper 2161 (*National Aeronautics and Space Administration*)

[58] P.J. Slikkerveer, F.H. in't Veld. "Model for Patterned Erosion" *Wear*, Vol 233-235, pp 377-386, 1999.